

PPPL- 5041

PPPL- 5041

Enhanced Confinement Scenarios Without Large Edge  
Localized Modes in Tokamaks:  
Control, Performance, and Extrapolability Issues for ITER

R. Maingi

JULY 2014



# Princeton Plasma Physics Laboratory

## Report Disclaimers

---

### Full Legal Disclaimer

This report was prepared as an account of work sponsored by an agency of the United States Government. Neither the United States Government nor any agency thereof, nor any of their employees, nor any of their contractors, subcontractors or their employees, makes any warranty, express or implied, or assumes any legal liability or responsibility for the accuracy, completeness, or any third party's use or the results of such use of any information, apparatus, product, or process disclosed, or represents that its use would not infringe privately owned rights. Reference herein to any specific commercial product, process, or service by trade name, trademark, manufacturer, or otherwise, does not necessarily constitute or imply its endorsement, recommendation, or favoring by the United States Government or any agency thereof or its contractors or subcontractors. The views and opinions of authors expressed herein do not necessarily state or reflect those of the United States Government or any agency thereof.

### Trademark Disclaimer

Reference herein to any specific commercial product, process, or service by trade name, trademark, manufacturer, or otherwise, does not necessarily constitute or imply its endorsement, recommendation, or favoring by the United States Government or any agency thereof or its contractors or subcontractors.

---

## PPPL Report Availability

### Princeton Plasma Physics Laboratory:

<http://www.pppl.gov/techreports.cfm>

### Office of Scientific and Technical Information (OSTI):

<http://www.osti.gov/scitech/>

---

### Related Links:

[U.S. Department of Energy](#)

[Office of Scientific and Technical Information](#)

# **Enhanced Confinement Scenarios Without Large Edge Localized Modes in Tokamaks: Control, Performance, and Extrapolability Issues for ITER**

R. Maingi, Princeton Plasma Physics Laboratory

## **Abstract**

Large edge localized modes (ELMs) typically accompany good H-mode confinement in fusion devices, but can present problems for plasma facing components because of high transient heat loads. Here the range of techniques for ELM control deployed in fusion devices is reviewed. The two baseline strategies in the ITER baseline design are emphasized: rapid ELM triggering and peak heat flux control via pellet injection, and the use of magnetic perturbations to suppress or mitigate ELMs. While both of these techniques are moderately well developed, with reasonable physical bases for projecting to ITER, differing observations between multiple devices are also discussed to highlight the needed community R & D. In addition, recent progress in ELM-free regimes, namely Quiescent H-mode, I-mode, and Enhanced Pedestal H-mode is reviewed, and open questions for extrapolability are discussed. Finally progress and outstanding issues in alternate ELM control techniques are reviewed: supersonic molecular beam injection, edge electron cyclotron heating, lower hybrid heating and/or current drive, controlled periodic jogs of the vertical centroid position, ELM pace-making via periodic magnetic perturbations, ELM elimination with lithium wall conditioning, and naturally occurring small ELM regimes.

## 1. Introduction

Controlled fusion research is taking a critical step toward power production with the construction and planned scientific program of the ITER<sup>1</sup>, an internationally-funded collaborative fusion facility. ITER and most future power producing tokamak reactor designs are based on operation in the “high confinement mode” (or H-mode)<sup>2</sup>, which also results in broad plasma pressure profiles that provide good global magnetohydrodynamic (MHD) stability, as well as high fractions of self-driven current, which reduces the external current drive requirements. In H-mode operation, the edge density, temperature, and pressure profiles display a stair-step structure referred to as the “pedestal”, characterized by a steep gradient in a narrow radial zone (“pedestal width”). Indeed it has been shown that the predicted fusion output power of ITER depends strongly on the temperature and density values at the top of the pedestal<sup>3</sup>.

While high pedestal-top pressure is desirable for good plasma performance, a MHD instability, the edge localized mode (ELM)<sup>4, 5</sup>, is routinely observed in present day devices. The ELM is thought to be driven<sup>6</sup> by either excessive edge pressure gradient (resulting in “ballooning” modes)<sup>7</sup> and/or edge current<sup>8</sup> (resulting in “kink” or “peeling” modes), where the edge current is self-generated by the pressure gradient (“bootstrap” current). The hottest and most dense H-mode discharges are plagued by periodic, large amplitude “Type I” ELMs<sup>9, 10</sup>, which typically release 5% (but as high as 10-20%) of the total plasma stored energy in a few hundred  $\mu$ sec, resulting in high repetitive heat and particles fluxes onto plasma facing components (PFCs). Studies combining data from present day devices have projected that naturally occurring Type I ELMs in ITER would release 20 MJ of plasma stored energy<sup>11, 12</sup>. On the other hand, materials response studies and calculations<sup>13, 14</sup> have shown that an ELM energy loss  $< 1$  MJ will be required to avoid unacceptable damage to the ITER PFCs. Hence, the development of ELM-suppressed and small ELM regimes has been emphasized in the international fusion research effort.

Over the past decade, excellent progress was made in the development of quasi-steady quiescent or ELM-suppressed H-mode discharges in tokamaks<sup>15-21</sup>, as well as techniques

to mitigate ELMs or trigger more frequent, small ELMs, along with the associated pedestal conditions<sup>22</sup>. The various techniques are discussed below, with highlighting of ELM pace-making with pellets, and ELM suppression with magnetic perturbations, as these are the baseline strategies planned for ITER. Furthermore advances in the last 2-3 years are stressed in this paper, as the implications for ELM control strategies in the context of ITER were recently reviewed<sup>23,24</sup>, and the projected capabilities over the range of plasma currents planned for ITER were recently updated<sup>25</sup>.

In the next section we explain the important elements of edge stability theory required to understand the effects of the density control techniques. In the subsequent sections, we review the multiple techniques used for ELM control, with an eye toward issues and required R & D for deployment in ITER. This paper targets a broad fusion audience, with an emphasis on a basic description of the current understanding of the physics involved with each strategy.

## **2. Background**

### 2a. Background on Edge Stability Theory:

Substantial evidence exists to support the hypothesis that ELMs are the consequences of exceeding stability thresholds for ballooning modes, kink/peeling modes, or coupled peeling-ballooning modes<sup>6,26,27</sup>. A typical set of edge pressure and current radial profiles, and a qualitative representation of an edge plasma stability boundary is displayed in Figure 1. The transition from the white “STABLE” region to the shaded regions in panel (b) represents the ideal stability boundary. The contours represent the growth rate of the fastest growing mode. The precise shape of the boundary depends on the details of the plasma boundary shape and profiles in panel (a), as well as the stabilizing effects of diamagnetic drifts. Stability curves such as these can be rapidly generated with modern analysis tools, such as the ELITE code<sup>26,28</sup>.

There is typically a limit associated with exceeding a critical edge pressure gradient (the x-axis), which results in short wavelength ballooning instability of the plasma on the low magnetic field side. There is also a limit observed with exceeding an edge current density

limit (y-axis), which results in a longer wavelength kink-like or peeling perturbation. In practice, the two instabilities combine to impose a corner in the upper right of the diagram, in which intermediate wavelength modes are driven both by the pressure gradient and current, termed “peeling-ballooning” modes. Note that the current and pressure gradient drives are not independent, in that the pressure gradient drives a self-generated bootstrap current, which is typically 50-100% of the local edge current density, depending partly on the edge collisionality. These modes typically exhibit a linear-growth phase, for which linear calculations can be used to compute instability thresholds, and non-linear explosive growth and detonation phases<sup>29-31</sup>. While such explosiveness is difficult to confirm experimentally, non-linear detonation is not needed for instability growth<sup>32</sup>, i.e. these modes should not be viewed as benign limits.

It is now widely accepted that violating the peeling and ballooning boundaries correlates with the experimental observation of ELMs. In practice ELMs reduce the edge pressure gradient and current, returning the plasma to a stable condition. There are a wide number of ELM types, however, with varying degrees of impact on the pedestal gradients, from large Type I ELMs, to medium Type III ELMs, and a number of small ELM regimes<sup>22, 23</sup>. Thus peeling-ballooning stability should be able to conceptually address these various ELM cycles. Figure 2a offers a qualitative explanation: large Type I ELMs are correlated with operation near the upper right hand corner of edge stability, leading to a relatively large relaxation. Intermediate-sized Type III ELMs could be correlated with current driven boundaries before achieving the maximum pressure gradient, and small Type II ELMs could be correlated with small excursions over the ballooning boundary, followed by a small relaxation. Similarly, figure 2b offers a qualitative explanation of mixed small Type II and large Type I ELM regimes.

Peeling-ballooning modes perturb the plasma over the entire width of the pedestal; thus from the pedestal standpoint, they can be viewed as global modes. These modes are destabilized by the free energy of the entire steep edge pressure gradient characteristic of H-mode (e.g. Figure 1a). Because these modes span the entire pedestal, they do not impose a limit on the pressure gradient at any given flux surface, but rather a limit on the

total pressure for a given profile width. It has been postulated that kinetic ballooning modes (KBM) provide the local pressure gradient constraint. The use of peeling-ballooning and KBM constraints was implemented in the EPED<sup>33-35</sup> model, which has successfully reproduced the edge pedestal operating space of many moderate and high aspect ratio ( $A=R/a$ ) tokamaks. The elements of this model are represented in Figure 3 for a particular equilibrium from DIII-D<sup>34</sup>. The peeling-ballooning limit on pedestal pressure is given by the solid black curve, while the KBM limit is indicated by the dashed curve. Conceptually discharges could evolve along the KBM constraint line, until the peeling-ballooning limit, i.e. the intersection of the two curves, is reached. Indeed the prediction of the maximum pedestal pressure (solid circle) is in good agreement with the maximum pedestal pressure in the last 20% of the ELM cycle from profile-constrained kinetic equilibrium<sup>36</sup>.

The types of edge stability diagrams discussed in this section will provide the basis for the ELM control schemes described below. Specifically the schemes will be categorized into:

- a) Forcing the plasma to go unstable due to a 2-D or 3-D perturbation, leading to a controlled, small ELM
- b) Maintaining the plasma in a stable portion of edge stability
- c) Expanding the stable operating space

While naturally occurring small ELM regimes remain attractive, the needed R&D for ITER was reviewed recently<sup>23</sup>, and recent studies not previously covered will be mentioned briefly at the end of section 6.

## 2b. Acceptable ELMs in ITER

Assessment of the size of ELMs acceptable for ITER has been refined to include the new PFC materials: W in the divertor and Be on the first wall<sup>25</sup>. Here a constant ELM size is used, i.e. there is no allowance for a few infrequent ELMs much larger than the mean. In this assessment, a critical parameter is the surface area over which ELM heat flux is deposited, i.e. the ‘wetted area’. Due in part to the technological challenges in

interpreting the rapidly evolving ELM heat flux, there have been substantially more studies of the inter-ELM heat flux width, and thus the assessment of acceptable ELM size has been made as a function of the ELM heat flux footprint normalized by the inter-ELM footprint ( $A_{\text{ELM}}/A_{\text{inter-ELM}}$ ), the latter of which is known to scale as  $1/I_p$ <sup>37-40</sup>.

A simple representation of the boundary between unacceptable and acceptable ELMs as a function of  $A_{\text{ELM}}/A_{\text{inter-ELM}}$  is shown in Figure 4. To create this figure, it was assumed that the relevant time scale of energy deposition is the ion parallel transport to the target, that the inter-ELM heat flux width varies as  $1/I_p$  as determined by recent multi-machine scalings, and that the ratio of inboard to outboard ELM heat flux is 2:1. The baseline value of the inter-ELM heat flux width,  $\lambda_q$ , was assumed to be 5 mm at  $I_p=15$  MA; we note that even this value is well above the 1 mm projections based on low recycling attached plasma conditions<sup>38,40</sup>. The magnitude of the x-axis was chosen to represent the range of  $A_{\text{ELM}}/A_{\text{inter-ELM}}$  reported in JET<sup>41</sup> and other tokamaks, although in some cases the heat flux width was shown to narrow during large ELMs in DIII-D<sup>42</sup> and NSTX<sup>43</sup>. The acceptable ELM limit was then set at 50% of the damage limit, which is 0.7 MJ or 0.2% of the plasma stored energy in ITER with  $I_p=15$  MA at  $Q=10$ ; this limit does not include thermal fatigue effects. The figure clearly shows that higher  $I_p$  is more likely to generate unacceptable uncontrolled ELMs, but the acceptable range increases with increasing ELM wetted area.

The requirements for controlled ELMs are summarized in Figure 5. Panel (a) shows that the natural ELM frequency (black squares) is projected to decrease with increasing  $I_p$  in ITER. The blue triangles represent the minimum ELM frequency needed to avoid W accumulation in the core (see ref. <sup>25</sup> for relevant details). The requirements for controlled ELMs are derived from the observation<sup>44</sup> that the product of ELM energy loss and frequency is a roughly constant fraction of power flow into the SOL, i.e.  $\Delta W_{\text{ELM}} \times f_{\text{ELM}} \sim (0.2-0.4) \times P_{\text{SOL}}$ , and that  $A_{\text{ELM}}/A_{\text{inter-ELM}}$  increases approximately as the square root of ELM fractional pedestal energy loss,  $\Delta W_{\text{ELM}}/W_{\text{ped}}$ . With these assumptions, the red circles represent the required controlled ELM frequency in ITER to avoid target melting; ELM frequency enhancement would be needed for  $I_p \geq 9$  MA. Panel (b) then shows the

required multiplier on the projected natural ELM frequency for acceptable ELMs, which is the larger of the ratios of the controlled ELM frequency to prevent target melting, and that needed to prevent tungsten accumulation in the core, normalized in both cases by the natural ELM frequency. Clearly achievement of controlled ELMs is anticipated to become more demanding as the  $I_p$  is increased in ITER, with a  $\sim 45x$  frequency multiplication (and equivalent reduction in ELM energy loss) needed at  $I_p = 15$  MA.

The outstanding research areas follow from these ITER projections. First understanding the physics governing the ELM wetted area is critical. Second, it needs to be determined if the ELM peak heat flux always decreases as  $1/f_{\text{ELM}}$  for the various ELM mitigation techniques. Finally understanding inter-ELM heat transport is critical in projecting the wetted area; in this regard, neoclassical drift-based limits project to narrower SOL footprints than ideal or kinetic ballooning limits.

### **3. ELM control with Pellets**

The efficacy of triggering ELMs with pellets from the tokamak low-field side has been known<sup>45</sup> since the mid-1990's; indeed high-field side injection<sup>46, 47</sup> or operation close to the H-mode power threshold<sup>48</sup> was developed mostly to improve fueling efficiency and/or reduce the ELM triggering probability.

The physics of the ELM triggering process is semi-quantitatively understood, leading to a controlled, small ELM; this technique can be placed in the 'Forcing the plasma to go unstable due to a 3-D perturbation' grouping discussed in the edge stability background section above. Figure 6 illustrates the conceptual picture<sup>49</sup>. Pellets are injected radially, vertically or tangentially into the plasma. Pellets ablate as they come into contact with substantial plasma temperature and fast ion content, with enhanced ablation rates at rational surfaces<sup>50</sup>. Thus at rational surfaces that are intersected by the pellet trajectory, an excess of electron density builds up inside the pellet cloud. This density equilibrates along the field line at the ion sound speed, i.e.  $\sim 1$  msec. On the other hand, the local electron temperature in the pellet cloud drops immediately because pressure is conserved

during the density increase. This local drop in  $T_e$  equilibrates along the field lines at the electron conduction speed, i.e.  $\sim 1-10 \mu\text{sec}$ . Thus the local electron pressure transiently bulges in the cloud. Figure 6c,d shows that a rather large radial pressure gradient can be obtained; this 3-D perturbation can destabilize ballooning modes, which would manifest as an ELM. This qualitative picture has been confirmed in non-linear reduced MHD simulations with the JOREK code<sup>51</sup>.

Excellent experimental progress has been made on multiplying the natural ELM frequency and reducing the ELM average size with small pellets<sup>52, 53</sup>. Figure 7 displays recent results<sup>52, 54</sup> from DIII-D, comparing a discharge with natural  $\sim 5$  Hz ELMs with one in which 60 Hz pellets were injected (blue lines in panel (b)). As shown in panels (a) and (b), the large peaks in deposited energy at the outer divertor and  $D_\alpha$  in the inner divertor due to the infrequent ELMs are eliminated. This is achieved with minimal impact on the H98 confinement multiplier and line-average electron density (panels (d) and (e)). A by-product of the more frequent ELMs with pellet injection is the reduction of impurity emission in the core, e.g. Ni-26 in panel (c).

The dependence of the ELM size and peak divertor heat flux from thermography on pellet injection frequency from DIII-D is shown in Figure 8. Panel (a) shows that the average ELM energy deposited in the divertor decreased at least as rapidly as  $1/f_{\text{pellet}}$ , while panel (b) confirms that the average peak heat flux during ELMs also decreased as  $1/f_{\text{pellet}}$ , at both the outer and inner targets. Note that the initial drop in peak heat flux with 20 Hz pellets was very large, with diminishing reduction in peak heat flux with subsequent increases in pellet frequency.

The use of pellets for ELM pace-making has been tested<sup>53</sup> in JET with the new ITER-like Be wall and W divertor, as shown in Figure 9. The natural ELM frequency in the target discharge was  $\sim 7-8$  Hz; 50 Hz pellets were requested at  $t=10$  sec. The ELM frequency responded rapidly, increasing to  $\sim 30-35$  Hz (top panel). The line-average density was unaffected, demonstrating that there was negligible fueling, while both the plasma stored energy and the H98 confinement factor were maintained. Thus, the natural ELM

frequency was increased by about a factor of 4.5 via pellet ELM pace-making in this discharge.

The impact on the peak heat flux in JET was much more subtle, however. Several characteristics of a discharge with small pellets (left hand column) are compared with a reference discharge (right hand column) in Figure 10. The top panels show that indeed, the ELM frequency was increased by a factor of 4-5. The ELM energy loss from equilibrium reconstructions was indeed reduced with pellet ELM-pacemaking, but the third row of panels shows that the peak heat flux was unchanged. This was due to a narrowing of the heat flux footprint, i.e. of the ELM wetted area, as the ELM frequency was increased. For completeness, it is noted that the fluency during ELMs, which is computed by integrating the ELM heat flux over its duration (and therefore more readily available), did decrease by about 33% during the 4-5x increase in ELM frequency<sup>53</sup>.

Furthermore the ELM triggering dynamics were quite different with the ITER-like wall, in that ELMs were successfully triggered effectively only  $\sim 10$  msec after the previous ELM, as compared to  $< 0.5$  msec with the carbon wall. These results on JET were confirmed with a new set of experiments and analysis of older experiments on ASDEX-Upgrade, in which tungsten wall pellet triggering dynamics were compared with carbon-wall observations<sup>55</sup>. Moreover new ASDEX-Upgrade experiments demonstrated that with nitrogen seeding (usually used for divertor heat flux management), the triggering dynamics and time scales approached those of the carbon wall results. While this difference in ELM dynamics is correlated with the metallic walls, the underlying physics is not understood. Thus this represents the largest single R & D need in pellet ELM pace-making that is at the heart of the viability of the scheme for ITER: reconciling the observed differences in the heat flux reduction and ELM triggering dynamics from DIII-D and JET, and the role of metallic walls, if any.

We conclude the discussion of recent results with a new development: the triggering and pace-making of ELMs in the EAST device with a novel lithium granule injector<sup>56</sup>. Figure 11a displays the schematic of the device. Basically  $\sim 1$  mm lithium granules are dropped

through a guide tube; a rotary motor then transfers radial momentum to the granules, toward the boundary plasma, with controllable speeds up to 100 m/s and frequencies up to 100 Hz. Figure 11b displays the time evolution of the  $D_\alpha$  emission; nearly every granule (vertical red line) triggers an ELM, as also shown in the spikes in visible Bremsstrahlung (VB) emission and extreme ultra-violet emission (XUV), in panels (c) and (d). This is the first demonstration of ELM pace-making with non-fuel pellets. Near term experiments in EAST will examine the effect of ELM pace-making on the divertor heat flux profiles and the edge plasma density, temperature and pressure profiles. Furthermore there is community-wide interest in modifying the injector to use beryllium or boron particulates.

Projections for the efficacy of ELM pace-making in ITER have been made with non-linear MHD calculations with the JOREK code<sup>25, 57</sup>. Validation studies using the full plasma geometry are based on the DIII-D results described above. These studies were initiated with a stable equilibrium with 70% of the pressure gradient of the maximum value of natural ELMs. Pellets of different sizes and speeds were simulated. Ballooning modes were triggered when the local pressure gradient exceeded a threshold that was well above the normal peeling-ballooning threshold for axisymmetric gradients prior to a natural ELM. This translates both into a critical pellet size for a given speed, and a critical speed for a given size. Figure 12a,b shows modeled perturbations to the density and flow fields, with panels (a) and (b) representing pellets that were below and above the critical size to destabilize the ballooning mode. Panel (c) shows the simulations of a pellet speed scan at the critical pellet size for ELM onset: the faster pellets penetrate further past the separatrix, and in this case beyond the top of the nominal pedestal. The slowest 25 m/s pellet requires the smallest relative pressure perturbation for ballooning mode triggering because it is centered in the pre-pellet steep gradient region. Note that the minimum pellet size needed for ballooning mode destabilization in JOREK is approximately 2-4 times larger, in terms of number of particles, than the minimum size observed in DIII-D. This discrepancy appears to be related to the toroidal resolution of the numerical grid, which limits the localization of the pellet ablation and pressure perturbation. Thus, validation could be improved by extending code capability and

resources to finer grids. Nevertheless, the minimum pellet size computed from JOREK should be viewed as an upper bound to the size needed for ELM triggering in other devices.

Figure 13 shows the ITER pellet injection geometry<sup>58</sup> and the JOREK calculations for ELM destabilization in ITER<sup>25, 57</sup>. Injection through the X-point region was chosen for ITER, and indeed this geometry was tested in the DIII-D experiments. Panel (b) shows the results of a calculation of the pressure perturbation as a function of pellet size: only the pellets at or above 3.7 mm size successfully destabilized ballooning modes in JOREK. Thus the ITER pellet triggering system specifies the need for 3.7 mm pellets with a minimum velocity of 350 m/s.

#### 4. ELM control with Magnetic Perturbations

Externally applied 3-D magnetic field perturbations (MP) have been shown to either suppress or mitigate large, Type I ELMs in DIII-D<sup>16, 17, 59-63</sup>, JET<sup>64-67</sup>, ASDEX-Upgrade<sup>20, 68-71</sup>, KSTAR<sup>72, 73</sup>, and MAST<sup>74-77</sup>. There are common characteristics in the way that the plasmas respond to the 3-D fields, but also apparent differences. This technique can be classified as “Maintaining the plasma in a stable portion of edge stability”, as discussed in the background section. For additional details, the reader is pointed to a couple of recent reviews of this area<sup>24, 78</sup>.

The effect of 3-D fields on the plasma appears to depend on the pedestal electron collisionality,  $\nu_e^*$ . Type I ELMs can be completely suppressed in DIII-D ( $\nu_e^* < 0.35$  and also  $\nu_e^* > 1$ )<sup>62, 63</sup> and in KSTAR ( $\nu_e^* < 0.5-1$ )<sup>72</sup>. The key requirements are 1) the edge safety factor is maintained in one of several resonant windows, and 2) the resonant magnetic perturbations (RMP) amplitude exceeds a threshold normalized radial field perturbation,  $\delta B_r/B_t$ . A common observation is that the loss of edge density (density “pump-out”) temporally precedes ELM suppression, although this phenomenon is not resonant in  $q_{95}$ . We first describe recent results for ELM suppression with MP, followed by ELM

mitigation with MP, and then conclude with experimental measurements of the displacements caused by the MP.

#### *4a. ELM suppression with RMP*

In DIII-D, a set of six internal coils above and below the midplane is available for MP, as is a set of six coils at the midplane outside the vacuum vessel. The combinations of these coils provide relatively good  $m,n$  spectral control, although only a subset of the coils is needed for suppression<sup>60</sup>. The applied 3-D field typically has toroidal mode number  $n=3$ , and so the relevant pedestal perturbations,  $\delta B_r^{m,n}/B_t$  are  $m,n \geq 10/3$  with an optimal  $q_{95} = 3.5$  for ELM suppression. A correlation is found between the RMP amplitude and ELM suppression that is attributed to the existence of a sufficiently large radial zone for the overlap of magnetic islands that are opened up with the 3-D perturbation (calculated neglecting the plasma response and shielding), across the pedestal region of the plasma<sup>59</sup>. For completeness we note the recent extension<sup>61</sup> of the DIII-D ELM suppression to RMP with  $n=2$ .

With the application of the RMP, the edge  $n_e$  pedestal is reduced in both height and width while the edge  $T_e$  gradient is only modestly increased (Figure 14a,b)<sup>17</sup>; hence the edge pressure and its gradient largely follow the changes to the  $n_e$  profile<sup>79, 80</sup>. The edge plasma profiles were fitted with modified hyperbolic tangent and/or spline functions<sup>36, 81</sup>. In short, the RMP reduces the pressure at the pedestal top and often narrows the pedestal width, enabling ELM-suppressed operation. Edge stability analysis has shown<sup>82</sup> that the ELMy discharges lie in the unstable region of overlap between peeling and ballooning modes while the RMP ELM suppressed discharges lie in the stable region (Figure 14c). The pedestal pressure, its gradient, and associated bootstrap current are all reduced in the RMP ELM suppressed discharges, which underpins the stability improvement.

The magnitude of the profile modification with RMP increases with the applied RMP amplitude. A dedicated scan of RMP amplitude was conducted<sup>59, 80</sup>. Figure 15 shows the time evolution of the divertor  $D_\alpha$  emission and ELMs for several values of  $\delta B_r^{11/3}/B_t$  and a reference discharge with  $\delta B_r^{11/3} = 0$  (panel (a)). The RMP was energized at  $t=1.8$  sec in

panels (b)-(f). While the RMP amplitude in panel (b) is below that needed for ELM suppression, the effect on ELM amplitude as measured by the height of the  $D_\alpha$  spikes is clearly visible when compared to the reference case in panel (a). Panels (c)-(f) show increasing RMP amplitudes; note that there is a temporal delay until ELM suppression is achieved, and that it generally decreases with increasing RMP amplitude. Panel (g) shows the evolution of the pedestal top density during this sequence; the magnitude of the density drop correlates approximately with the applied 3-D field.

A plausible explanation was recently offered<sup>83</sup> for the long-standing observation of the existence of limited  $q_{95}$  operational windows for ELM suppression. The basic picture is that a remnant island chain is responsible for enhanced particle transport with RMP near the top of the pedestal. This enhanced transport would prevent the pedestal width from expanding in the inter-ELM cycle to the point where a peeling/ballooning mode would have been destabilized. Figure 16a,b displays the concept in the context of the EPED model discussed in the background section. A normal ELM cycle would occur when the KBM constraint (dashed green curve) crossed the peeling-ballooning limit (solid blue curve), resulting in an ELM crash and re-build. If a remnant island chain were just inside the top of the unperturbed pedestal (central orange shaded region in Figure 16b), then pedestal expansion would be arrested, allowing stable operation just below the stability limit. This is precisely the region where the electron perpendicular rotation frequency  $\omega_E$  typically crosses zero, which facilitates the formation of the island chain<sup>84</sup>. Here  $\omega_e = \omega_{\text{EXB}} + \omega_{*e}$ , where  $\omega_{\text{EXB}}$  is obtained from charge-exchange recombination spectroscopy via the lowest order radial force balance, and  $\omega_{*e}$  is the standard diamagnetic drift frequency proportional to the electron pressure gradient. An example of the radial profile of these various drift frequencies is published in ref. <sup>84</sup>; typically crosses  $\omega_e$  zero between  $\psi_N$  of 0.85-0.95. If the island chain were too far down the steep gradient region (orange shading on left hand side), then the electron rotation would screen out the island, preventing formation. If the island chain were too far in beyond the top of the pedestal, it would not prevent the pedestal re-building back up to the peeling-ballooning limit and ELM onset. Resonant windows emerge from this picture as various island chains (e.g.

12/3, 11/3, 10/3 in Figure 16c) are allowed to form near the pedestal top with varying  $q_{95}$ . When such island chains are in the optimal position to restrict pedestal expansion, which is  $0.96 < \psi_N < 0.97$  for these DIII-D discharges, an ELM suppression window would be predicted. The lightly shaded regions in Figures 16c,d are the predicted ELM suppression windows from these arguments, whereas the dark shaded regions represent the experimentally observed resonance windows: there is good agreement between this simple model prediction and the observed  $q_{95}$  resonances. One caveat is that the measured pedestal pressure width did not vary substantially just inside or outside the ELM suppression resonance windows in Figure 16b,c. This is not a critical discrepancy, however, as the actual difference in the widths on different sides of the resonance windows may be beyond measurement accuracy.

ELM suppression has also been realized with RMP in the KSTAR device. KSTAR has a 3 poloidal x 4 toroidal set of in-vessel control coils for MP experiments. Large ELM suppression has also been achieved in KSTAR, first with  $n=1$  RMP<sup>72</sup> and more recently with  $n=2$  RMP<sup>73</sup>. Resonances in the  $q_{95}$  window have been observed as in DIII-D. Figure 17 shows a comparison of a discharge with RMP ELM suppression to a reference ELM discharge. The three rows of internal coils that enable the 3-D field are activated from  $\sim 3.2 - 4.2$  sec. During the initial period of coil activation from 3.2 sec-3.6 sec, ELMs become less frequent and larger, as can be seen from the  $D_\alpha$  trace in panel (b). ELM suppression is observed  $\sim 100-200$  msec after all three coils are activated. There is an initial density pump-out, but the density re-builds as the ELM frequency goes down toward zero, rather like an ELM-free H-mode. The plasma stored energy first drops and then recovers during the ELM-free phase, while the central toroidal rotation speed  $V_{\text{tor}}$  remains modestly lower than in the reference discharge. Large ELMs resume following de-activation of the coils at 4.25 sec.

Figure 18 shows an expanded time frame during the coil turn on phase for another KSTAR discharge. The transition to ELM-free operation occurs during the shaded region in panels (a) from 3.75 – 3.95 sec. There is a very small drop observed in the edge  $T_e$  during this transition phase, both the average value and also the minima and maxima

during the ELM cycles. However a substantial increase in the fluctuation level of the  $T_e$  signal can be observed in the transition and ELM suppressed phase (panels (a), (b)), which is attributed to an increase in the plasma turbulence. Panels (c) highlight the difference in filamentary structure with large ELMs (left hand side) and no ELMs (right hand side) from the ECE imaging diagnostic<sup>85</sup>.

These new results from KSTAR supplement and extend the DIII-D results in several ways. First they provide a demonstration of ELM control with a very low- $n$  perturbation, which has some appealing aspects. Second they demonstrate recovery of the density after pump-out during evolution of the H-mode. Edge profile and stability analysis is needed for understanding of these results in the context of DIII-D and other results.

A recent noteworthy development is the demonstration of ELM suppression with less than a full complement of control coils in DIII-D<sup>86</sup>. A previous study demonstrated suppression with a single row of internal coils<sup>60</sup>; in this study, coils were deactivated in a pseudo-random manner and ELM suppression was demonstrated with as few as 5 active coils out of the normal set of 12 internal coils. The computed toroidal and poloidal spectrum was impure, with the appearance of substantial low- $n$  sidebands. Detailed analysis of the impact of these sidebands in enabling ELM suppression with moderate coil currents has commenced. The results provide semi-quantitative corroboration of an analysis<sup>87</sup> that predicted the achievement of the vacuum overlap island width criterion<sup>59</sup> (thought to be needed for ELM suppression in ITER) even with the failure of multiple internal coils.

#### *4b. ELM mitigation with MP*

ELM mitigation with MP has been achieved on ASDEX-Upgrade, DIII-D, JET, and MAST, with a variety of applied MP spectra and ranges of dimensional and dimensionless parameters. Details of recent progress from these devices are given here.

A set of 2 poloidal x 8 toroidal in-vessel saddle loop coils are installed in ASDEX-Upgrade. Mitigation of large ELMs was obtained with every other toroidal coil, in an  $n=2$

configuration. However these results appear to be insensitive to the magnitude of the resonant components of the applied perturbation. Figure 19a shows time traces of MP amplitude ramp experiments with even parity (up/down symmetric current distribution) and odd parity (up/down current distribution out-of-phase toroidally). Figure 19b shows the poloidal spectrum of the applied fields, with a strong variation in the edge resonant components at the 9/2, 10/2, and 11/2 flux surfaces (vacuum field calculation neglecting plasma response). ELM mitigation was observed with either of these poloidal spectra, at approximately the same current amplitude. A hysteresis in the MP amplitude is evident in both cases. Also there was no evidence of density pump-out with the MP. Additional experiments have shown that in the range of  $\nu_e^* \geq 1$ , the critical access condition for ELM mitigation with MP is achievement of line-average density normalized to Greenwald scaling<sup>88</sup>  $n/n_{GW} > 0.65$ . Gas-puffing experiments have recently shown that mitigated ELMs can also be achieved at  $n/n_{GW} > 0.77$  without MP<sup>68</sup>, and pellet fueling experiments have succeeded in extending the  $n/n_{GW} \geq 1.5$  with central density peaking<sup>89</sup>.

Edge profile and stability analysis of the mitigated ELM regime with MP has shown access to a new operational space in terms of pedestal  $T_e$  and pressure gradient. Figure 20 compares the data in this operational space with and without MP, and large and small ELMs. The light blue line indicates the empirical stability threshold for small ELM regimes. The purple/pink line indicates the onset of large ELMs, likely due to violation of peeling-ballooning stability limits. The discharges marked in the red oval indicate access to an enlarged operational space with MP and small ELMs (red  $\times$ ) and relatively high pedestal  $T_e$ , but below the large ELM pressure gradient limit. The reduced gradients with small ELMs and MP are correlated with a  $\sim 30\%$  increase of edge  $\chi_e^{\text{eff}}$ .

To date, however, no resonant ELM suppression windows have been found with  $\nu_e^*$  down to 0.5 in ASDEX-Upgrade; central heating and edge gas puffing to control the central tungsten concentration has made access to  $\nu_e^* < 0.5$  unachievable<sup>90</sup>. An upcoming divertor geometry modification should improve impurity control and access to lower  $\nu_e^*$ .

MP can be applied in JET with a 1 poloidal x 4 toroidal row of midplane coils, allowing  $n=1$  or  $n=2$  toroidal mode numbers. ELM mitigation has been achieved with both of these configurations, with an ELM amplitude reduction of more than 70%<sup>64-67</sup>. In addition, density pump-out is observed above a critical MP amplitude. Figure 21 shows time evolution for a discharge with a ramped MP application. During the MP amplitude ramp, reductions in radiated power and  $D_\alpha$  emission can be observed in panels (d) and (e) respectively. Panels (f) and (g) compare the evolution of the pedestal  $T_e$  with Type I ELMs and mitigated ELMs; overall there is a measurable reduction in the ELM transient with MP, but also in the baseline pedestal  $T_e$  between ELMs. Panel (h) shows a PDF of ELM size in type I ELMy and mitigated ELM conditions; the most probable peak heat flux was reduced by more than 60% in the mitigated ELM case. While mitigation can be obtained over a wide range of  $q_{95}$ , there are multiple resonances observed in the mitigated ELM frequency as a function of the safety factor<sup>65</sup>. An engineering assessment of in-vessel off-midplane coils for greater poloidal spectral control is continuing, but the installation decision has not yet been confirmed.

ELM mitigation in DIII-D was observed<sup>91</sup> well before ELM suppression was achieved. There are, however, differences in the nature of the changes to  $D_\alpha$  emission observed in DIII-D with respect to observations in ASDEX-Upgrade and JET. In DIII-D the discrete ELMs were replaced with bursty, turbulence-like events, with minimal drops in stored energy per event. Nonetheless occasional type I ELMs were observed, i.e. large ELMs were not uniformly eliminated<sup>91</sup>.

A set of six toroidally spaced in-vessel coils above the midplane and 12 toroidally separated coils below the midplane have been installed for MP experiments in MAST<sup>77</sup>. Figure 22 shows a summary of experimental results and edge stability analysis. Panel (a) compares two boundary shapes used in the experiments: connected double-null (CDN) and lower-single (LSND). In the CDN shape,  $n=3$  up/down symmetric fields were applied for this experiment, whereas  $n=6$  was applied from the lower row of coils only in the LSND shape. Panels (b)-(e) show the evolution of discharge parameters for a

reference large ELM discharge (black) and one with mitigated ELMs (blue) applying  $n=6$  in LSND configuration. Panels (f) – (i) display a reference ELMy discharge (black) and ELM mitigated discharge (green) in CDN configuration with  $n=3$ . Density pump-out is clearly observed with MP in the LSND case, but not in the CDN case; this suggests that density pump-out is not critical to ELM mitigation.

Peeling-ballooning stability analysis with the ELITE code is shown in panels (j), (k). Analysis of the reference ELMy discharge in both configurations (LSND in panel (j) and CDN in panel (k)) is shown by the black curves and data-points. It can be seen that the reference points lie near the peeling/ballooning stability boundary. In contrast the computed mitigated ELM discharge boundaries (red curves and data points in both plots) lie relatively far from their stability boundaries. One resulting hypothesis (to be tested) is that 3-D effects modify the edge stability in such a way that small ELMs are triggered with the MP, i.e. before large ELM onset can occur.

While the effects of ELM suppression in the previous section appear as ‘resonant’ phenomena, i.e. when the safety factor profile is aligned so that the relevant  $n$ -number and associated  $m$ -number along magnetic field lines occurs at the top of the pedestal, there is no uniform correlation of ELM mitigation with field-line pitch resonances. Specifically, there is no evidence of a resonant character in ASDEX-Upgrade, DIII-D, or JET with a carbon wall. On the other hand the natural ELM frequency in JET exhibits substantial, possibly resonant structure<sup>65</sup> as a function of  $q_{95}$ , as does ‘density pump-out’ and the appearance of striations near the X-point<sup>77, 92</sup> in MAST.

Thus there are many observations of ELM mitigation and a few of ELM suppression via MP from existing devices. A common theoretical framework to understand these results is still lacking, however. In particular there is no unifying view of ELM mitigation from the conventional peeling-ballooning stability perspective (e.g. the results described for the MAST device above). An important element of a theory will be to incorporate both effects of the applied field, and plasma response to those fields, discussed below.

#### *4c. Measurements of plasma displacements*

Many of the calculations used to guide experiments with MP are done with vacuum field modeling, which means that a superposition of the 2-D equilibrium and the computed 3-D perturbations from field line tracing are used to construct the 3-D magnetic topology. Calculations have shown, however, that the plasma responds to resonant magnetic fields in certain ways, screening them when rotation is sufficiently high or amplifying them at sufficiently high pedestal  $\beta$ <sup>84, 93-98</sup>. Experimental confirmation of these predicted effects is needed for predictive understanding of the role of RMP on plasmas.

Initial attempts to validate calculations focused on predicted ‘lobes’ or homoclinic tangles<sup>99</sup> in the vicinity of the X-point region. Indeed such lobes were observed in both visible light<sup>92</sup> and also in the ultra-soft X-ray region<sup>100, 101</sup>. Experimental evidence<sup>102</sup> of island chains and other 3-D topological modifications that may be present e.g. near the top of the pedestal in H-mode plasmas with RMP ELM suppression appears to now be possible with present day advanced diagnostics.

In principle the addition of 3-D fields to an axisymmetric equilibrium will generate 3-D topological changes, which manifest as a splitting of the separatrix into a couple of intersecting manifolds<sup>99</sup>. This topological change would result in 3-D structures on plasma fields, such as density and temperature. While it is difficult to accurately measure these relatively modest perturbations with finite channel diagnostics, high spatial resolution imaging diagnostics can distinguish such structures, assuming sufficient signal-to-noise. Such data was obtained with a soft X-ray (SXR) imaging diagnostic<sup>103</sup> on DIII-D, and compared with MHD calculations via a synthetic diagnostic.

Figure 23 compares<sup>84</sup> evidence of magnetic perturbation effects with soft X-ray (SXR) imaging data<sup>103</sup> near the X-point and Thomson scattering profile data above the outer midplane with calculations from the M3D-C1 resistive two-fluid MHD code. Emission in the SXR portion of the spectrum is a function of  $n_e$ ,  $T_e$ , and  $Z_{\text{eff}}$ .<sup>103</sup> Structures in the SXR emission from e.g. islands will appear as emission bright spots or holes. Panel (a) shows

the net SXR signal with subtraction of the two possible phases of the RMP, with a poloidal cross-section of the equilibrium overlaid. By subtracting the signal for the two RMP phases, the positions of the static islands, if they exist, would rotate; thus the subtraction is a tool to enhance the contrast of the SXR emission. Panel (b) shows a synthetic diagnostic rendering of the M3D-C1 calculations and a model for SXR emission for comparison: there is reasonable agreement in the size of the predicted structures in the X-point region, due to a remnant island chain, although the agreement away from the X-point is not so good. Panel (c) shows a comparison of two  $T_e$  profiles from Thomson scattering with the two different phases applied for the  $n=3$  MP (red, blue symbols) compared with the predicted profiles from M3D-C1 in the equilibrium (black), and alternate phases (blue, red). The overall agreement is only fair, noting that the predicted difference in radial displacements is 50-100% larger in the calculations.

While the recent progress and semi-quantitative level of agreement is encouraging, additional validation studies are still needed. Progress is limited by the available human resources, as these validation studies are labor intensive.

## 5. Naturally Occurring Quiescent Regimes

While the ELMy H-mode has the widest set of experimental observations from which to extrapolate to future devices, naturally occurring quiescent regimes devoid of large ELMs would represent attractive solutions if they can be meaningfully projected for ITER. In this section we discuss progress on research on the I-mode<sup>19, 104-109</sup>, the quiescent H-mode<sup>15, 83, 110-114</sup>, and the Enhanced Pedestal H-mode<sup>115-117</sup>. Another candidate regime, Enhanced  $D_\alpha$  (EDA) H-mode<sup>21, 118</sup>, is discussed briefly in section 6 as studies<sup>119</sup> have shown that small ELMs appear in EDA H-mode at sufficiently high  $\beta$ .

### 5a. I-mode

The “Improved” or I-mode operation has been observed in a number of devices and investigated in depth at Alcator C-Mod<sup>19, 104</sup>. It is characterized by the presence of a  $T_e$  pedestal without a density pedestal, leading to low  $v_e^* \sim 0.1$  at the top of the temperature

pedestal. The regime exists in a heating power region between L-mode and H-mode. Quasi-steady I-modes are most readily observed with the ion grad-B drift away from the dominant X-point, i.e. the so-called unfavorable drift direction that leads to an elevated L-H power threshold. I-modes have been obtained with ICRF heating, EC heating, and NB heating<sup>120</sup>.

The evolution of an I-mode discharge phase from Alcator C-Mod is shown in Figure 24 by the gray shaded region<sup>104</sup>. The time prior to the shaded region is L-mode, and the subsequent time is ELM-free H-mode. The  $D_\alpha$  level, radiated power, and line-average density remain at the L-mode levels, but the central  $T_e$  and energy confinement relative to the H98 scaling law both increase relative to L-mode levels. A new high frequency fluctuation, termed a weakly coherent mode (WCM), appears in the  $\sim 150$  kHz range.

Over the last few years, research has focused on characterization of the L-I and I-H power thresholds and operational windows<sup>107</sup>, expansion of the operational space of the regime<sup>121</sup>, and analysis of the edge stability<sup>108</sup>. Steady I-mode were obtained over a wide range of  $I_p$  (0.8-1.35 MA),  $B_t$  (3-6 T), density and plasma boundary shaping. The I-mode was maintained for up to two times the L-I power threshold, with edge  $T_e$  reaching as high as 1.1 keV. The edge  $n_e$ ,  $T_e$ , pressure, and parallel current density profiles were fitted/reconstructed with kinetic equilibrium fits, via techniques used widely in the fusion community<sup>36</sup>; these fits are shown in Figure 25. The profiles show in panels (a)-(d) are representative of the I-mode and H-mode radial profiles in C-Mod: the edge  $n_e$  in I-mode shows no barrier-like formation, while the edge  $T_e$  clearly shows a pedestal-like structure as in H-mode. The overall pedestal pressure and its gradient are lower in I-mode as compared to H-mode, as is the parallel current density, much of which originates from the bootstrap current driven by the pressure gradient. Panel (e) shows the results of stability analysis<sup>108</sup> of the kinetic equilibrium profiles with the ELITE code: the I-mode data are well separated from the peeling/ballooning stability boundary indicated by the purple transition region, consistent with the absence of ELMs in I-mode discharges. This is in contrast to ELMy H-mode discharges in C-Mod, which appear to be close to the ballooning instability boundary<sup>122, 123</sup>.

A comparison of the fluctuation characteristics<sup>121</sup> in L, I, and H-mode from Alcator C-Mod is shown in Figure 26. Panel (a) shows the amplitude of density fluctuations as a function of frequency for these three operational modes. While H-mode has the lowest fluctuation level, I-mode fluctuation amplitude is lower than L-mode, except in the high frequency range near the WCM. Panel (b) shows that the particle flux through the separatrix is correlated with the normalized amplitude of the WCM, suggesting that the WCM is at least partly responsible for the particle transport that prevents the edge density build-up observed in H-mode. Panel (c) shows an existence diagram for I-mode, and both L-I and I-H transitions, along with an L-H transition data point with ion grad-B drift toward the X-point for reference. Note that the L-I power threshold increases near linearly with line-average density, as also observed for the L-H power threshold<sup>124</sup>. The black arrow represents the trajectory of a particular discharge in which gas puffing was used to successfully increase the density in I-mode by 33%. Interestingly a subsequent discharge with a slight drop in ICRF power resulted in an I-H transition. This suggests that the strong  $T_e$  gradient up to 200 keV/m could be responsible for the high frequency fluctuations that increase particle transport and effectively prevent H-mode access. This increased particle transport applies to impurities, as well, in that impurity retention times in I-mode are comparable to L-mode, and well below EDA H-mode<sup>19</sup>. For reference, the measured  $T_e$  fluctuation levels are 1-2%, an order of magnitude below the  $n_e$  fluctuation levels<sup>109</sup>.

An assessment<sup>121</sup> of the accessibility of I-mode in ITER with ion grad-B drift away from the X-point was made with a set of assumptions based largely on data trends from C-Mod. The relevant operating boundaries were the L-I and I-H power thresholds, as well as total pedestal pressure limit when ELM would be destabilized. These calculations showed a possible operational window for ITER to access I-mode and achieve its  $Q=10$  goal.

For a more thorough assessment of the prospect of I-mode for ITER, I-mode studies demonstrating wide operational windows need to be completed in additional present-day

devices. A causal connection between the electron temperature gradient, the amplitude of the WCM, and the high particle transport rates needs to be demonstrated experimentally and computationally. Also, the implications of a peaked pressure profile, more than in H-mode, on global stability requires assessment. Finally access to a wide I-mode operating space in ITER would likely require reversed  $B_t$ ; the feasibility of that operational scenario needs investigation.

#### 5b. Quiescent H-mode

Quiescent H-mode (QH-mode) is a high-performance H-mode operating regime that is devoid of large ELMs, but still has acceptable impurity exhaust and density control<sup>15, 110</sup>. The individual ELMs are replaced by a continuous MHD mode. QH-mode was pioneered on DIII-D, and subsequently confirmed in ASDEX-Upgrade<sup>125, 126</sup>, JET<sup>127</sup>, and JT-60U<sup>128, 129</sup>. While initially restricted to NB injection counter to  $I_p$  and very low density, the operating window was broadened to include NB heating and toroidal rotation<sup>130</sup> in the co- $I_p$  direction, over a range of densities.

Several general characteristics of QH-mode discharges are shown in Figure 27. Panels (a)-(e) represent the temporal evolution of QH-mode discharge parameters with the commonly used counter- $I_p$  NB injection technique. MHD activity with  $n=3$  is observed during the QH-mode phase. Despite the lack of ELMs, line average density and radiated power are held constant. Panel (f) shows a spectrogram of oscillations in the magnetics signal, with prominent peaks at  $n=1$ ,  $n=2$ ,  $n=3$ , and  $n=4$ . The toroidal mode number of the dominant mode is not fixed; it has been observed to spontaneously shift during QH-mode, without a measurable change to the profiles. The modes are harmonic multiples of each other, and hence the instability has been named an “edge harmonic oscillation” (EHO). Beam emission spectroscopy and a radial sweep was used to determine that the radial location of the mode is very near the magnetic separatrix (inset in panel (f)).

The edge  $n_e$ ,  $T_e$ ,  $T_i$ , and pressure profiles in QH-mode are quite similar to the profiles during preceding ELMy phases, just prior to the disappearance of ELMs<sup>15, 110, 131</sup>. There is a stronger toroidal rotation and shear in the QH-mode than ELMy H-mode, and this is believed to provide the drive for the EHO, as described now. Standard edge stability

analysis was performed<sup>82</sup> with the ELITE code. It was found that the kinetically constrained equilibria were closer to the current-driven portion of the peeling-ballooning boundary (Figure 27g) than the pressure-driven portion. However the mode growth rates are sufficiently low that diamagnetic stabilization would be expected to prevent the explosive ELM instability. Furthermore it was found that the high rotational shear observed in QH-mode was destabilizing to the kink mode; the EHO can thus be interpreted as a non-linearly saturated, continuous kink mode that prevents the growth of discrete, explosive ELMs.

The main progress in QH-mode research over the past few years has been in DIII-D on the use of low or zero NBI torque scenarios coupled to 3-D fields, which exert an edge torque due to neoclassical toroidal viscosity<sup>132</sup>. Figure 28 shows the typical temporal evolution and other characteristics using this technique<sup>112</sup>. The NBI torque is initially negative to allow QH-mode access (panel (c)), but then is brought to zero as the 3D fields from internal I-coils and external C-coils are enabled (panel (a)). The QH-mode phase, i.e. devoid of ELMs, is maintained as shown in panel (b), while the confinement enhancement slowly grows during the discharge evolution (panel (d)). Toroidal rotation profiles from the purple and red shaded time windows are compared in panel (e); while the core rotation is drastically different, the edge rotational shear is maintained in both cases. An existence space of ELMy H-mode and QH-mode is shown in panel (f). Here the toroidal rotational shear for the C-VI impurity rotation speed (from charge exchange recombination spectroscopy) is plotted against the  $E \times B$  shear rate,  $\omega_E$ , normalized to the Alfvén frequency,  $\omega_A$ . An approximate threshold of  $\Delta\omega_E / \Delta r / \omega_A \sim 0.25 \text{ m}^{-1}$  is seen to separate the ELMy and QH-mode data, which can be interpreted as the experimental shearing rate needed for QH-mode access. Furthermore the toroidal rotation shearing rate for the measured  $C^{6+}$  species (y-axis in panel (g)) does not separate the ELMy and QH-mode data. There is a caveat: there was no direct measurement of the main ion (D+) rotational shear, however, and so main ion rotational shear cannot yet be ruled out as an ordering parameter.

An example<sup>114</sup> of an integrated scenario with ITER range co- $I_p$  NB torque is shown in Figure 29. Panel (e) shows that while negative NB torque was used to access the scenario, it was maintained as the torque was made more positive and non-resonant magnetic fields with the external C-coils were used to provide edge rotational shear. Examples of QH-mode sustainment with torque above, at and below the ITER equivalent value have been obtained. Note that the discharge maintains  $\beta_N \sim 2$  with  $H_{98y2} \sim 1.3$ , within the range needed for ITER to achieve  $Q=10$ .

Progress has also been made on extending QH-mode to higher density and higher Greenwald fraction<sup>133</sup>. This was accomplished with simple gas puffing once in QH-mode; there was no correlation measured with Greenwald fraction up to  $n/n_{GW}$  of 0.8. The extension of the operational window was done with strong plasma shaping. Finally impurity confinement in QH-mode was assessed<sup>134</sup>. Fluorine was injected via a gas puff as a low or non-recycling impurity, and it was shown that the core fluorine particle confinement time after gas puff termination was as low or lower than in comparable ELMy H-modes with overlapping density ranges. This rapid exhaust demonstrated the efficiency of the EHO in controlling the core impurity content.

There are several areas of R & D required for further extrapolation to ITER. First, access to QH-mode with ITER-relevant torque must be demonstrated; at present, the torque has been reduced only after QH-mode was accessed. Second, the onset condition of the EHO needs to be quantified to determine applicability to ITER. Finally, the relation between particle transport and EHO intensity needs to be determined, as other devices have measured EHOs with insufficient amplitude to provide acceptable impurity exhaust.

### 5c. Enhanced Pedestal H-mode

Another ELM-free operational regime discussed in the literature is Enhanced Pedestal (EP) H-mode, observed in NSTX<sup>115</sup> but not yet reproduced on other devices. In this scenario, an ELM typically provides a trigger for a confinement bifurcation in which the pedestal  $T_e$  and  $T_i$  increase substantially, while the rate of line-average density ramping slows substantially or is arrested. The temporal evolution of a relatively long-lived EP H-mode<sup>116</sup> is shown in Figure 30. The ELM trigger preceding the confinement transition is

marked with a dashed vertical arrow. Panel (b) shows that the line-density ramp is substantially reduced, panels (c)-(e) quantify that the stored energy and confinement are enhanced by up to 50%, and panel (f) shows that no ELMs occurred following the transition. The termination event at  $t \sim 0.87$  sec corresponded to  $\beta_N \sim 6.5$ , suggesting onset of either an internal kink or resistive wall mode. These discharges are distinctly more quasi-steady than the enhanced confinement, ELM-free H-mode scenarios with lithium conditioning in NSTX with substantial changes to the density profile<sup>18</sup>.

The strong increase in the edge temperatures is shown in Figure 31. Panels (a) and (b) shows the sharp increases in the  $T_e$  and  $T_i$  profiles respectively, with little impact on the edge  $n_e$  profile (panel (c)). Panel (d) shows a sharp increase in the toroidal rotation and its gradient, along with the formation of an inflection just inside of the separatrix. A working hypothesis is that the ELM trigger alters the magnetic equilibrium to allow a localized momentum drag near the edge. The local drag on toroidal rotation results in an increased rotational shear, which would reduce any residual H-mode turbulence. It is likely that the  $E \times B$  shear is the critical quantity, but analysis<sup>116</sup> has shown that the changes in the  $E \times B$  shear were dominated by the changes in the toroidal rotation profile, i.e. the changes in the poloidal rotation made a smaller contribution to the  $E \times B$  shearing rate. Figure 31e shows that the pedestal  $T_i$  is indeed strongly correlated with increasing toroidal rotation gradient from a number of EP H-mode discharges.

Recent research<sup>117</sup> into this operating mode has identified examples of EP H-modes that are quiescent for the duration of the heating phase. In fact, examples of confinement transitions with barriers formed anywhere from the separatrix to 10 cm inside the separatrix have been identified, suggesting the EP H-mode could be the result of a superposition of a large radius internal transport barrier with the H-mode edge barrier. Correspondingly a strong correlation between the  $T_i$  gradient and the toroidal rotation shear has been established, consistent with the trend in Figure 31e. Furthermore a broad operational space of EP H-modes in  $q_{95}$  and collisionality space has been identified, and it has been determined that ion transport is at or below computed neoclassical transport rates. Fluctuation changes in EP H-mode are subtle: fluctuations appear to be slightly

higher in EP H-mode than in H-mode, suggesting that those fluctuations might be responsible for the observed increase in particle transport.

Extrapolating to future devices with the present database is problematic, however, because of the lack of detailed understanding of the dynamics of the transition and sustainment phases. Additional experiments are anticipated in the NSTX-Upgrade<sup>135</sup>, which commences operation in 2015.

## **6. Other ELM control: active and naturally occurring**

A number of alternate techniques have been developed for control of large ELMs, both active and passive via operational spaces. These techniques include supersonic molecular beam injection (SMBI)<sup>73, 136, 137</sup>, edge electron cyclotron heating (ECH)<sup>73, 138, 139</sup>, lower hybrid heating and/or current drive (LHH, LHCD)<sup>140, 141</sup>, controlled periodic oscillations of the vertical centroid position (jogs)<sup>73, 142-146</sup>, ELM pace-making via periodic magnetic perturbations<sup>147-154</sup>, modification of edge profiles and stability with lithium wall coatings<sup>18, 155-167</sup>, and the use of naturally occurring small ELM regimes<sup>23</sup>. Each of these is described below.

### 6a. Supersonic molecular beam injection

Supersonic molecular beam injection (SMBI) consists of a source, e.g. a free-flowing gas jet, that is accelerated to high local velocities and Mach numbers via a pressure difference through a constricting nozzle<sup>136</sup>. The average gas jet velocity exceeds those from thermal gas injectors, which translates to deeper penetration into high temperature plasmas. As long as the gas jet can penetrate past the separatrix in H-mode plasmas, or indirectly alter the profiles inside the separatrix, ELM control with SMBI can be considered in the portfolio of ELM control tools.

SMBI has been used to ameliorate ELMs in a number of devices, including HL-2A<sup>137, 168, 169</sup> and KSTAR<sup>73, 169</sup>. An example of ELM mitigation with SMBI from HL-2A is shown in Figure 32. After the SMBI pulse in panel (a), the  $D_\alpha$  reflects modification of ELM activity for a characteristic influence time,  $\tau_1$  (panel (b)). During this period, both the time

between ELMs and the ELM amplitude decrease (panels (c) and (d)). The overall energy confinement time is unaffected, while the line-average density increases for a time considerably longer than  $\tau_I$ .

The effects of the SMBI on divertor heat flux and the  $n_e$  profile are shown in Figure 33. Panel (b) shows that the inter-ELM peak heat flux  $Q_{div}$  drops by  $\sim 50\%$ ; it appears that the heat flux during the ELMs themselves are not resolved by the diagnostic. Also, it can be seen from panel (d) that the  $n_e$  gradient following SMBI ( $t=722$  msec) was reduced, followed by a gradual recovery. Similar  $n_e$  profile effects were observed in KSTAR. Additionally the toroidal rotation was decreased following SMBI pulses, but recovered between pulses. Finally in KSTAR high frequency  $n_e$  fluctuations from beam emission spectroscopy increased, while low frequency oscillations were reduced<sup>73</sup>.

A sandpile model<sup>170</sup> was constructed to understand the amelioration effect of SMBI on ELMs. In this model, source deposition just at the foot of the pedestal, i.e. just inside the separatrix, destabilizes small-scale transport events that prevent the buildup of gradients until a large-scale event is reached. This type of model qualitatively reproduces several features of the experimental observations.

One substantial difference worth noting is the large observed difference in  $\tau_I$  between EAST and KSTAR<sup>169</sup>. The ratio of the characteristic influence time described above to energy confinement,  $\tau_I / \tau_E$ , was measured as  $\sim 1$  in HL-2A, and much larger  $\tau_I / \tau_E \sim 2-3$  in KSTAR. Separate estimates of particle confinement time  $\tau_p$  have shown that  $\tau_I / \tau_E \sim 1$  and  $\sim 2.4$  in HL-2A and KSTAR in the experimental conditions. This implies that  $\tau_I / \tau_p \sim 1$  in both devices, qualitatively consistent with the conclusion that particle transport events are responsible for ELM amelioration in both devices.

Looking ahead, SMBI for ELM control in future high power & density devices appears problematic, as penetration to the separatrix would be difficult unless the mean velocity approached speeds near shallow pellet injection, in the range of 100 m/s. Additionally

assessment of the quantitative applicability of sandpile-type models on particle transport and density gradient relaxation is needed for projections.

### 6b. ECH/ECCD

Edge Electron Cyclotron Heating (ECH) and/or Electron Cyclotron Current Drive (ECCD) can be used to modify the edge pressure and current profiles, and stability via e.g. Figure 1. The edge heating would modify the local temperature and pressure gradients (and associated bootstrap current), while current drive could modify the edge current profile directly. Here we will focus on ECH studies since achieving localized current drive in the pedestal region is difficult, and dedicated ECCD studies yielded similar effects on the pedestal as compared to ECH studies<sup>138</sup>. Typically experiments to test this method rely on steering of in-vessel mirrors to alter the deposition locations; once these deposition locations approach the edge plasma, effects on the ELM amplitude and frequency can be observed.

ECH has been shown to alter ELM amplitude and frequency in a number of devices, including ASDEX-Upgrade<sup>138</sup>, TCV<sup>139</sup>, and KSTAR<sup>73</sup>. Recent progress from TCV experiments is shown in Figure 34. The time evolution plot is color-coded: the peach shaded region has constant ECH power and a constant launcher angle. A dynamic scan of the launcher angle during the green shaded region is shown in panel (a): the launcher angle is reduced, while the  $\rho$  value of the flux surface of maximum deposition increases. A consequence of the deposition scan toward the edge is that absorbed power from second harmonic ECH is reduced with time, as shown in panel (b). The ELM frequency (amplitude) increased (decreased) during the ECH deposition scan, in the opposite direction expected for Type I ELMs with decreasing heating power (panels (d) and (e)). This suggests that the ECH indeed affected ELM stability, leading to faster, smaller ELMs. Confinement decreased, while density remained constant (panels (f), (g), (h)).

The prospects for ECH ELM control in ITER are, however, rather limited, as current drive phasing doesn't seem to be especially more effective than heating phasing in present experiments<sup>131</sup>. Heating phasing used in the edge plasma can suffer from

imperfect absorption by the edge plasma, which can lead to substantial power on in-vessel components that may not be designed for such loads<sup>23</sup>.

### 6c. LHH/LWCD

Another set of waves used for heating and current drive is in the lower hybrid (LH) range of frequencies. As long as a wave accessibility criterion for the parallel refractive index  $n_{\parallel}$  is met, some level of heating and current drive via electron Landau damping can be expected. These systems are typically designed for core heating and current drive, and can contribute to magnetic shear optimization<sup>171</sup>, e.g. in JET. At excessively high densities, however, the LH wave can be absorbed in the SOL instead of the main plasma.

In the Alcator C-Mod tokamak, LH waves routinely affected the H-mode pedestal, leading to reduced density and particle confinement at constant energy confinement<sup>172</sup>, i.e. the temperature increased to compensate for the density pump-out. The rotation profile also was observed to go strongly in the counter- $I_p$  direction<sup>173</sup>. These studies were performed in Enhanced  $D_{\alpha}$  H-mode plasmas<sup>21, 118</sup>, and so the effect on ELMs and edge stability was not a focal point.

Recently, it was observed that the application of LH waves to EAST ELMy H-mode discharges strongly affected the ELM characteristics<sup>140, 141</sup>. Figure 35 shows the response of the ICRF heated H-mode plasma to modulated LH heating. The phases with LH heating have modestly higher stored energy (panel (d)) but nearly all of the ELM activity is eliminated (panels (e) and (f)). The reference discharges have ELM frequency  $\sim 150$  Hz, and this goes to zero in most cases, with a few observations of very rapid ELMs at  $\sim 600$  Hz. In addition, application of LH waves resulted in the formation of five helical, pitch-angle aligned current-carrying filaments in both L-mode and H-mode discharges<sup>140</sup>. Furthermore, thermographic measurements have identified the occurrence of strike point splitting, similar to observations with applied magnetic perturbations. The local of the striations is consistent with field line tracing of the 3-D effect of the SOL filaments on the magnetic topology.

The observed ELM modification appears to be a resonant phenomenon<sup>141</sup>, one signature of which is a marked dependence of results on  $q_{95}$ . The results of a  $q_{95}$  scan in EAST with applied LH is shown in Figure 36. Clearly suppression is observed for substantial fractions of the LH phases at the lower  $q_{95} \sim 3.8$ , whereas LH phases in the higher  $q_{95}$  values can result in destabilization of rapid, small ELMs.

Applicability to future devices depends on an integrated scenario design accessible to LH waves, along with sufficient LH power to reproduce the striations observed in EAST. The extent to which damping of the LH waves in the SOL is needed for the formation of the observed filaments needs assessment. If SOL damping turns out to be a crucial ingredient for the positive LH modifications, then optimization for future devices would be needed to prevent excessive current and plasma flux to the divertor PFCs.

#### 6d. Vertical Jogs

Rapid movement of the plasma centroid, also referred to as “vertical jogs”, has been used to manipulate the natural ELM frequency in a number of devices. The idea is that the movement affects the equilibrium profiles and current in a way that destabilizes peeling/ballooning modes in a controllable manner. Devices that have demonstrated the effectiveness of jogs include TCV<sup>142</sup>, ASDEX-Upgrade<sup>143</sup>, JET<sup>144</sup>, NSTX<sup>145</sup>, and KSTAR<sup>73</sup>.

The time traces from a pioneering example<sup>142</sup> of ELM triggering via jogs from TCV is displayed in Figure 37. A pair of up-down symmetric internal coils was used to apply perturbations that resulted in magnetic axis oscillations with a programmed ramp in the time between pulses from 7 msec to 3 msec (dashed lines in panels (c)). The two columns represent two different magnitudes of applied currents in those coils; the magnitude of the input perturbations was 4x higher in the right hand set of panels. The time between ELMs in panel (c) left-hand-side comes down during the programmed perturbation frequency ramp, but doesn't lock to the ramp frequency. In comparison, the higher amplitude perturbation on the right-hand-side in panel (c) mostly locks to the programmed frequency ramp. Panels (d) display the time delay from each perturbation to

the next ELM. There is no direct correlation in the left-hand side panel, but the right-hand side panel mostly comes to a delay between 2 and 3 msec, indicating synchronization to the applied perturbations. This work also showed that the ELM amplitude as measured by the  $D_\alpha$  spike also correlated directly with the time between ELMs. Finally a simple model of the ELM cycle showed good agreement with the time/frequency characteristics of the ELM response to the programmed perturbation frequency ramps, but the model did not include time dependent stability analysis of equilibria used for edge stability evaluations which have become community standards over the past  $\sim 5$  years.

In recent years, the technique has been adapted and further developed in the JET device<sup>144</sup>. Figure 38 shows a comparison of jogs (also known as “kicks”) with other ELM control techniques: magnetic perturbations from error field correction coils (EFCC), and gas injections. It can be seen in panel (a) that the ELM size as measured by the pedestal energy fractional drop decreases with increasing ELM frequency in a similar way for all of the techniques shown. Panel (b) shows that the jogs are consistent with high normalized energy confinement  $H_{98y2}$  up to 1.2, over a range of density normalized to Greenwald density limit scaling between 0.4 and 0.65. The high H-factor is common to jogs and natural ELMs, but application of MP, gas, and combinations of the two result in modest but measurable confinement degradation.

The initial results on TCV<sup>142</sup> and subsequent results on NSTX<sup>145</sup> showed ELM triggering with upward movement of the magnetic axis, consistent with increased edge current leading to the destabilization of current driven modes. However the results on ASDEX-Upgrade and JET showed preferential ELM triggering with downward movement of the axis<sup>23, 143</sup>. In-depth analysis of the ASDEX-Upgrade data<sup>23</sup> including the in-vessel passive stabilizing plates indicated a deformation of the flux surfaces leading to changes in the “squareness”<sup>174</sup> of the last closed flux surface, which destabilized edge modes during the downward axis movement. To date, there is no community-wide consensus on the underlying physics of the triggering.

The capabilities of ITER to utilize vertical jogs for ELM control via the in-vessel vertical stability coils was recently assessed<sup>25</sup>. At full current  $I_p=15$  MA, the potential effectiveness of this technique was evaluated as limited, but its use during the early phase of ITER operation with  $I_p$  of 5-10 MA to control W central accumulation was identified. The major impediment for a detailed evaluation for ITER and future facilities, however, is the lack of an accepted physical explanation that would unite the observations from the many present-day devices.

#### 6e. MP ELM pacing

While magnetic perturbations are presently deployed in attempts to suppress or at least mitigate ELMs, these can also be used to destabilize ELMs and increase the natural ELM frequency. The first reports of ELM destabilization from 3-D fields were from JFT-2M<sup>147</sup> and COMPASS-D<sup>148</sup>, and the techniques were further developed and refined in NSTX<sup>151-153, 175</sup> and DIII-D<sup>150, 154</sup>.

In NSTX, the application of sufficient pre-discharge lithium conditioning to plasmas facing components resulted in ELM-free H-mode with impurity accumulation and radiated power ramps (see the next section for details of elimination of ELMs with lithium conditioning). The discharges could be made into quasi-steady H-modes through the controlled re-introduction of ELMs with magnetic perturbations. Time traces for a discharge in which short-pulse square-wave  $n=3$  magnetic perturbations from external window-frame coils are used for ELM pace-making in an otherwise ELM-free discharge are shown<sup>152</sup> in Figure 39. Three discharges are compared: a reference ELM-free one with impurity accumulation (black traces), one with 10 Hz paced ELMs (red traces), and one with 30 Hz paced ELMs (blue traces). Both of the pacing frequencies reduce the radiated power to acceptable levels (panel (c)), and the higher frequency pacing further reduces the line average density ramp (panel (b)). This technique was successfully deployed up to a frequency of 62.5 Hz, although the efficiency for triggering ELMs with each pulse declined at the highest frequencies<sup>153</sup>.

In DIII-D,  $n=3$  perturbing fields with sinusoidal programming with frequencies up to 200 Hz were successfully used for ELM pace-making<sup>154</sup>. A common observation in NSTX and DIII-D was reduction of peak heat flux with increasing perturbation frequency, although the reduction appeared to saturate at the higher ELM frequencies. Figure 40 shows aspects of the DIII-D results as a function of applied perturbation frequency<sup>154</sup>. Panel (a) shows that the reduction in the divertor peak heat flux tends to saturate with increasing perturbation frequency,  $f_i$ . At face value, the result is discouraging, but it is noteworthy that the efficiency in pacing ELMs also drops with increasing  $f_i$  (panel (b)). Thus as the ELM pacing became less effective, larger ELMs were observed. The product of the ordinates from panels (a) and (b) is plotted in panel (c); the curve in green is the ratio of the natural ELM frequency,  $f_0$  ( $\sim 40$  Hz for the reference discharges), and twice the value of  $f_i$ . This curve suggests that further reductions in peak heat flux could be obtained at improved pacing efficiency. When the ELM size (from  $\Delta W/W$ ) is plotted against actual triggered ELM frequency in NSTX, a reduction is evident, although not as strong as the hoped-for direct inverse relationship with ELM frequency<sup>153</sup>.

The physics of the ELM triggering is not completely clear. In NSTX, the application of the 3-D fields increased the edge electron pressure gradient by 30% just prior to ELM onset in certain classes of discharges with magnetic perturbations just above the threshold needed for destabilization<sup>151</sup>. The possible extension of the conventional 2-D peeling ballooning calculations to 3-D may be required for in-depth understanding. Along these lines, the application of stellarator-type 3-D equilibrium and transport codes to ELM destabilization with magnetic perturbations in tokamaks is just commencing<sup>175</sup>. In addition to the lack of in-depth understanding of the destabilization phenomenon, there is an observed side-effect of rotation drag from the applied 3-D fields. Indeed the destabilization of locked modes or slowly rotation core modes was exacerbated with the magnetic perturbations for ELM triggering in NSTX<sup>153</sup>. For ITER and other future devices, the capability to cycle the appropriate coils fast and frequently enough for ELM triggering at desired frequencies, and the concomitant impact on coil reliability would need thorough assessment.

## 6f. Lithium wall conditioning

One additional technique to control ELMs is via lithium conditioning. In NSTX, sufficient pre-discharge lithium conditioning first reduces ELM frequency and eventually eliminates ELMs altogether<sup>155-157</sup>. In EAST, the use of lithium conditioning is thought to be critical in achievement of long pulse H-mode plasmas<sup>141, 176</sup>, including small ELM or limit-cycle type regimes<sup>177</sup>.

Figure 41 shows the impact of high levels of pre-discharge lithium evaporation onto graphite PFCs on an ELMy H-mode discharge in NSTX<sup>157</sup>. The blue traces are for the reference ELMy discharge, while the red traces are from the lithiated ELM-free H-mode. The gas puffing required to achieve approximately the same density was much higher in the lithiated discharge (panels (b), (d)), while the stored energy was substantially higher at constant NBI power (panels (e), (f)). As typically observed in ELM-free discharges, both the radiated power and  $Z_{\text{eff}}$  climbed during the discharge (panels (g), (h)). Note the elimination of ELMs on the  $D_{\alpha}$  trace, as well as the lower baseline  $D_{\alpha}$  value (panel (c)), indicating substantially reduced recycling.

Substantial progress has been made on understanding the physics behind the ELM suppression. The edge  $T_e$  gradients were relatively unchanged in the last 5% of normalized poloidal flux, while the edge  $n_e$  gradient were substantially reduced<sup>18, 156, 160, 163</sup>. Inside of this region, the  $T_e$  and  $T_i$  gradients both increased. The resulting pressure profiles and gradients were reduced close to the separatrix but increased farther from the separatrix, as shown in Figure 42a,b. The ELMy H-mode equilibria were computed to be unstable to peeling/ballooning modes, whereas the changes in the profiles were stabilizing to peeling/ballooning modes for the lithiated ELM-free H-modes (Figure 42c,d,e). Intermediate lithium evaporation levels reduced ELM frequencies; overall the magnitude of the impact on plasma characteristics increased with increasing pre-discharge lithium<sup>161, 163, 164, 167</sup>. Relative to the stability diagram in Figure 1, this technique is one of the few in which the stable operating window is substantially enlarged, in that core/global limiting instabilities are encountered before ELMs<sup>18</sup>.

Detailed micro-stability analysis revealed that increased drive for Electron Temperature Gradient modes was correlated with the resilience of the far edge  $T_e$  profile, which was a central ingredient of the ELM suppression, while stabilization of Micro-Tearing Modes near the pedestal top was correlated with the global confinement improvement<sup>165</sup>.

While the control over ELMs with lithium conditioning is robust, the line of research is in its infancy and needs to address several issues for serious consideration in future devices. First, a mechanism to provide additional particle transport to prevent impurity accumulation in the ELM-free H-mode must be demonstrated. Second the temperature limit restrictions on lithium as a PFC must be incorporated at a very early stage into future device design. This is partly because lithium evaporation increases exponentially with temperature above about 300 C°, reaching  $\sim 1.5 \times 10^{24}$  atoms/m<sup>2</sup>/sec at 700 C°, and also because of the extreme chemical reactivity of lithium. Modifying the ITER design for lithium usage would be very costly and time consuming, if not impossible. Third the extent to which the ELM elimination requires low recycling regimes needs to be ascertained. Research along these lines has been ongoing with limited resources for several decades<sup>178, 179</sup>, and appears to be accelerating<sup>180</sup> with the increasingly widespread use of lithium in present day confinement devices.

#### 6g. Naturally occurring small ELM regimes

In many ways naturally occurring small ELM regimes represent an elegant solution to the conflicting desires of sufficient ELM impurity exhaust with minimal transient PFC heat and particle loads. The characteristics and physics of small ELM regimes have been described in previous studies<sup>22</sup>. Here the obvious differences in large, medium and small ELM regimes is illustrated. Figure 43 compares<sup>181</sup> the impact of large, Type I ELMs, medium-sized Type III ELMs, small-sized Type V ELMs, and a mixed Type I/V scenario, on divertor  $D_\alpha$  emission and stored energy in NSTX. The Type I ELMs result in stored energy drops of 3-15%, Type III ELMs 1-4%, and Type V ELMs < 1.5%. With sufficient heating power, some small ELM regimes are insufficient to prevent the reappearance of large ELMs; this is illustrated in panel (d), where a giant Type I ELM, with a  $\sim 25\%$  drop in stored energy, appears despite the occurrence of Type V ELMs. We

note that Type II ELMs<sup>182</sup> and grassy ELMs<sup>183</sup> represent two other promising small ELM regimes.

The evaluation of small ELM for applicability in ITER were recently discussed in depth<sup>23</sup>. While there has been additional recent work assessing pedestal stability in EDA H-mode<sup>108</sup>, and comparing Type II ELMs between MAST and ASDEX-Upgrade<sup>184</sup>, and Type II and Type V ELMs in Alcator C-Mod, MAST, and NSTX<sup>185</sup>, the overall conclusions for extrapolability to ITER and future devices remains mixed, as reported recently<sup>23</sup>.

## **7. Summary, Conclusions, and Current Open Questions**

Substantial progress has been made on ELM control techniques over the past decade, and particularly over the last few years as estimates of ITER's acceptable ELM characteristics have been refined. The two leading candidates incorporated into the ITER baseline design are pellet ELM pace-making, to trigger rapid small ELMs, and magnetic perturbations intended to suppress or substantially mitigate ELMs through topological variations.

In the pellet ELM pace-making area, frequent pellets have been shown to pace ELMs and reduce ELM fractional energy loss. The leading need in this area is for a consistent explanation of the impact on the peak heat flux. While DIII-D has shown peak heat flux reduction increasing with pellet frequency, a reduction in peak heat flux has not been realized in JET, because of narrowing of the ELM heat deposition footprint with increasing triggered ELM frequency. Moreover the triggering dynamics and time scales between DIII-D and JET/ASDEX-Upgrade are very different. The extent to which these differences are related to pedestal dynamics tied strongly to the differences in divertor materials (low-Z carbon vs. high-Z tungsten) needs to be ascertained. Resolving these differences appears to be critical in the viability of pellet ELM pace-making as an ELM control tool. On the other hand, the recent use of non-fuel pellets for ELM triggering, namely lithium granules in EAST, is promising in terms of reducing gas loads on

pumping systems and fuel inventory control. Extension of those results to other devices, including confirmation of reduction of the peak heat flux, is needed; installations of similar devices are planned in DIII-D and NSTX-U.

A growing number of devices have demonstrated the ability to affect edge stability and ELM behavior with magnetic perturbations. As such, MP coils have been incorporated into the ITER baseline design. The observations of differing dynamic behavior of pedestal and ELMs in the devices, however, point to the need for a unifying theory to explain the range of results. A central ingredient for such a theory is the role of plasma response to the applied perturbations, particularly under what conditions the applied fields are screened or amplified. Additionally the role of (dimensionless) collisionality and (dimensional) Greenwald fraction needs to be clarified, particularly with respect to the importance of resonant effects. Confidence in the extrapolability for ITER would be increased by the demonstration of MP ELM suppression in discharges with very low rotation, as well minimization of density reduction in the scenarios where significant reduction is observed. Evaluation for future devices with large neutron fluence requires identification of locations where such coils could survive, and assessment of the needed current capability.

Regimes natural devoid of ELMs appear attractive, if extrapolable. In this regard, QH-mode is an increasingly promising possibility as operational windows of QH-mode are enlarged toward ITER-relevant conditions. I-mode may also be usable for some portions of mission fulfillment for future devices like ITER. Although there is less known about the Enhanced Pedestal H-mode, the prospect of a very confinement scenario would be attractive from a design standpoint, if reproducible in other devices. For extrapolation the mechanism by which the naturally occurring MHD in these scenarios drives particle transport needs to be quantified.

The other ELM control techniques discussed in Section 6 may successfully contribute for ITER and future devices in specific operational regimes, but the physics basis for many of these needs to be strengthened for meaningful assessment. SMBI for example, has

demonstrated ELM control in a number of devices, but sufficient penetration of the gas jet inside of the separatrix for future large, high density devices is projected to be very difficult. Heating and current drive for edge control, i.e. ECH/ECCD, LHH/LHCD, have been proven in multiple devices, but power requirements for ELM control in the future appear onerous, and there is still the problem of non-absorbed power depositing on internal components that may not have been designed for high heat loads. Vertical jogs and 3D coils for ELM pace-making have also been shown in multiple devices, but the required in-vessel position control coil current for high current tokamaks are problematic, especially in a neutron environment. Finally lithium wall conditioning has been shown to eliminate ELMs in a single device; applicability on additional devices, and development of techniques to increase particle transport are required before serious consideration as a mainstream ELM control tool; such evidence may come from the recent deployment of lithium in EAST and DIII-D. The various naturally occurring small ELM regimes hold some promise, particularly the ones compatible with lower pedestal collisionality and high divertor recycling.

Overall substantial progress has been made on ELM mitigation techniques. All areas require more thorough fundamental understanding for predictability. There are only a couple of ELM suppression/elimination techniques, and these need to be extended to ITER and reactor relevant conditions, e.g. very low torque input, fueling with pellets, partially detached divertor operation, and compatible with helium exhaust. ELM mitigation techniques need to demonstrate substantially higher enhancement factors over natural ELM frequencies for ITER, and challenges for reactors will be even more substantial, possibly requiring the development of alternative PFCs, e.g. liquid metals. Naturally occurring ELM-suppressed regimes hold good promise for the future, provided their access and operating windows can be substantially widened.

### **Acknowledgements**

The author acknowledges discussions with K. Burrell, R. Buttery, T. Evans, S. Gerhardt, A. Garofalo, B. Grierson, R. Hawryluk, A. Hubbard, J. Hughes, Y.M. Jeon, A. Kirk, A. Loarte, Y.F. Liang, D. Orlov, T. Osborne, C. Skinner, W. Solomon, and W. Suttrop. The

referees are also thanked, as their comments resulted in substantial improvements. This work was supported by the U.S. Dept. of Energy under contract DE-AC02-09CH11466.

## Figure Captions

1. (a) Schematic of H-mode edge pressure and current profiles, with the H-mode pedestal region shaded in dark green. The lighter shading represents the width of the calculated unstable peeling-ballooning mode, driven both by pressure gradient and current<sup>35</sup>. Y-axis units are arbitrary. (b) Representation of edge stability space in edge pressure gradient and current space, color-coded by the most unstable toroidal mode number.
2. (a) Diagram of edge pedestal stability in pressure gradient and edge current space, with different possible ELM cycles indicated in parenthesis. (b) Representation of a possible relaxation cycle for mixed (small and large) ELM regimes<sup>27</sup>.
3. Illustration of EPED pedestal model, with constraints imposed by peeling-ballooning modes (solid) and kinetic ballooning modes (dashed). The EPED model prediction is given by the intersection of the two curves, in good agreement with the measured data<sup>34</sup>.
4. Projected boundary between acceptable and unacceptable ELMs for ITER, as a function of the ELM wetted area<sup>25</sup>. See text for details of the calculation.
5. (a) Comparison of projected uncontrolled ELM frequency for ITER as a function of plasma current (black squares), with that required for controlled ELMs (red circles) and that required to maintain acceptable tungsten influx (blue triangles)<sup>25</sup>. (b) Required ratio of the maximum of either the mitigated ELM frequency or the frequency needed to prevent W accumulation, divided by natural ELM frequency for acceptable ELMs in ITER<sup>78</sup>.
6. Schematic of sequence leading to ELM triggering with pellets: (a) Excess density builds up on rational surfaces, due to enhanced pellet ablation; this equilibrates along flux surfaces at the ion acoustic speed (time scale  $\sim$  msec); (b) the local temperature drop associated with the excess density equilibrates on an electron conduction time scale ( $\sim$   $\mu$ sec); (c) a localized high pressure forms due to the mismatch of particle and energy equilibration time scales; (d) a strong 3-D pressure gradient develops, leading to destabilization of ballooning modes<sup>51, 186</sup>.

7. Comparison of evolution of two discharges with 60 Hz pellet induced ELMs (red) with natural 4-5 Hz ELMs (black) in DIII-D<sup>52</sup>.
8. Dependence of (a) ELM deposited energy, and (b) peak heat flux at the inner and outer divertor targets as a function of pellet frequency in DIII-D<sup>54</sup>.
9. Evolution of discharge with ELM pace-making in JET with the ITER-like wall; the top panel displays an expanded time range of the subsequent panels<sup>53</sup>.
10. Comparison of (a) ELM frequency, (b) ELM energy deposition, (c) peak divertor heat flux, (d) ELM energy flux density, and (e) ELM size relative to initial pedestal stored energy for a discharge with pellets (left column) and with natural ELMs only (right column) in JET<sup>53</sup>. The red datapoints represent average values.
11. Demonstration of ELM pace-making with lithium granules on EAST<sup>56</sup>: (a) Schematic of lithium granule injector implemented; (b) divertor  $D_{\alpha}$ , (c) visible Bremsstrahlung, and (d) extreme ultra-violet emission from the edge plasma. Red vertical lines denote triggered ELMs, while vertical blue lines reflect natural ELMs. The horizontal green lines in panel (d) represent time of flight of lithium granules from the injector to the plasma edge.
12. Non-linear MHD modeling with JOREK of pellet-induced ELM in DIII-D<sup>57</sup>: modeled pellet density (colors) and flow contours after (a) a small 1 mm pellet that does not trigger a ballooning mode, and (b) a 2.1mm pellet that triggers a ballooning mode. Panel (c) shows the analysis of a variation of the pellet speed, and its effect on the pellet deposition profile and resulting local pressure perturbation. The perturbation to the density and computed flow patterns with JOREK are shown to qualitatively distinguish the small 3-D pellet perturbation from a large one, the latter due in part to the destabilized ELM.
13. (a) Schematic of ITER pellet design layout<sup>58</sup>, including low-field side pellets for ELM pacing near the X-point, and (b) Non-linear MHD calculation with JOREK showing impact of pellets size on local pressure perturbation<sup>57</sup>. Ballooning modes were triggered for the 3.7mm and 4.7mm pellets.
14. Comparison of (a) Pedestal electron density and (b) electron temperature response with two different RMP amplitudes (red, green) with reference (black) in DIII-D.

- Panel (c) shows that the RMP reduced the edge pressure gradient and current, moving the operational point from unstable (red) to stable (blue)<sup>17</sup>.
15. Demonstration of ELM suppression with RMP in DIII-D, and its sensitivity to amplitude of the radial component of the applied resonant magnetic perturbation at the 11/3 surface normalized to the on-axis vacuum toroidal field ( $\delta b_r^{11/3}/B_t$ )<sup>59</sup>: (a) reference, (b)  $3.0 \times 10^{-4}$ , (c)  $3.7 \times 10^{-4}$ , (d)  $4.0 \times 10^{-4}$ , (e)  $4.4 \times 10^{-4}$ , (f)  $4.9 \times 10^{-4}$ . The pedestal density response is shown in (g). The RMP initiation time is indicated by the vertical green line.
  16. Illustration of how RMPs could suppress ELMs in DIII-D<sup>83</sup>: (a) EPED model calculation, representing natural ELM crash when the peeling/ballooning limit is exceeded; (b) vertical shaded zones indicating where an island could open up under proper conditions; (c) prediction of width of resonant windows in  $q_{95}$  (light shade) with observed ELM suppression windows (dark shade), when island would open up near the top of the pedestal and induce extra particle transport. Also shown are (d)  $q_{95}$ , (e)  $I_p$ , (f) RMP coil current, and (g) pedestal  $n_e$ .
  17. Evolution of discharge parameters with ELM suppression from n=1 magnetic perturbations (red), and for a reference discharge (black) in KSTAR<sup>72</sup>: (a) plasma current, and current in the magnetic perturbation coils above (“Top-FEC”), at (“Mid-FEC”), and below (“Bot-FEC”) the midplane; (b) divertor  $D_\alpha$  emission; (c) midplane  $D_\alpha$  emission; (d) line-average density; (e) plasma total stored energy, and (f) core toroidal rotation speed.
  18. Evolution of discharge parameters with ELM suppression from n=1 magnetic perturbations in KSTAR<sup>72</sup>: (a)  $D_\alpha$  emission, (b) edge  $T_e$  at  $\rho \sim 0.94$  with nominal and expanded time ranges, (c) 2-D ECE imaging during ‘ELM intensified’ phase (left panel), and during ELM suppressed phase (right panel).
  19. (a) Magnetic perturbation ramps to determine the threshold perturbation for ELM mitigation in ASDEX-Upgrade<sup>20</sup>. The left hand side panels are for odd parity, and the right hand side panels for even parity. (b) Poloidal mode number spectrum for n=2 magnetic perturbation, at the q=5 surface.

20. Operational space of edge electron pressure gradient and pedestal electron temperature for small ELM regimes in ASDEX-Upgrade<sup>69</sup>. Application of magnetic perturbations opened up a new regime with high edge  $T_e$  (indicated by red-dashed ellipse) but below the stability limit encountered for Type I ELMs.
21. Evolution of discharge parameters during ELM mitigation with applied  $n=2$  magnetic perturbation in JET<sup>67</sup>: (a) current in error field correction coils, (b) central  $T_e$ , (c) central  $n_e$ , (d) total radiated power, and (e) divertor  $D_\alpha$  emission. Panels (f) and (g) compare evolution of pedestal  $T_e$  with and without applied magnetic perturbation. Panel (h) shows a probability distribution function of ELM size without (red) and with MP mitigation (blue).
22. Comparison of ELM mitigation with different plasma boundary shapes and toroidal mode numbers in MAST<sup>77</sup>: (a) boundary shapes for connected double-null (CDN) and lower single-null diverted (LSND) configurations; (b) current in perturbation coils; (c) comparison of line-average density with (blue) and without (black) coils;  $D_\alpha$  emission without coils (d) and with coils (e); panels (f)-(i) correspond to reference and with-coil discharges for CDN shape. Panel (j) shows comparison of computed edge stability in edge current density and normalized pressure gradient ( $\alpha$ ) space with measured profiles for LSND configuration, and panel (k) the corresponding stability evaluation for CDN configuration.
23. Comparisons between data and calculations with the linear, two-fluid resistive MHD M3Dc1 code, using a phase flip of the applied  $n=3$  coil current in DIII-D<sup>84</sup>: (a) data from soft X-ray emission, (b) simulation with M3Dc1. (c) Computed modification of the edge  $T_e$  profile with M3Dc1, compared with Thomson scattering data during phase flip experiments.
24. Time evolution of discharge parameters with an “Improved” or I-mode phase from Alcator C-Mod<sup>104</sup>. The I-mode phase is shaded, and accompanied by an increase in magnetic fluctuations. An ELM-free H-mode phase follows at  $t \sim 1.2$  sec.
25. (a)-(d): comparison of fitted kinetic profiles during I-mode and ELMy H-mode in Alcator C-Mod<sup>108</sup>. Panel (e) represents the computed edge stability boundary with

the I-mode profiles from panels (a)-(d), showing that the I-mode profiles are stable to kink/peeling and ballooning modes.

26. (a) Fluctuation amplitude as a function of frequency during L-mode, I-mode, and H-mode from reflectometer measurements on Alcator C-Mod<sup>106</sup>; (b) correlation between weakly coherent mode (WCM) amplitude and particle flux through the last closed flux surface, via a heating power scan and midplane  $D_\alpha$  analysis for the particle flux<sup>146</sup>; and (c) operational space of I-mode in C-Mod, with the arrows indicating a single discharge trajectory with fueling to increase density in I-mode<sup>121</sup>.  $P_{\text{loss}}$  is the total power crossing the separatrix, i.e. heating power-core radiation- rate of change of plasma stored energy ( $dW/dt$ ).
27. Evolution of discharge parameters<sup>114</sup>, edge fluctuations<sup>110</sup>, and edge stability analysis<sup>82</sup> for quiescent H-mode (QH) discharges at DIII-D: (a) Plasma current and  $D_\alpha$  emission, (b) amplitude of the Edge Harmonic Oscillation (EHO) for  $n=2$  and  $n=3$ , (c) line average density, (d) neutral beam heating power and total radiated power, and (e) neutral beam torque. Panel (f) shows the evolution<sup>15</sup> of the EHO with prominent oscillations for  $n=1$ ,  $n=2$ ,  $n=3$ , and  $n=4$ , while the inset shows the radial structure of the  $n=2$  mode amplitude from beam emission spectroscopy. Panel (g) shows that the edge is stable to ballooning modes, but near the kink/peeling stability boundary for QH-modes.
28. Evolution of QH-mode discharge with dynamic torque scan and applied 3-D magnetic perturbations in DIII-D<sup>112</sup>: (a) normalized  $\beta$ ,  $n=3$  current from the internal (I-coil) and external (C-coil) coils; (b)  $D_\alpha$  emission; neutral beam torque; and (d) confinement quality as indicated by H-factor normalized to ITER89-P scaling. Panel (e) compares the toroidal rotation profiles with substantially negative and zero torque. Panel (f) compares the edge rotational radial shear in QH-mode and ELMy H-mode, normalized to the Alfvén frequency ( $\omega_A$ ).
29. Evolution of QH-mode discharge in DIII-D with positive neutral beam torque<sup>114</sup>, close to the equivalent design value of ITER: (a)  $D_\alpha$  emission, (b) normalized  $\beta$  and

- energy confinement relative to ITERH98-pby2 scaling, line-average and pedestal  $n_e$ , (d) toroidal rotation speed at the pedestal top, and (e) neutral beam torque.
30. Time evolution of an Enhanced Pedestal (EP) H-mode discharge in NSTX<sup>116</sup>: (a) plasma current and neutral beam injected power ( $P_{\text{NBI}}$ ), (b) line-average density from Thomson Scattering, (c) plasma stored energy from equilibrium reconstruction, (d) thermal energy confinement time, (e) thermal energy confinement time relative to ITERH98-pby2 scaling, and (f) divertor  $D_\alpha$  emission. The transition from H-mode to EP H-mode is indicated by the vertical arrow.
  31. Profile comparisons for H-mode and EP H-mode from NSTX<sup>116</sup>: panels (a)-(d). Panel (e) shows the correlation between the edge toroidal rotation shear and the achieved pedestal ion temperature during EP H-modes. The different symbols are from different discharges.
  32. Time evolution of discharge parameters with Supersonic Molecular Beam Injection (SMBI) used for ELM mitigation in HL-2A<sup>137</sup>: (a) control voltage to SMBI valve, (b)  $D_\alpha$  emission, (c) average time between ELMs, (d) ELM amplitude, (e) energy confinement time, and (f) line-average electron density.
  33. Response of heat flux and edge density profile to SMBI pulse in HL-2A<sup>169</sup>: (a)  $D_\alpha$  emission, (b) peak divertor heat flux  $Q_{\text{div}}$  [ $\text{MW}/\text{m}^2$ ] inferred from Langmuir probes, with overlaid SMBI control voltage in white, (c)  $D_\alpha$  emission with overlaid SMBI control voltage for a different discharge, and (d)  $n_e$  profiles at four different times indicated in panel (c).
  34. Use of edge Electron Cyclotron Resonance Heating (ECRH) to alter ELM stability in TCV<sup>139</sup>: (a) ECH launch angle and location of maximum deposition, (b) absorbed power for second harmonic  $P_{\text{abs},X2}$ , (c)  $H_\alpha$ , (d) ELM frequency, (e) ELM size, (h) energy confinement time, (g) H98 confinement factor, and line-average density.
  35. Use of Lower Hybrid Waves (LHW) to affect ELM activity in EAST<sup>140</sup>: (a) power input from Ion Cyclotron Resonance Heating ( $P_{\text{ICRH}}$ ), (b) power input from LHW ( $P_{\text{LHW}}$ ), (c) line-average electron density, (d) plasma stored energy, (e) peak particle flux, and (f) divertor  $D_\alpha$  emission.

36. Sensitivity of effect of Lower Hybrid Current Drive (LHCD) on ELM stability to edge safety factor  $q_{95}$  in EAST<sup>141</sup>: peak ion particle flux for three different  $q_{95}$  values. The phases with substantial LHCD are indicated by the yellow shaded regions.
37. Use of vertical placement displacements (“kicks” or “jogs”) to increase ELM frequency in TCV<sup>142</sup>. The left hand side panels represent a perturbation current below the level needed to affect ELMs, while the right hand side panels represent a 4x higher perturbation amplitude: (a)  $D_{\alpha}$ , (b) current in the perturbation coils  $I_g$ , (c) time between ELMs  $\Delta t_{ELM}$ , and (d) the delay from the time of the applied perturbation to the ELM trigger time. A direct effect on the  $\Delta t_{ELM}$  can be seen on the right hand column in panel (c). The clustering of data to the 2-2.5 msec range in the right hand side panel (d) indicates a substantial correlation with high amplitude perturbations.
38. (a) Dependence of ELM size (normalized to pedestal stored energy) on ELM frequency in JET, and (b) dependence of energy confinement time relative to ITERH98-pby2 scaling on ratio of pedestal electron density to the Greenwald density limit in JET<sup>144</sup>.
39. Demonstration of ELM pace-making with magnetic perturbations in NSTX<sup>152</sup>: (a) stored energy from equilibrium reconstruction, (b) line-average electron density, (c) total radiated power, (d)  $D_{\alpha}$  emission from reference ELM-free discharge, (e)  $D_{\alpha}$  emission and n=3 magnetic perturbation current from discharge with 10 Hz triggered ELMs, and (f) same quantities from discharge with 30 Hz triggered ELMs.
40. ELM pace-making with magnetic perturbations in DIII-D<sup>154</sup>: (a) ratio of peak heat flux during paced ELMs relative to natural ELMs; (b) pacing efficiency  $f_l$  defined as ratio of observed to expected ELMs at a given frequency; and (c) product of (a) and (b), showing relationship between natural ELM frequency  $f_0 \sim 40$  Hz and  $f_l$ .
41. Comparison of discharge evolution in ELMy H-mode (blue) with lithium-induced ELM-free H-mode (red) in NSTX<sup>157</sup>: (a) plasma current and neutral beam heating power, (b) integral of gas fueling, (c) divertor  $D_{\alpha}$  emission, (d) line-average electron density, (e) stored energy in electron channel, (f) total stored energy from

equilibrium reconstruction, (g) radiated power, and (h) volume-average effective charge,  $Z_{\text{eff}}$ .

42. Comparison of ELMy H-mode and lithium-induced ELM-free H-mode in NSTX<sup>18</sup>: (a) total pressure and (b) radial pressure gradient in ELMy (black) and ELM-free (red) H-modes; (c) computed displacement with the PEST code for the ELMy H-mode; edge stability diagrams for (d) ELMy and (e) ELM-free equilibria.
43. Illustration of characteristic of different ELM types, from the NSTX<sup>181</sup>:  $D_{\alpha}$  (left column) and stored energy  $W_{\text{MHD}}$  for (a) large, Type I ELMs, (b) medium, Type III ELMs, (c) small, Type V ELMs, and (d) mixed, Type I and Type V ELMs.

Figure 1

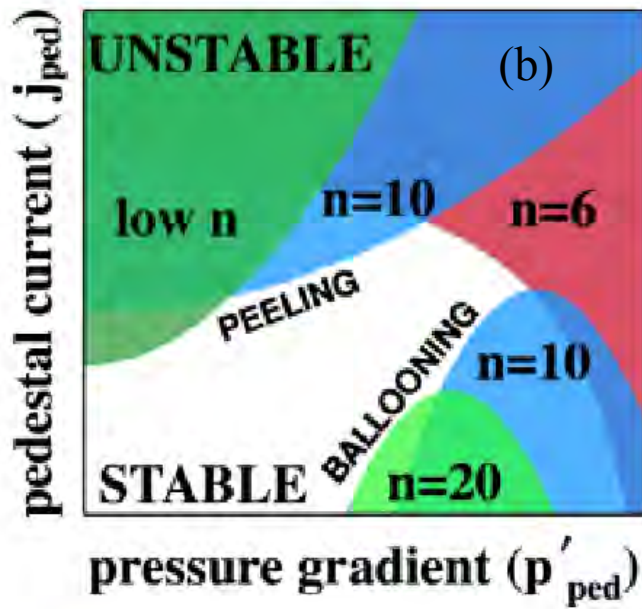
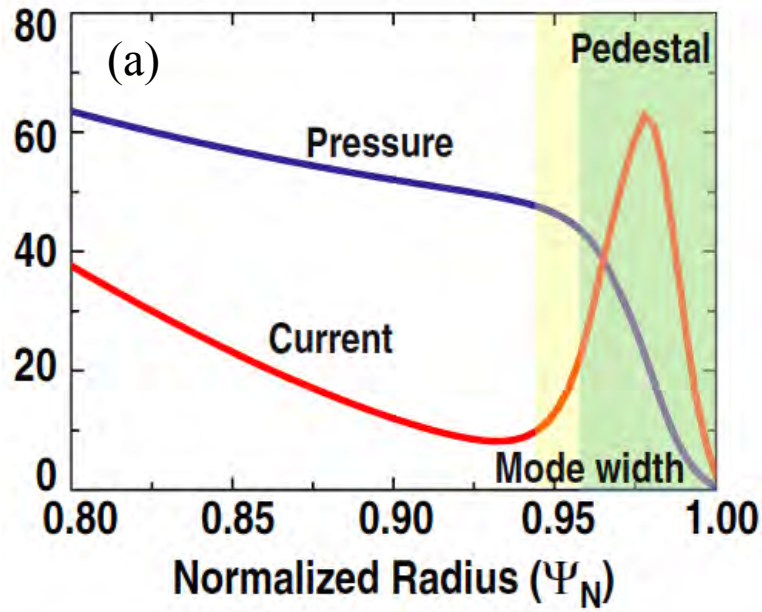


Figure 2

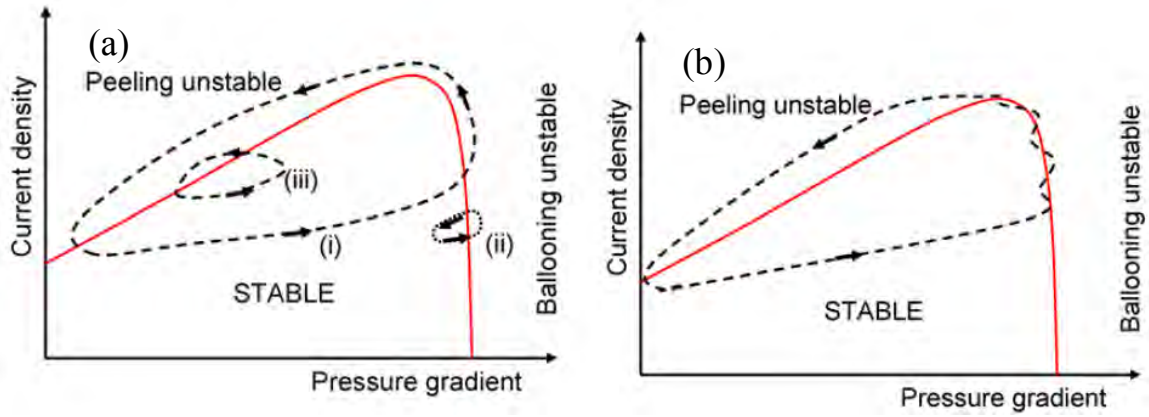


Figure 3

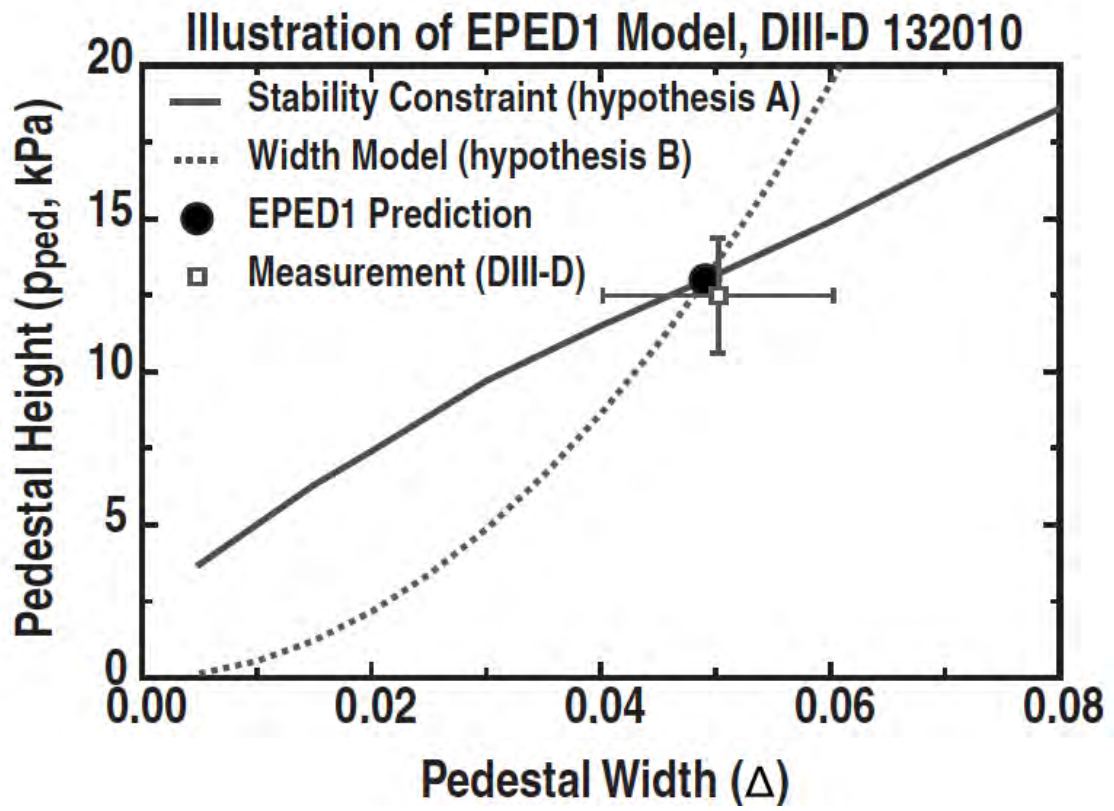


Figure 4

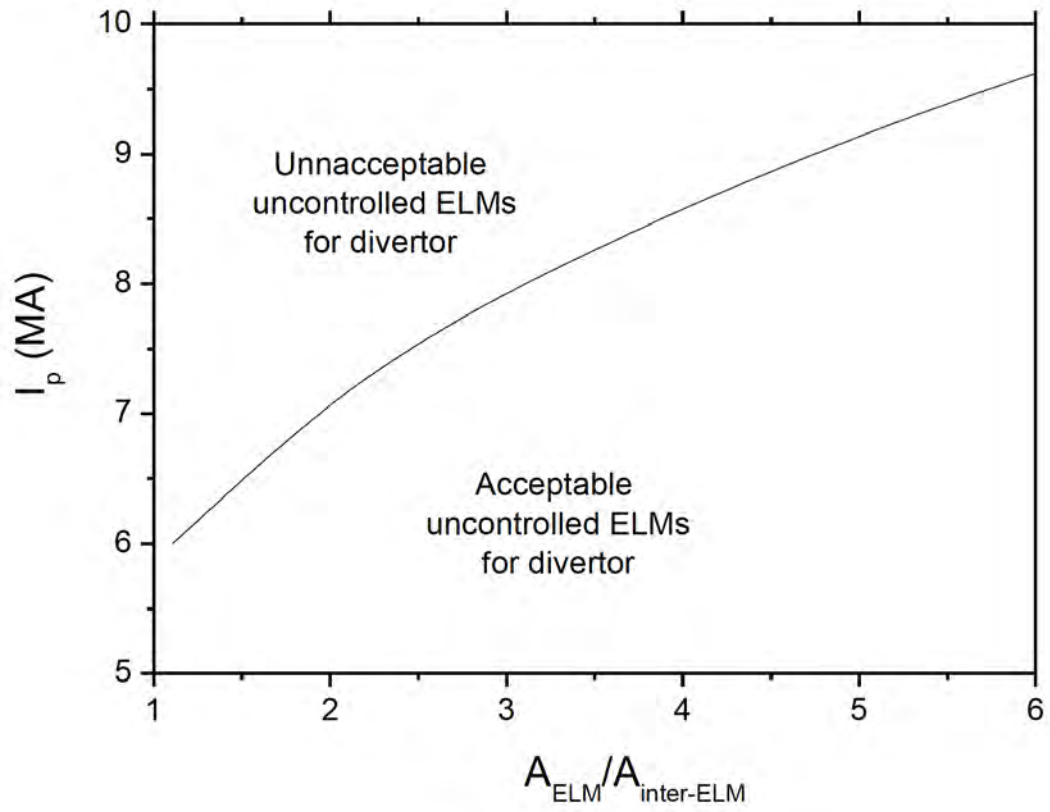


Figure 5

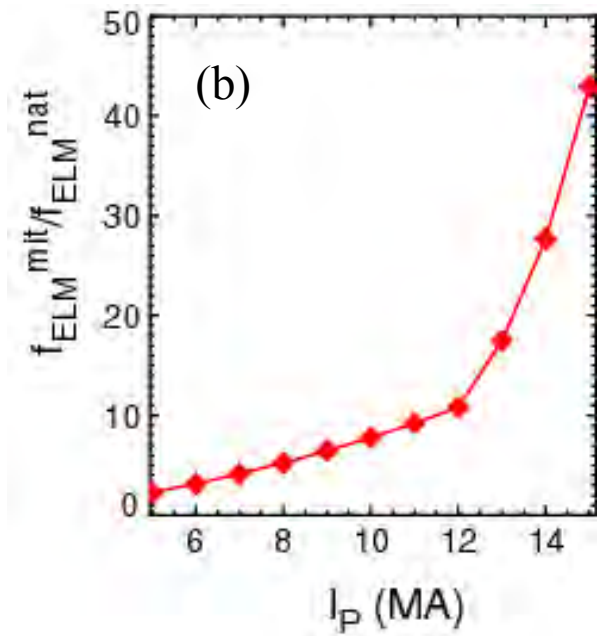
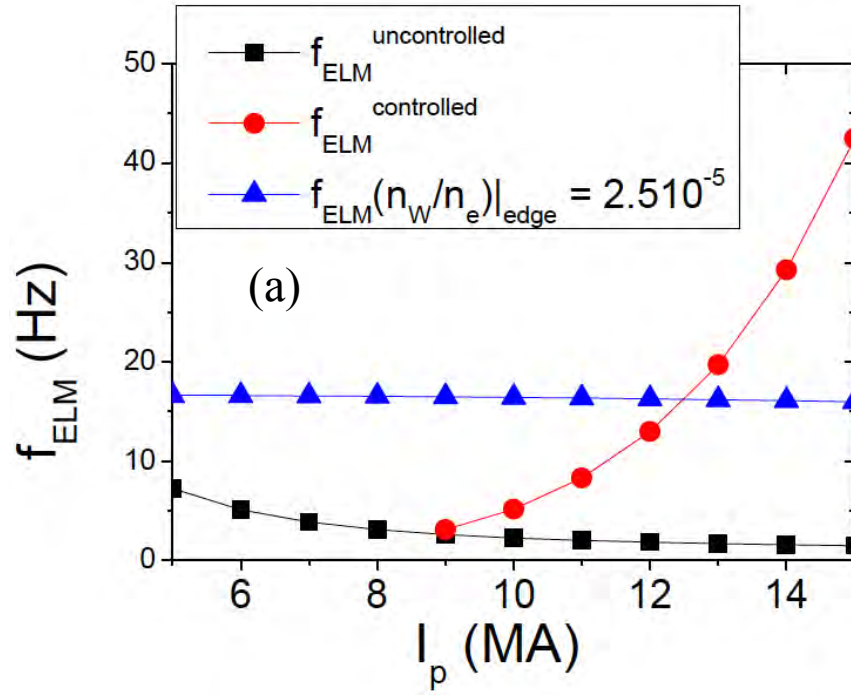


Figure 6

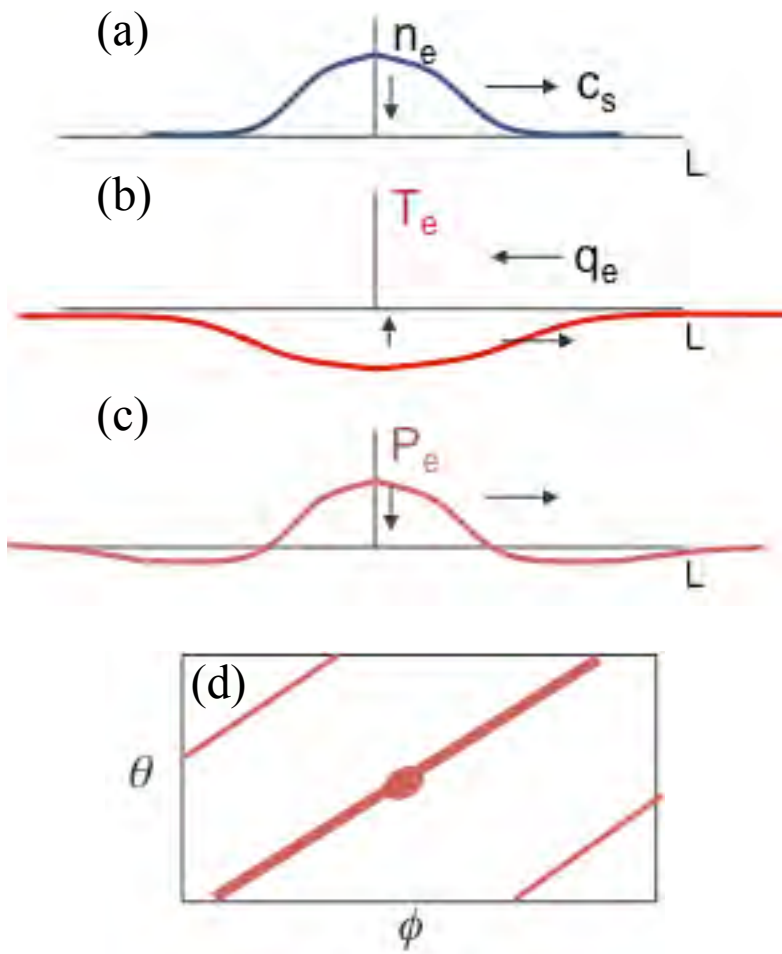


Figure 7

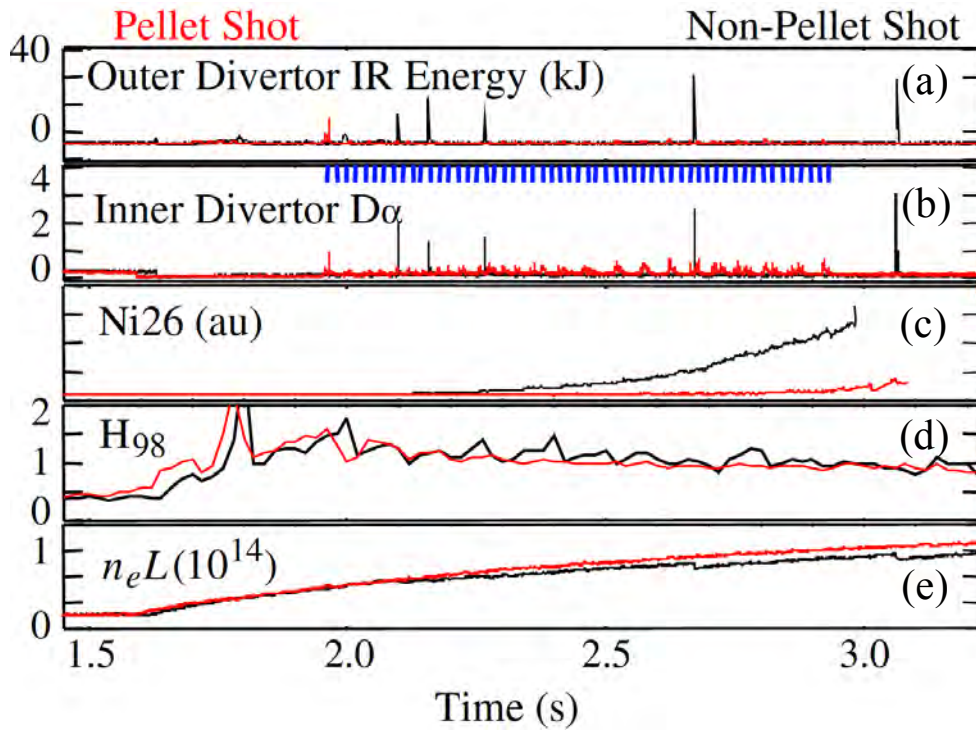


Figure 8

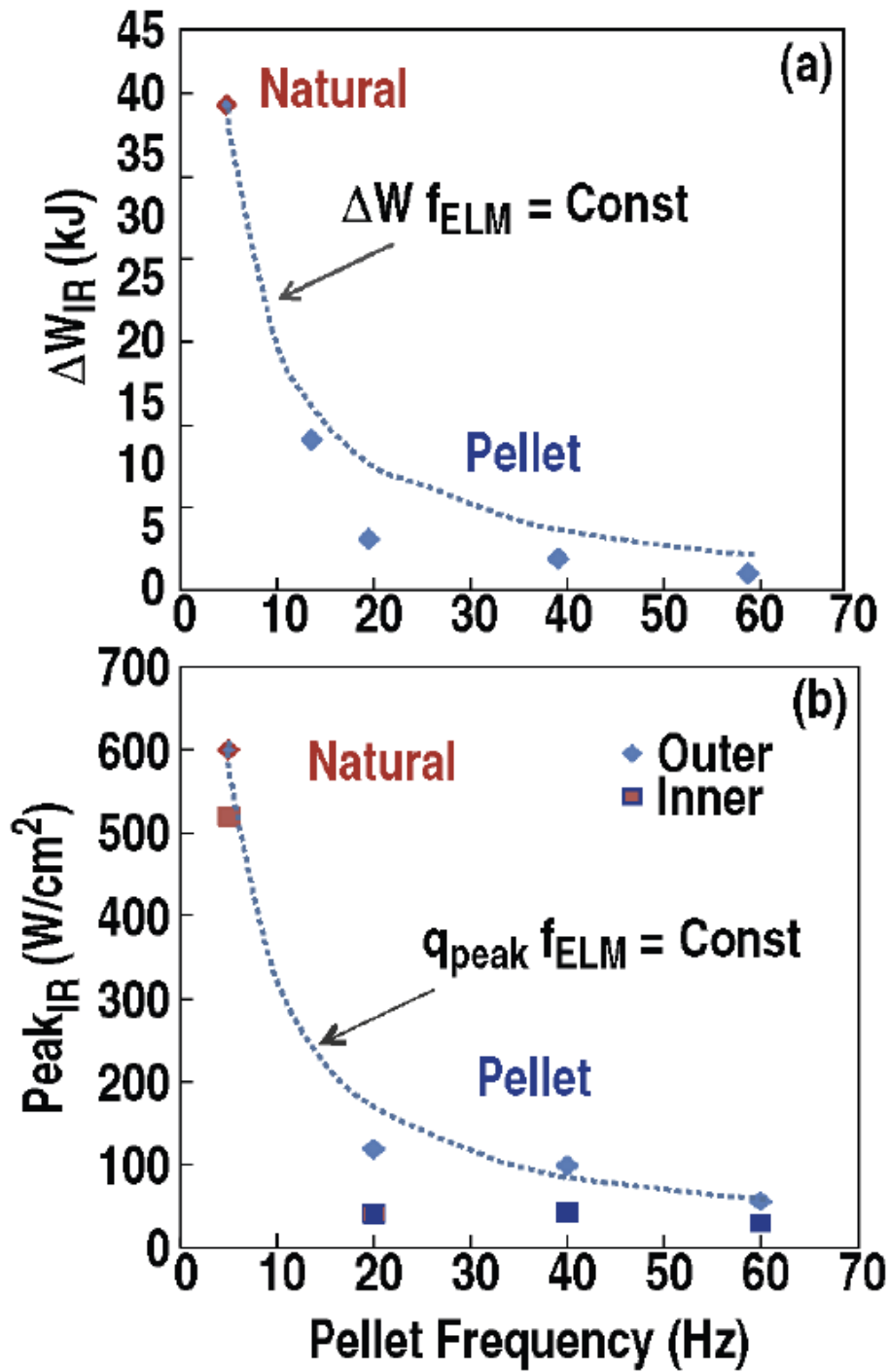


Figure 9

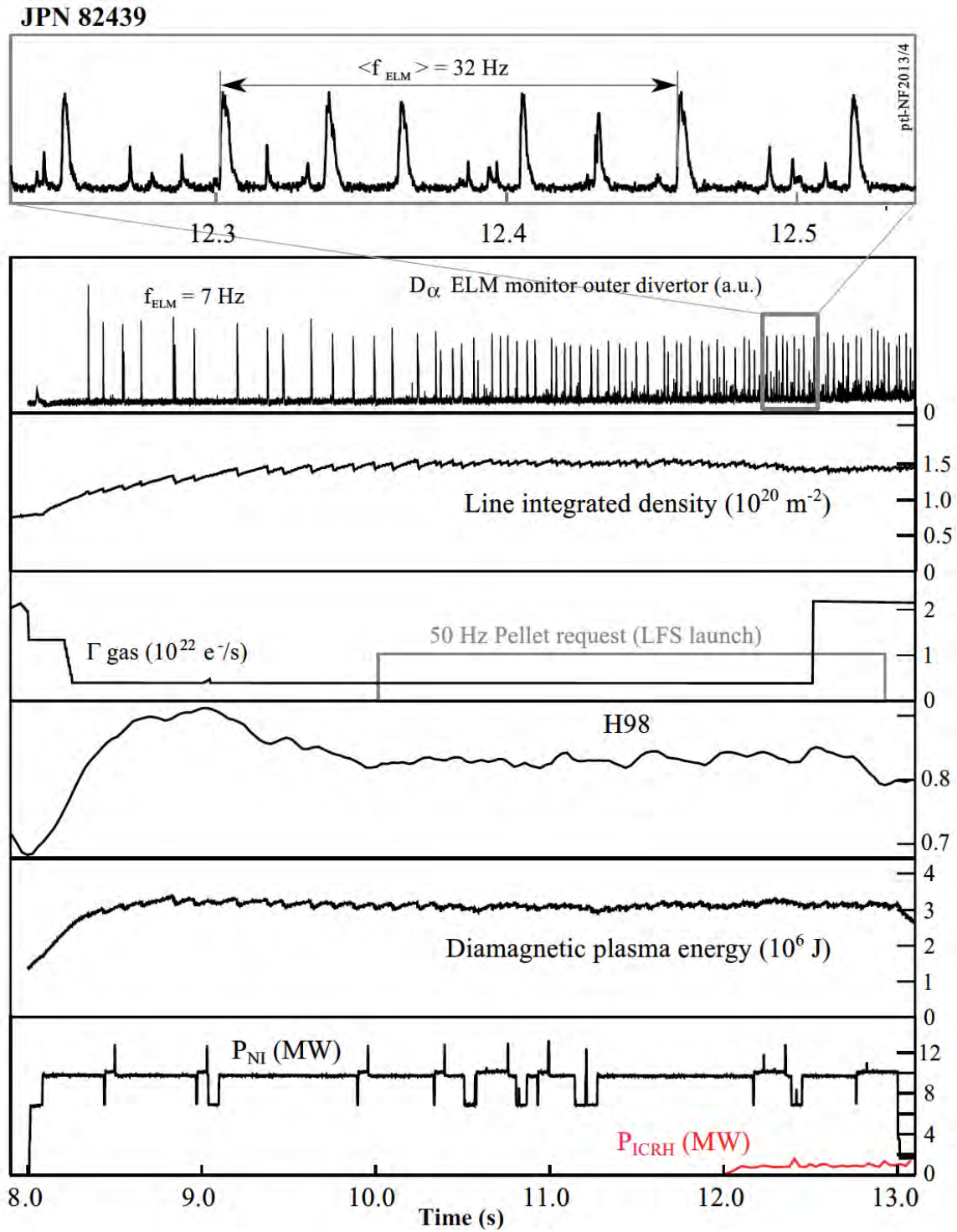


Figure 10

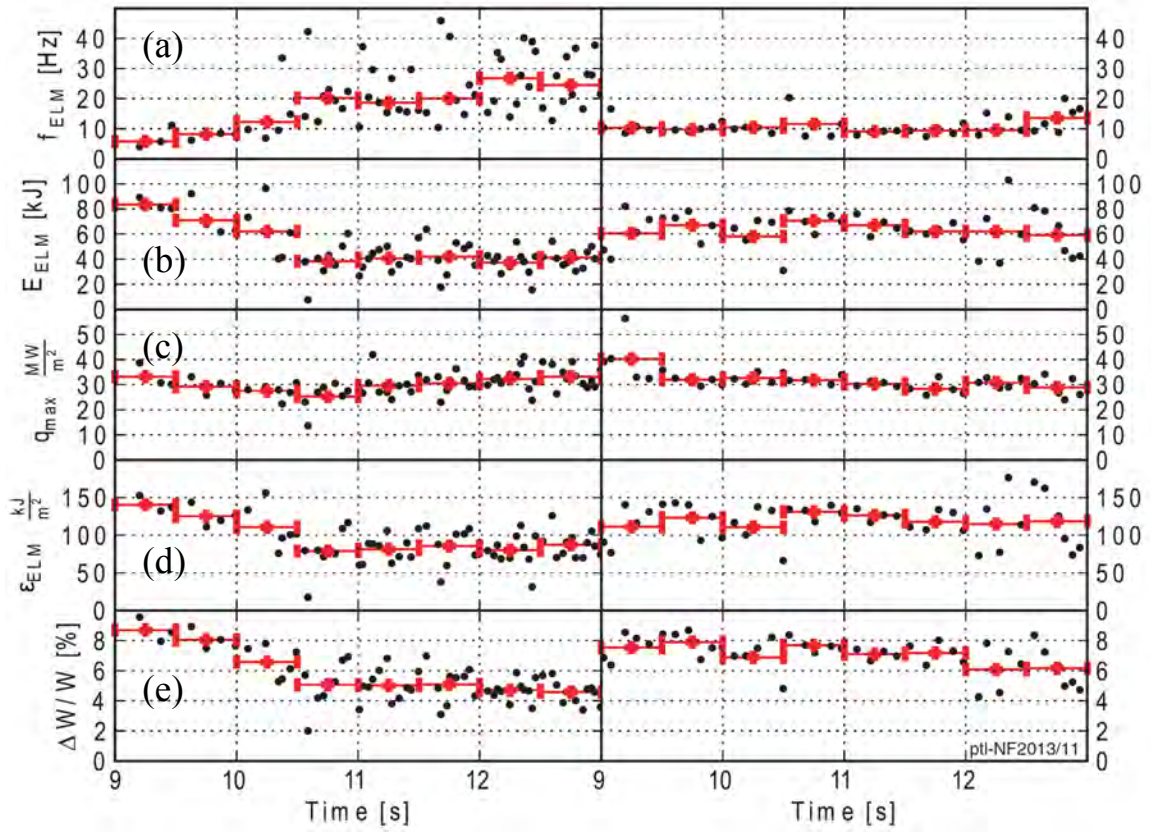


Figure 11

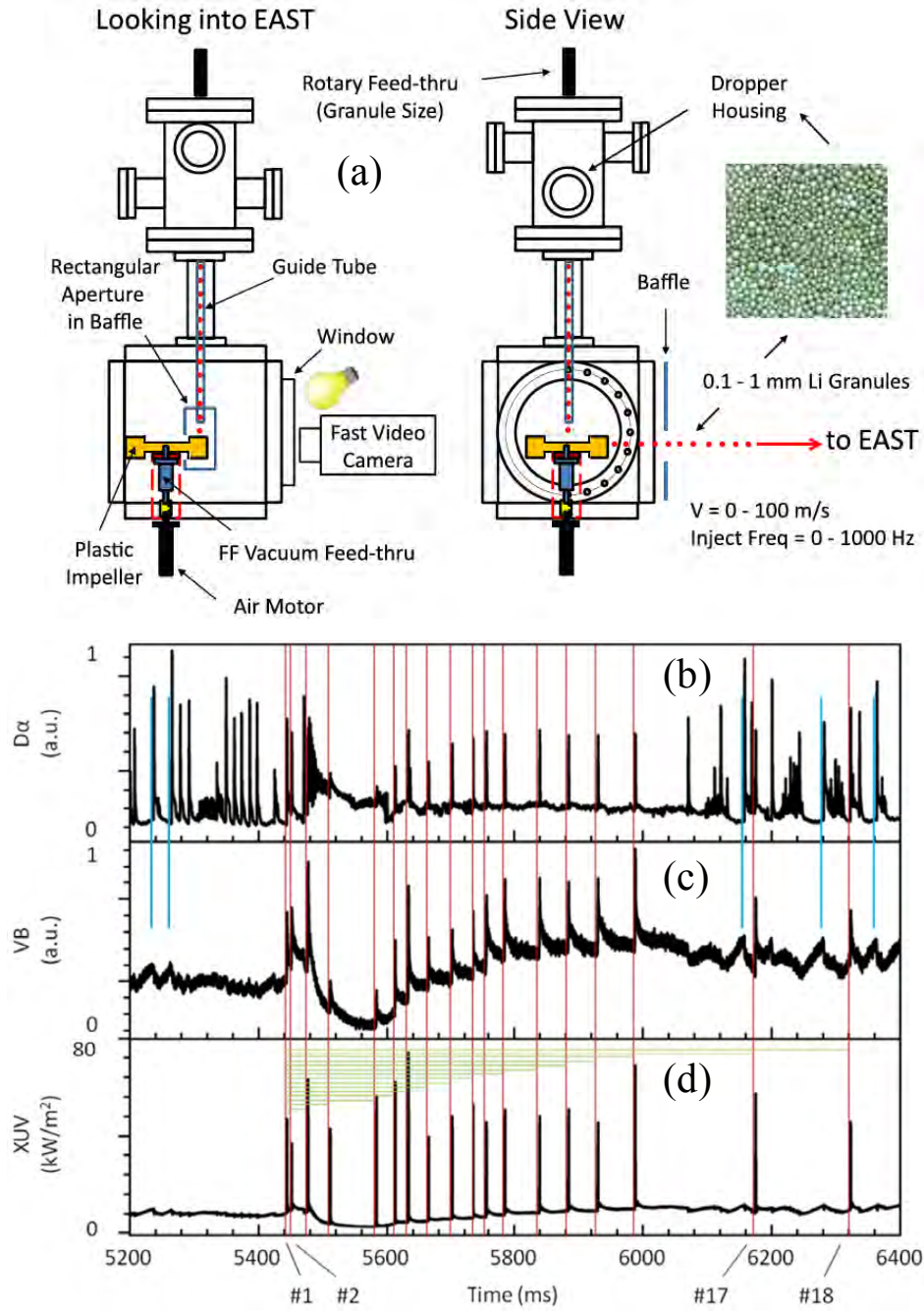


Figure 12

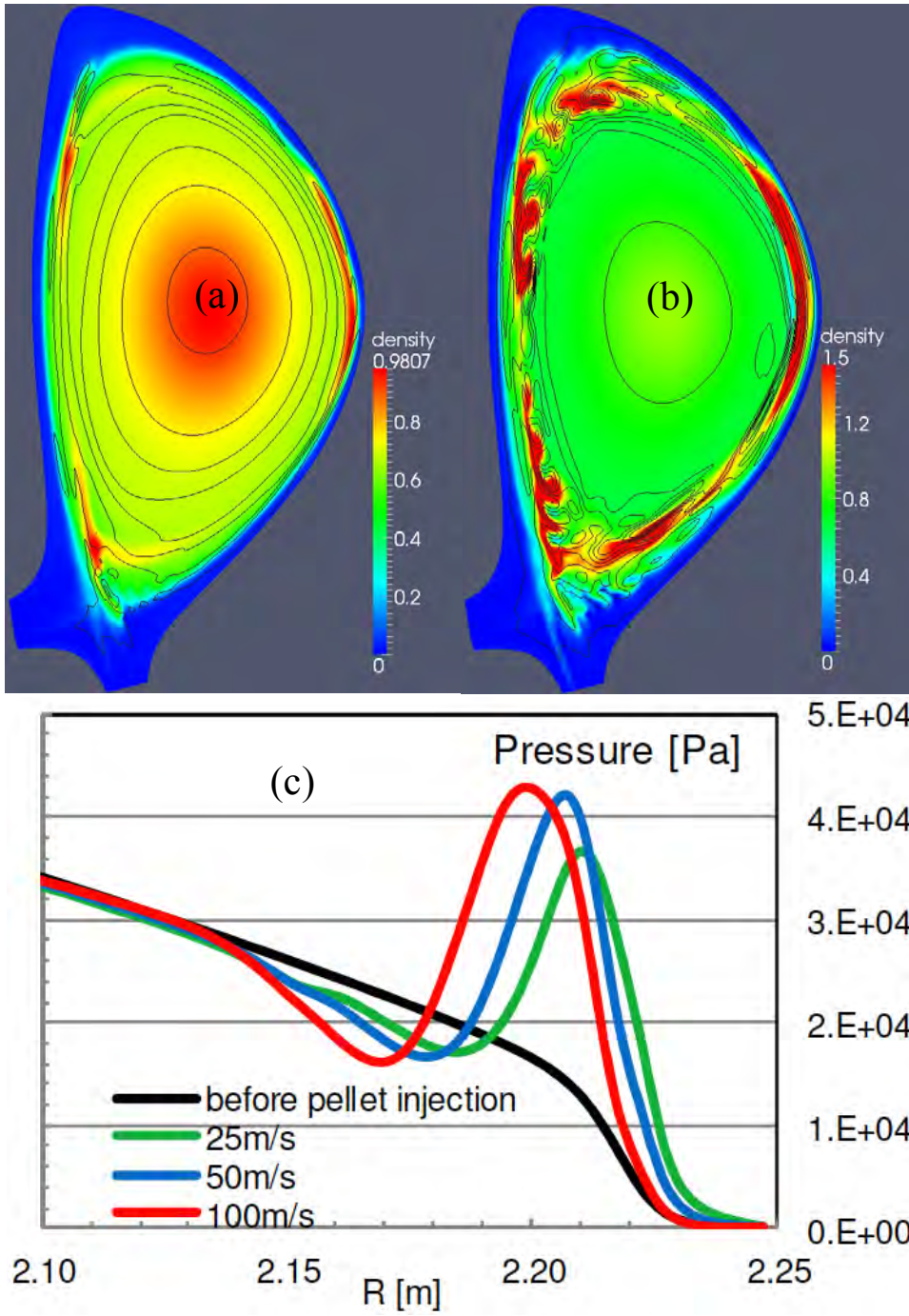


Figure 13

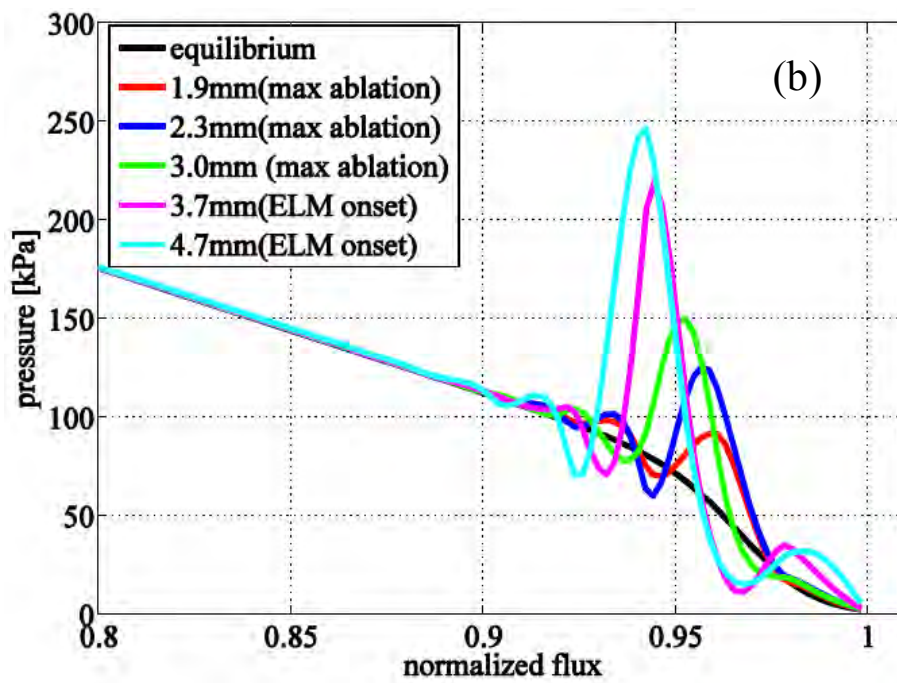
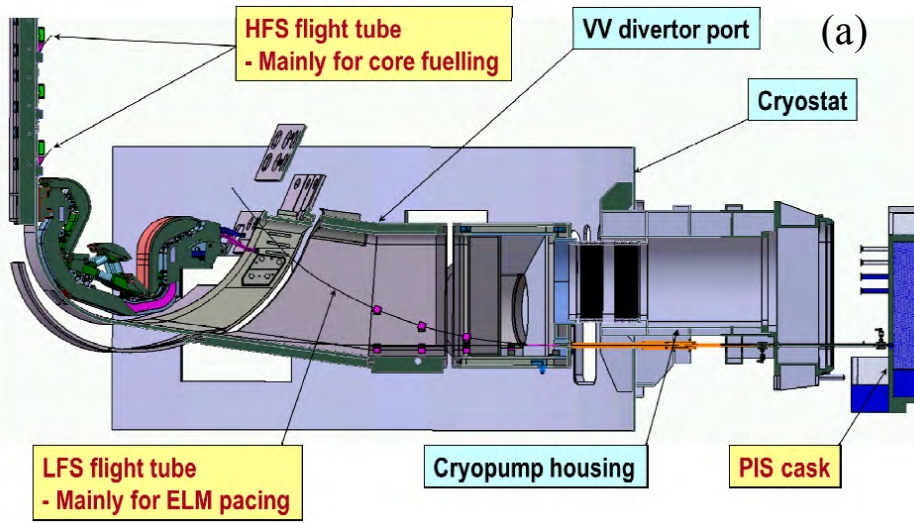


Figure 14

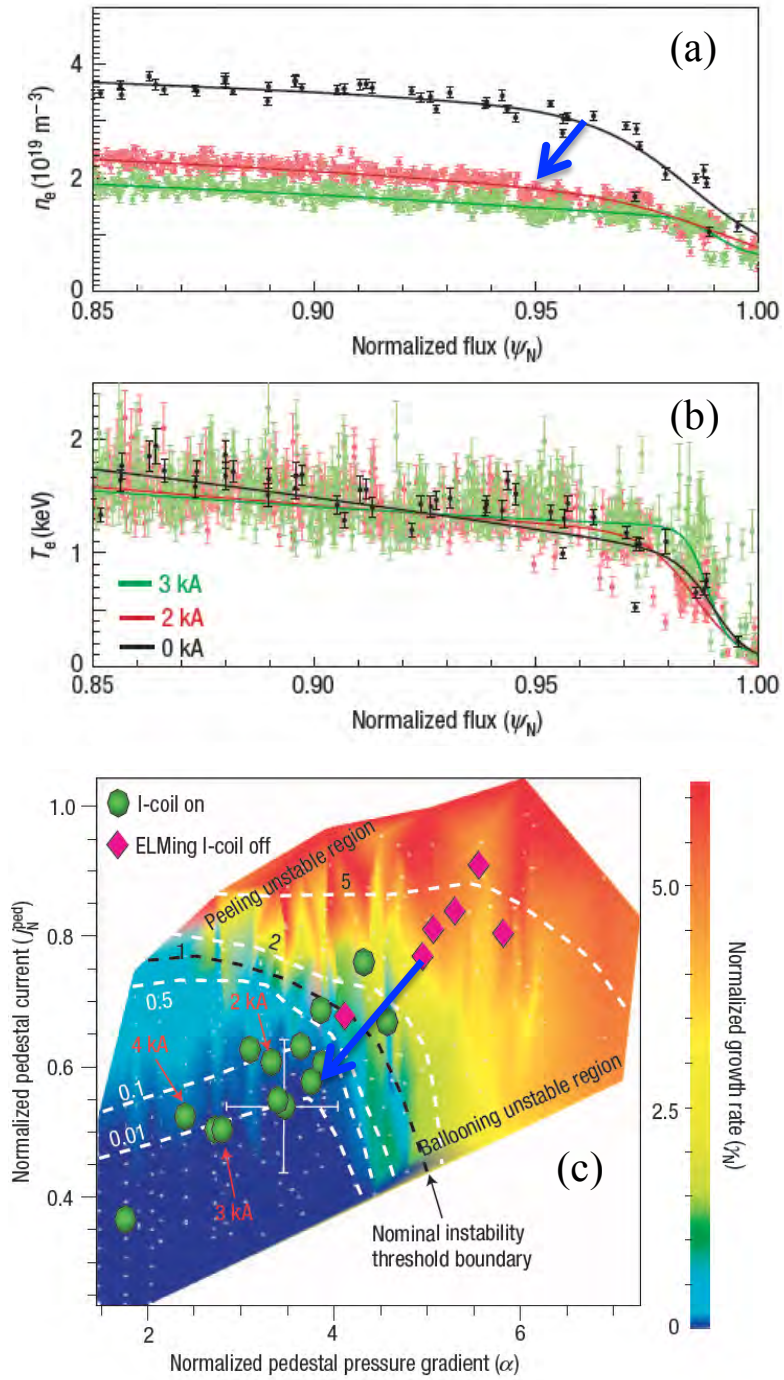


Figure 15

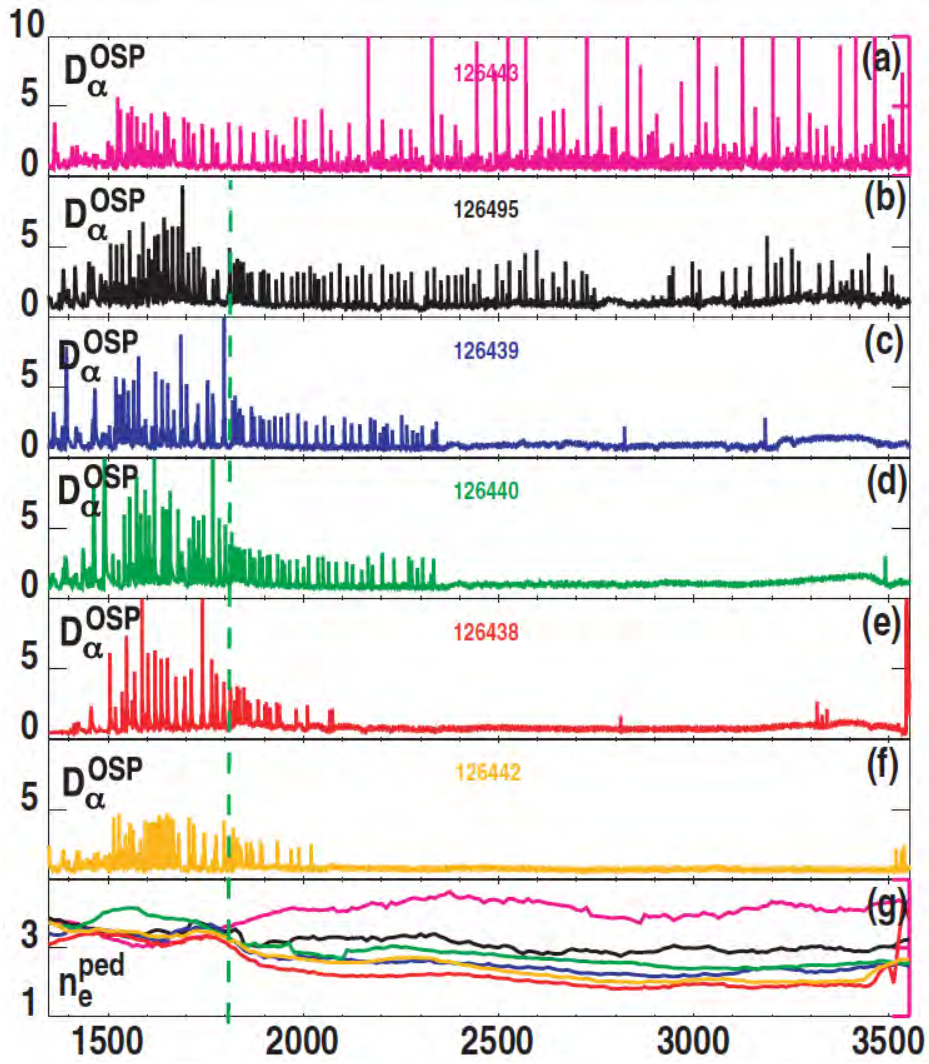


Figure 16

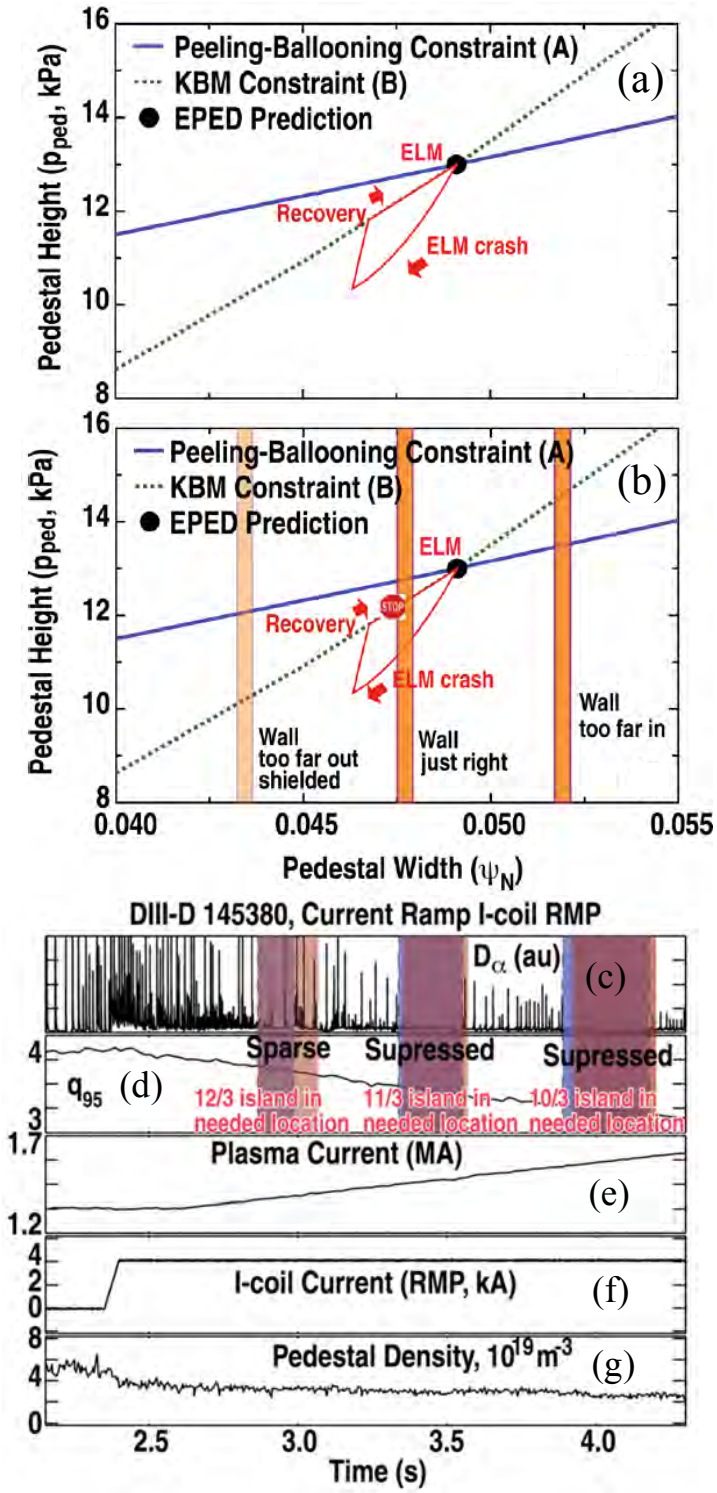


Figure 17

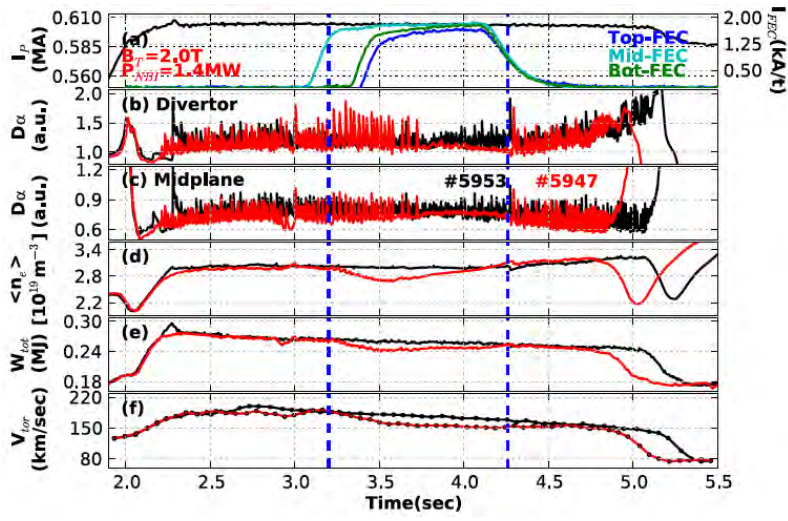


Figure 18

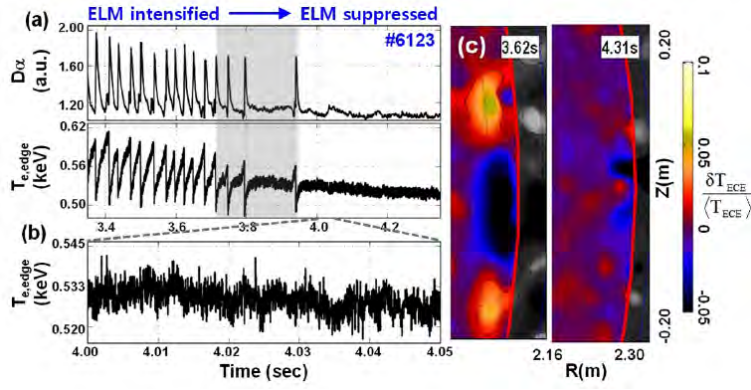


Figure 19

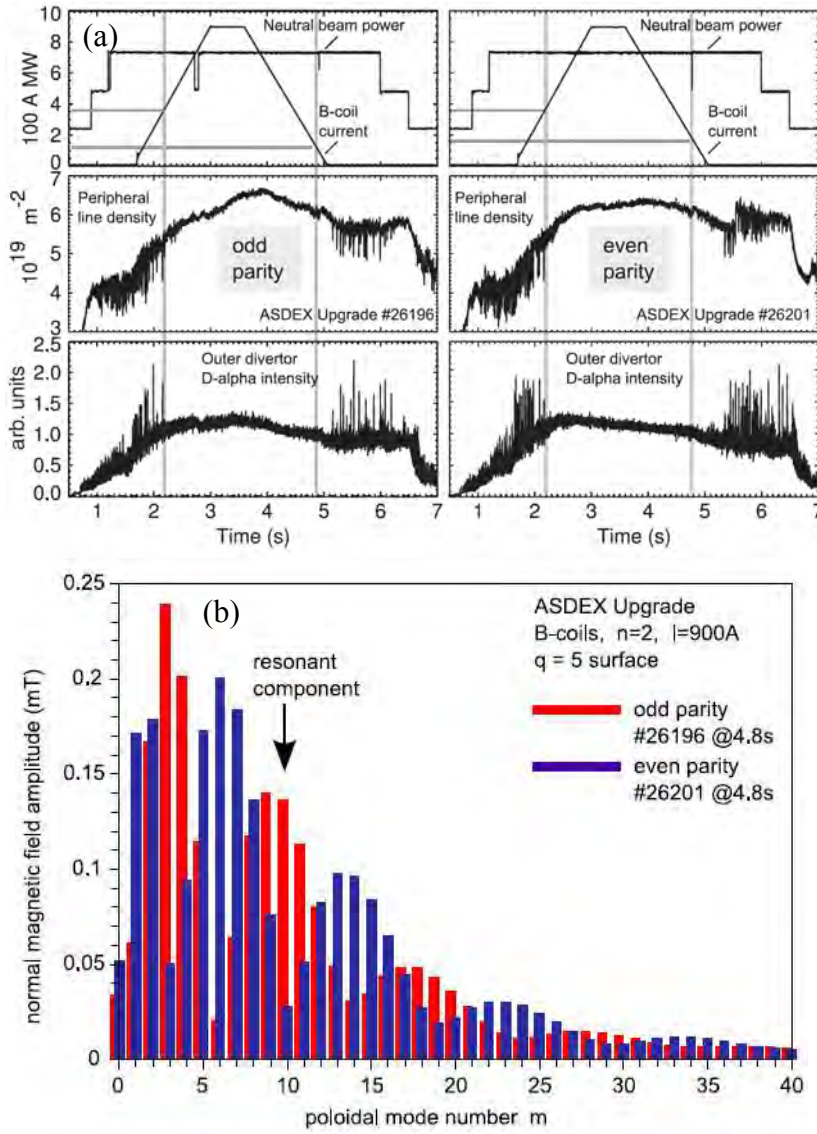


Figure 20

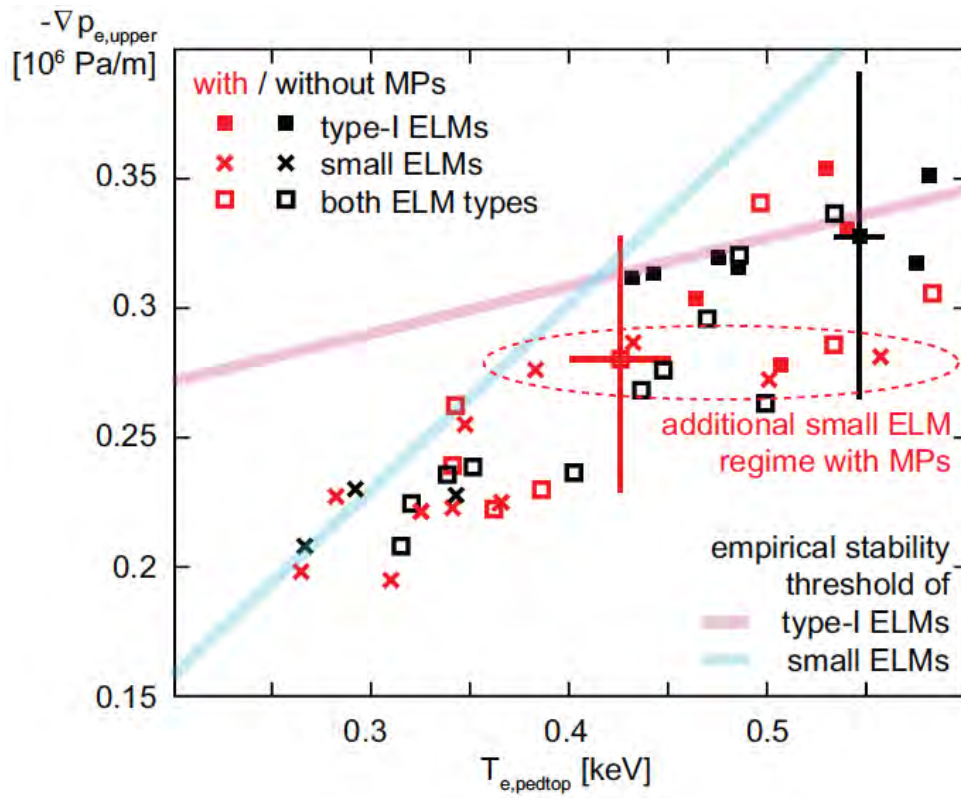


Figure 21

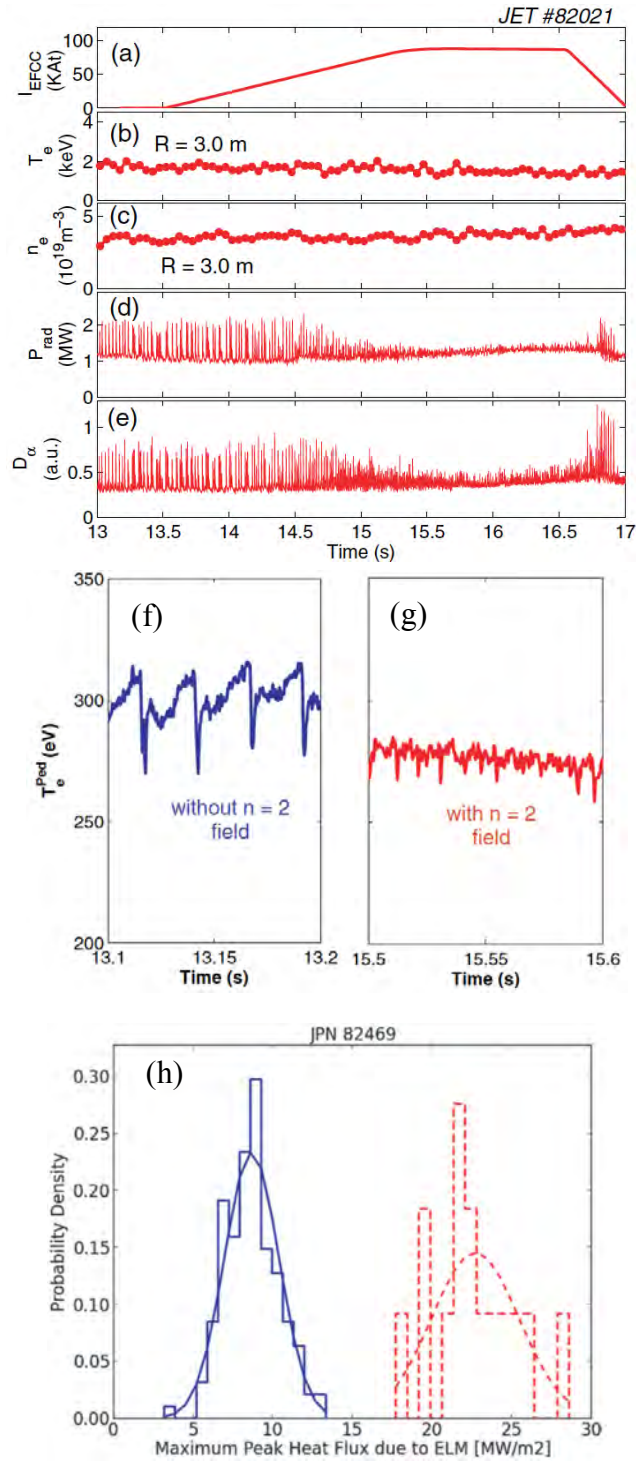


Figure 22

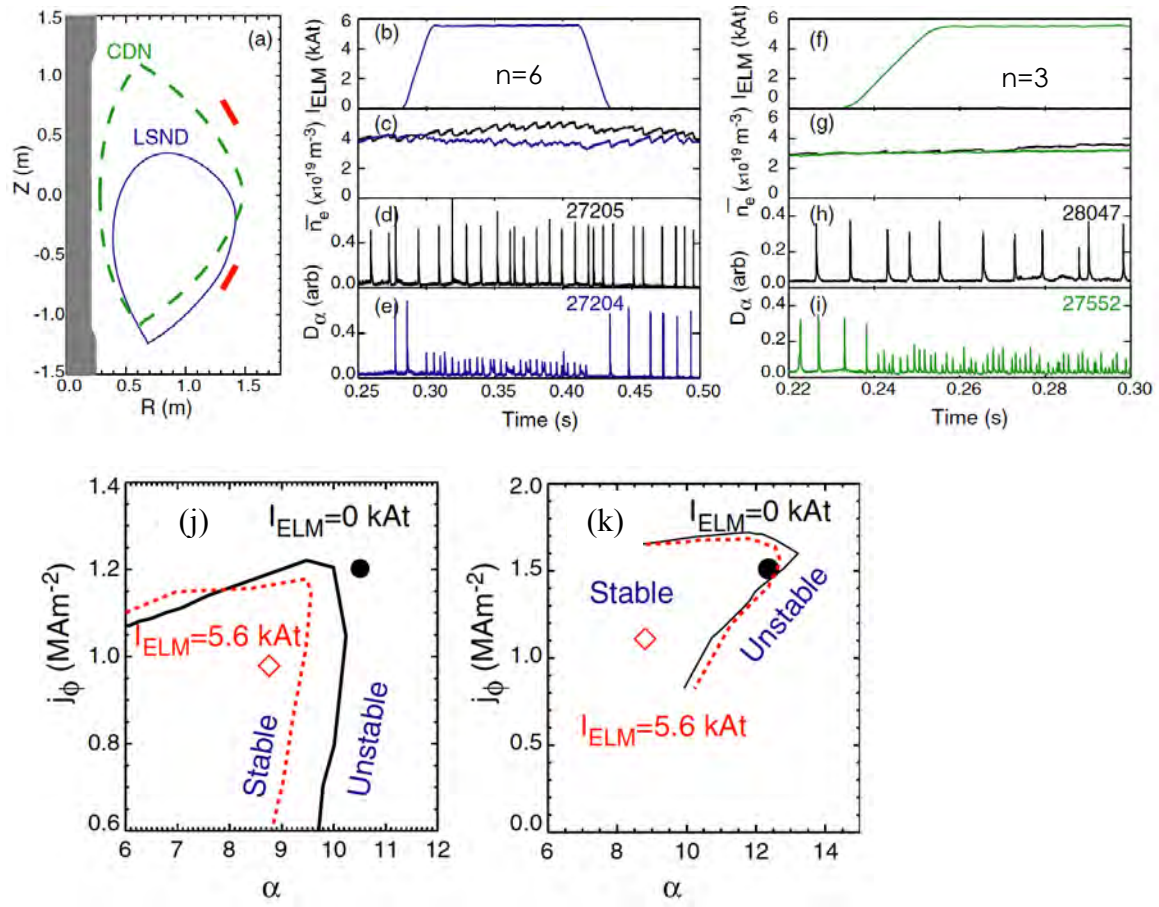


Figure 23

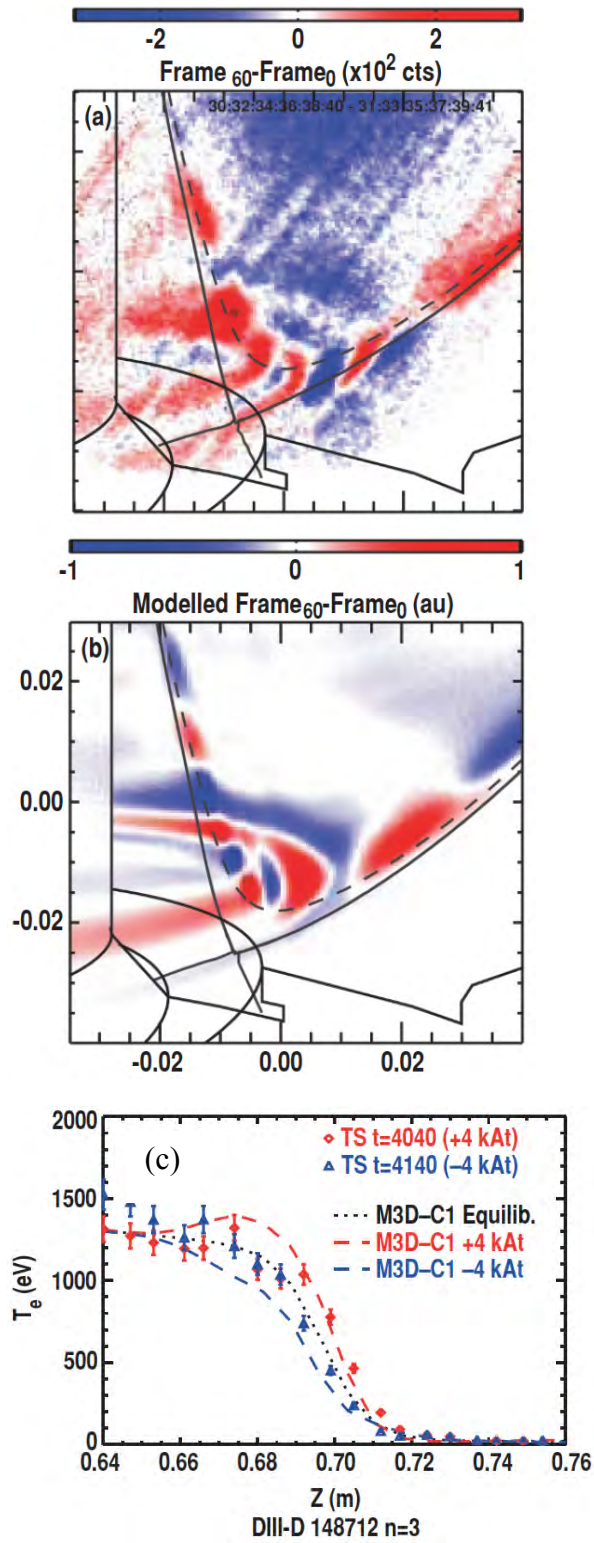


Figure 24

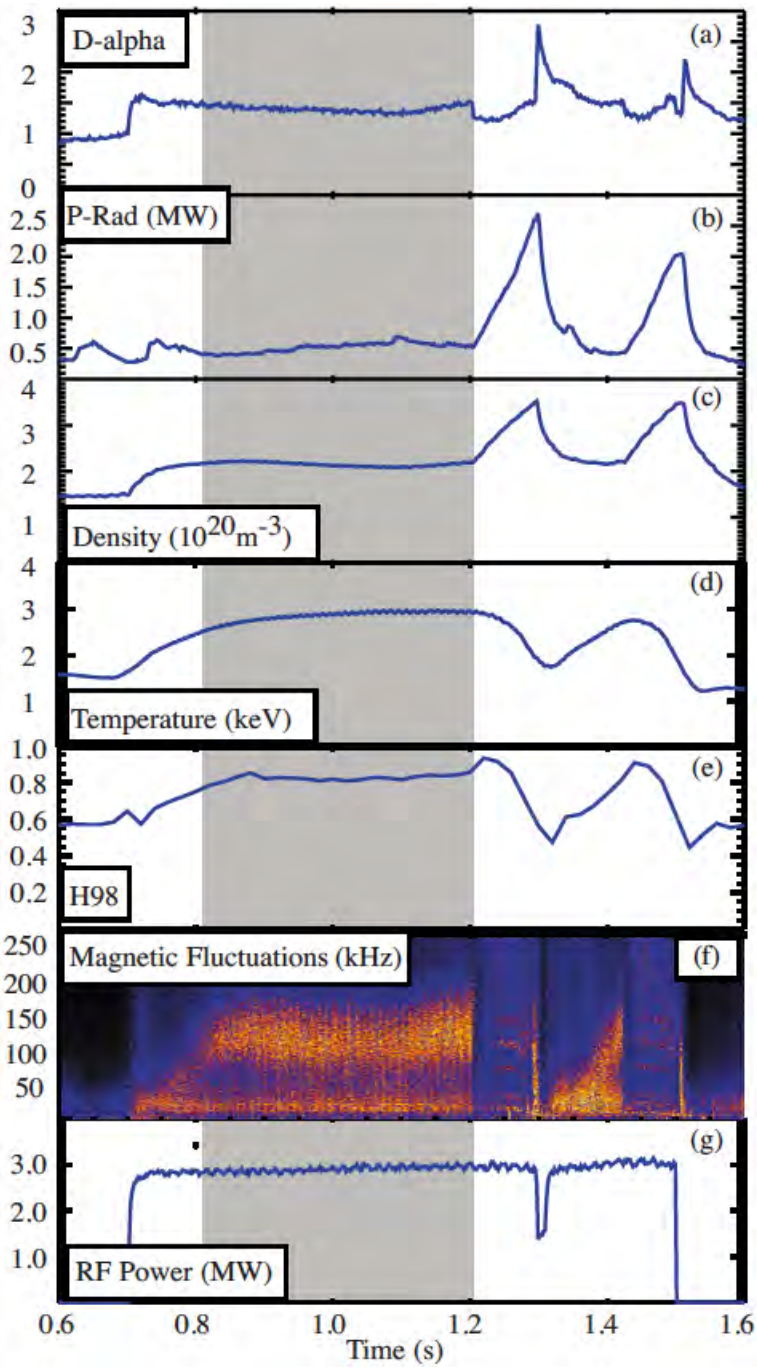


Figure 25

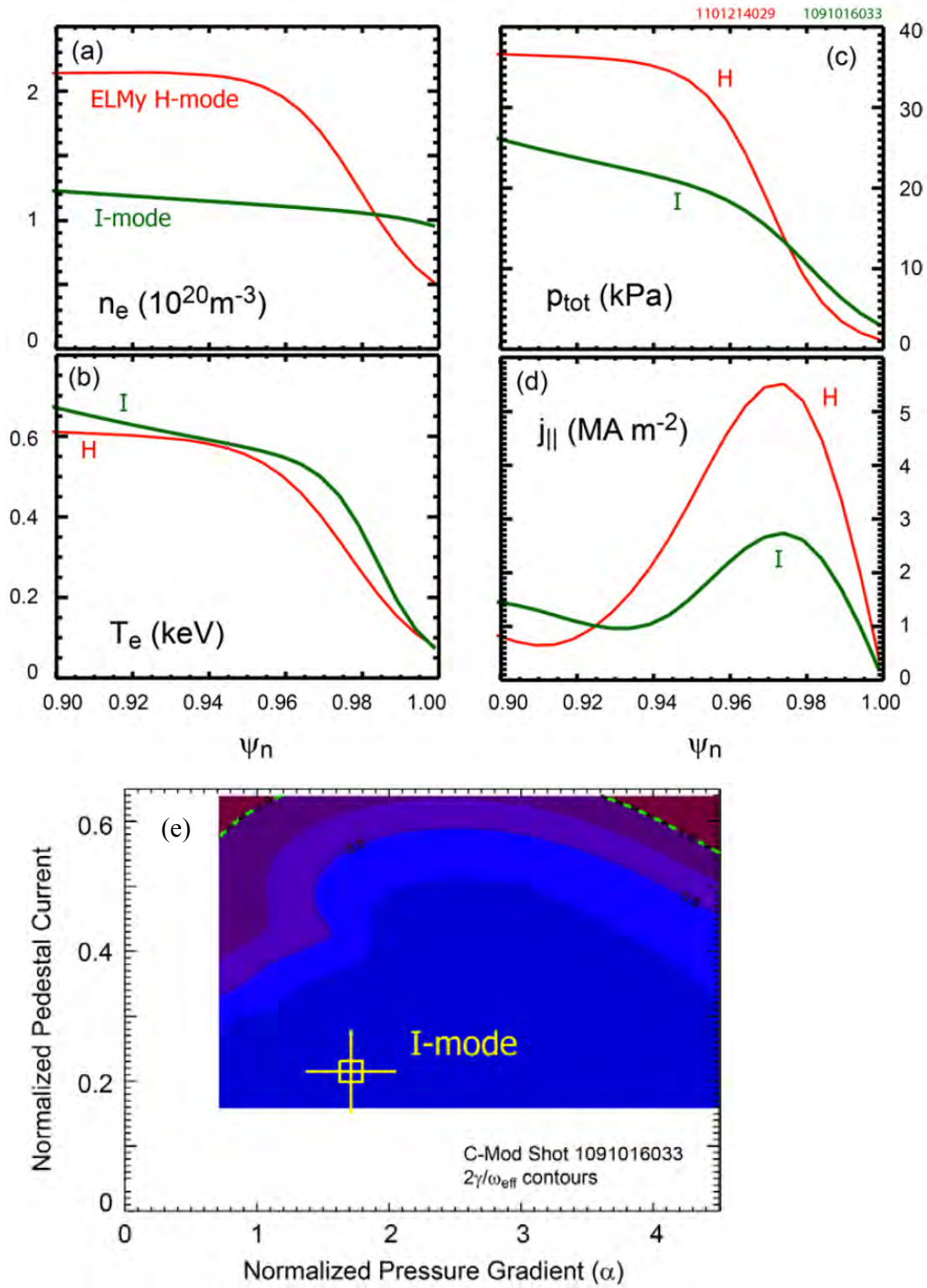


Figure 26

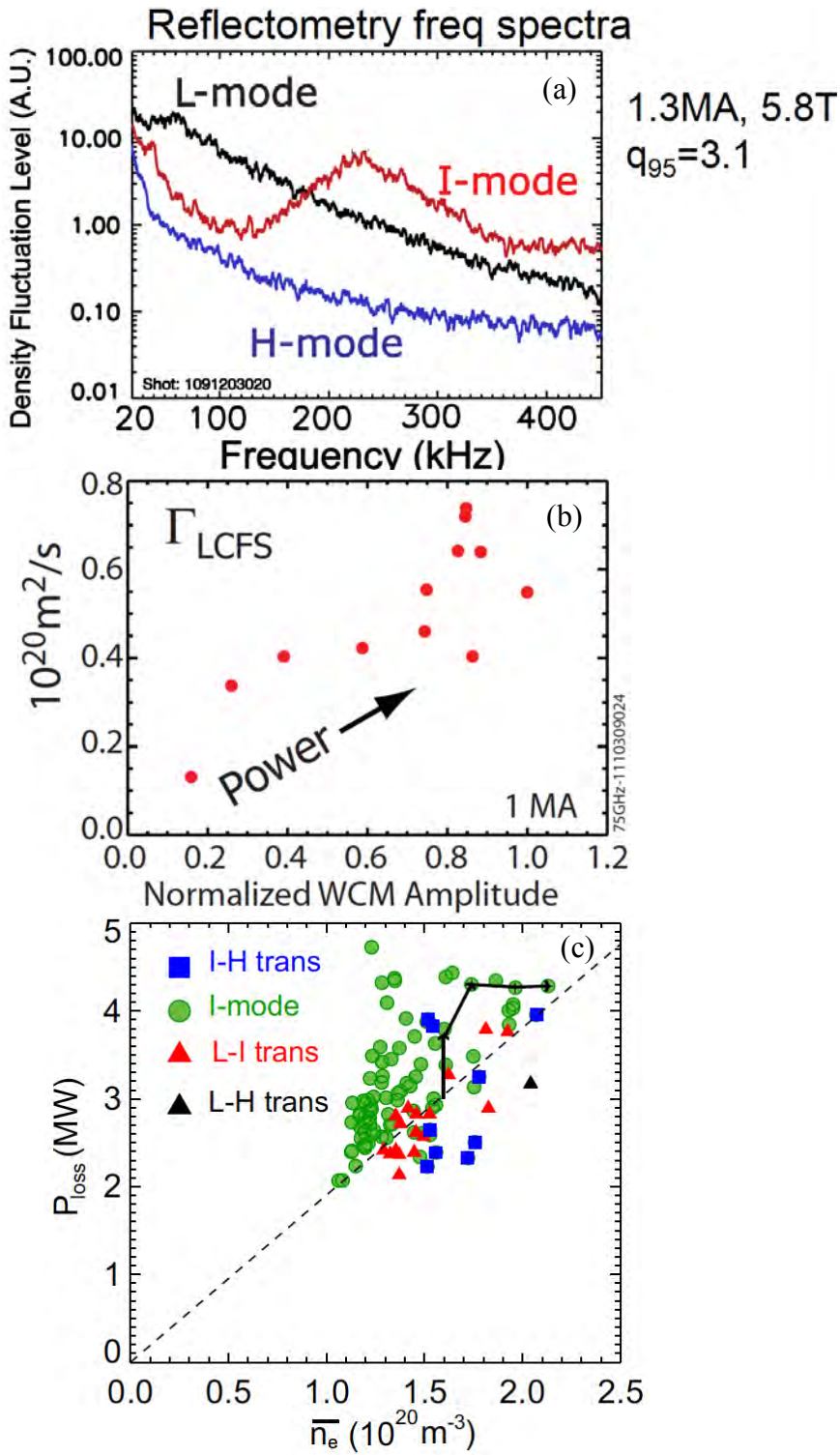


Figure 27

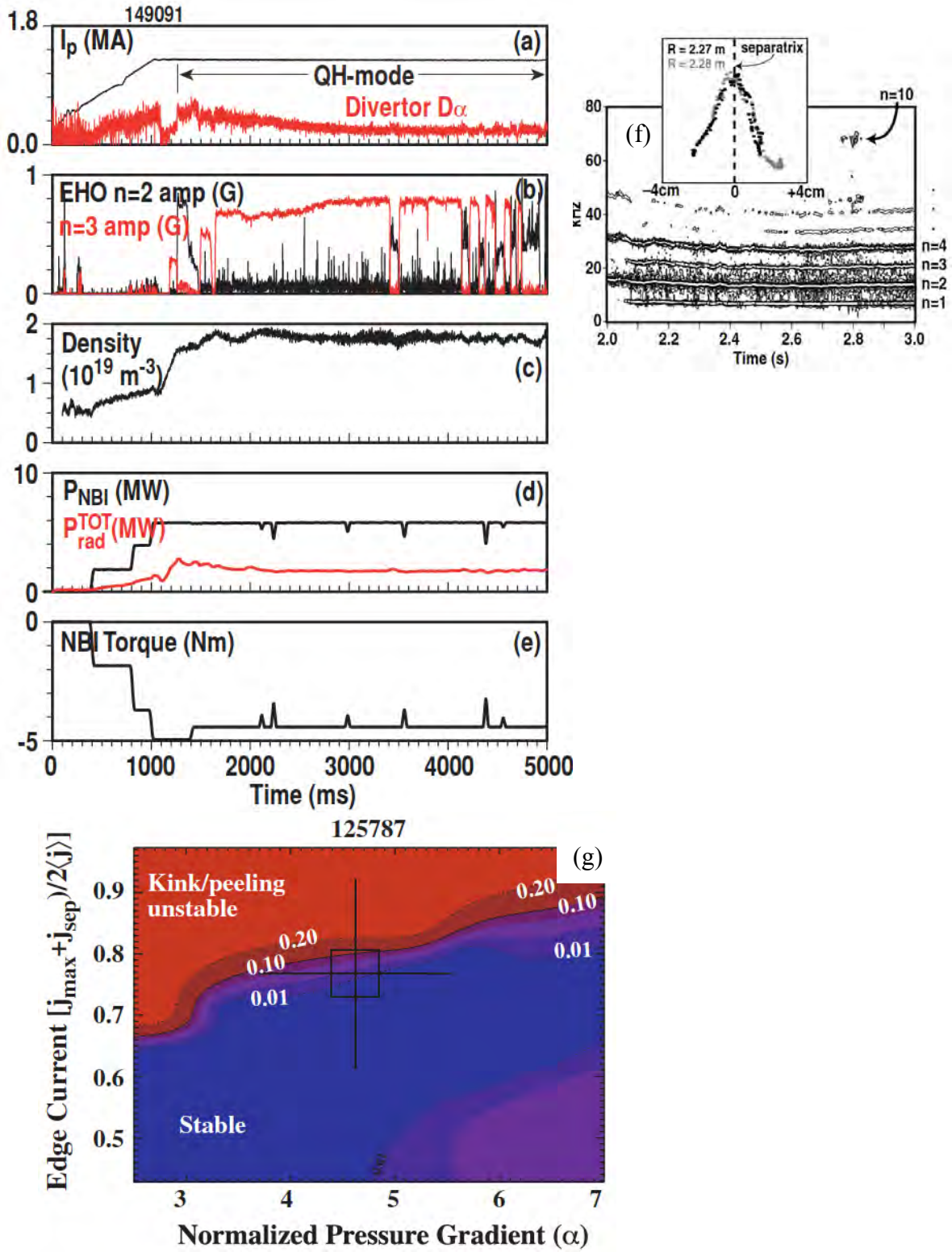


Figure 28

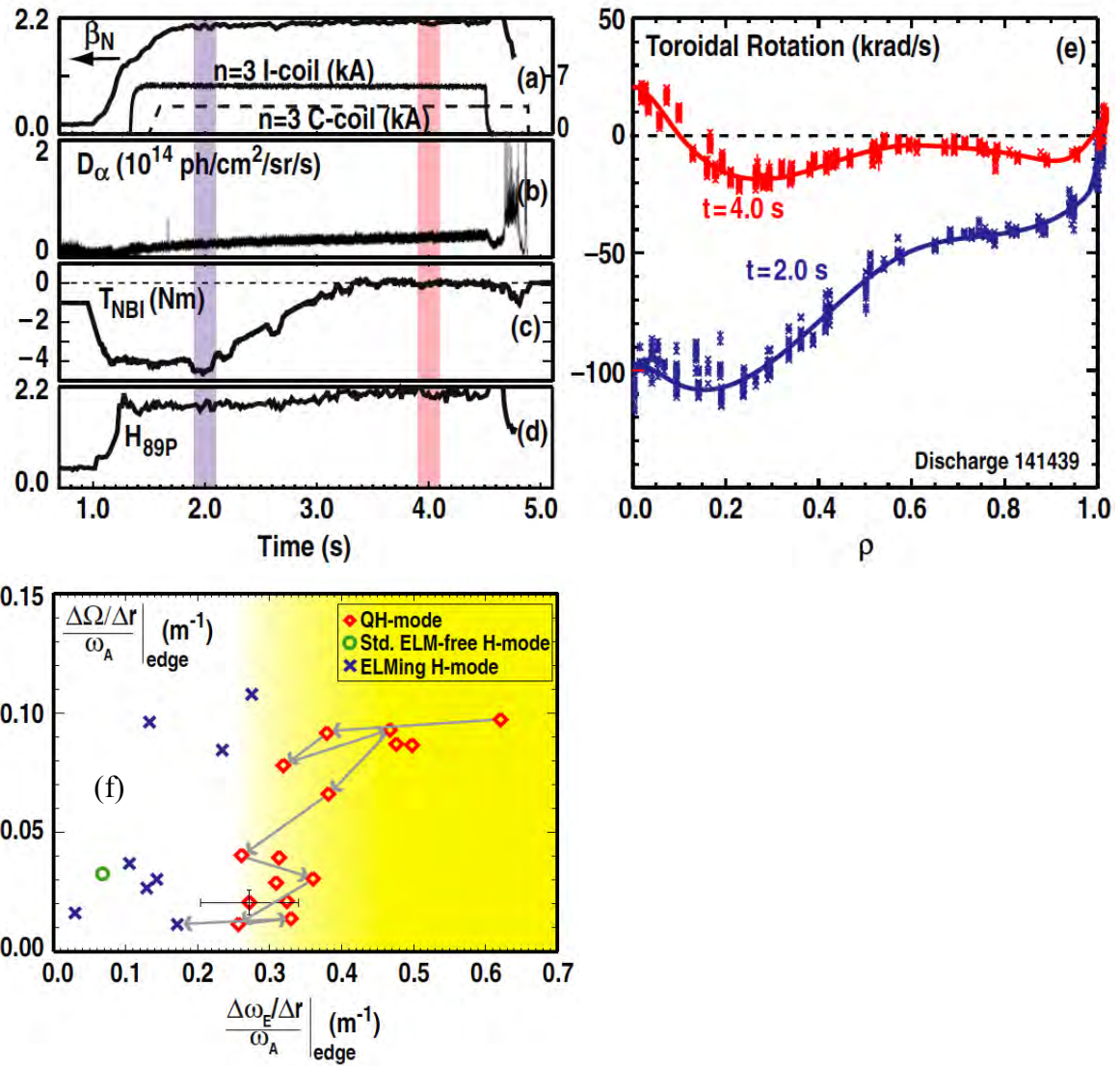


Figure 29

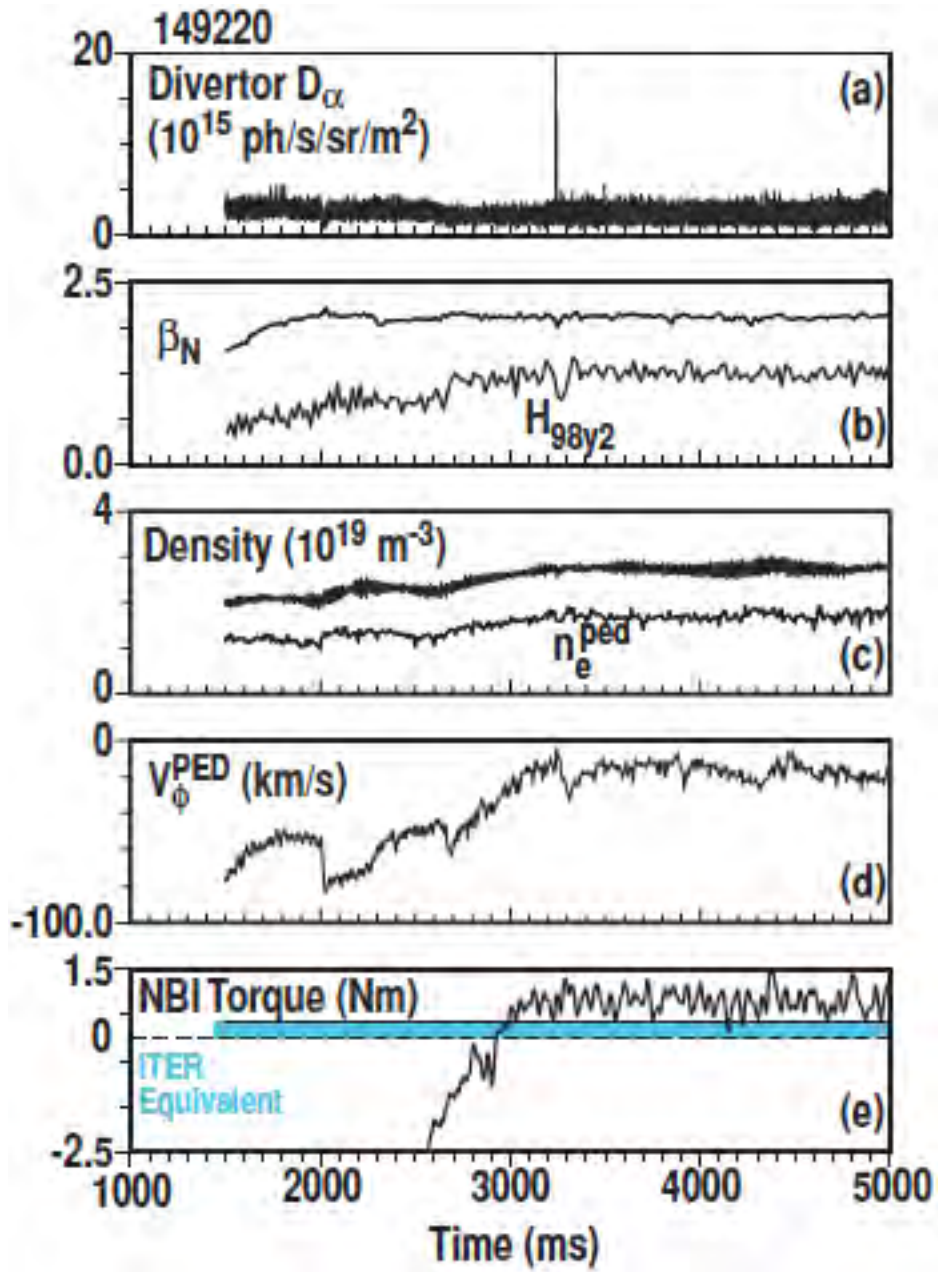


Figure 30

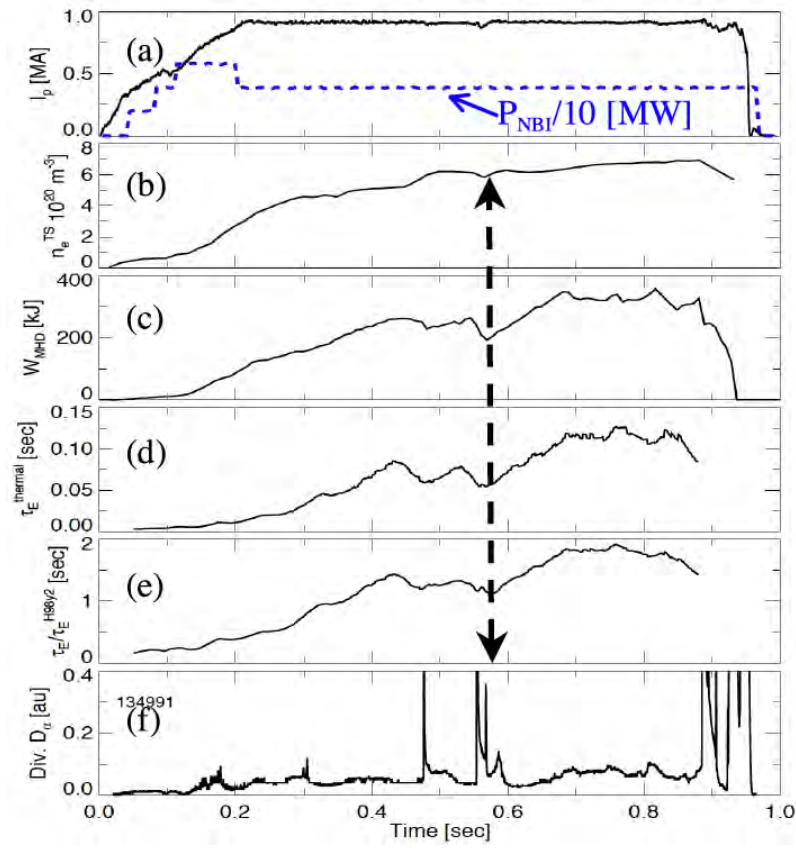


Figure 31

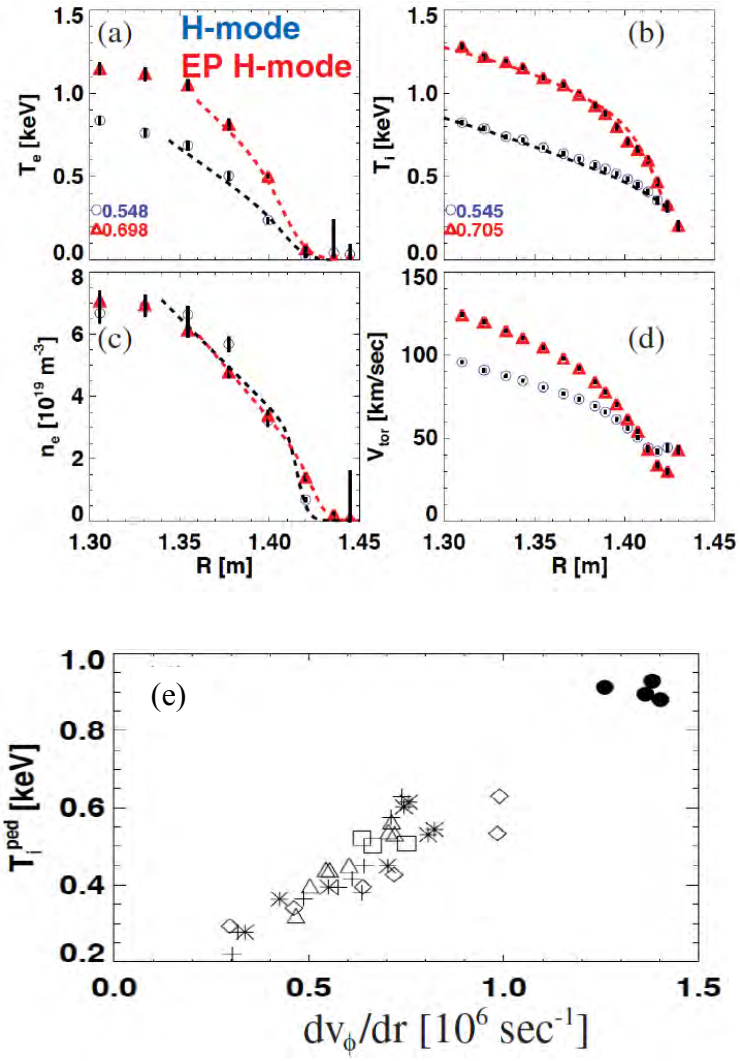


Figure 32

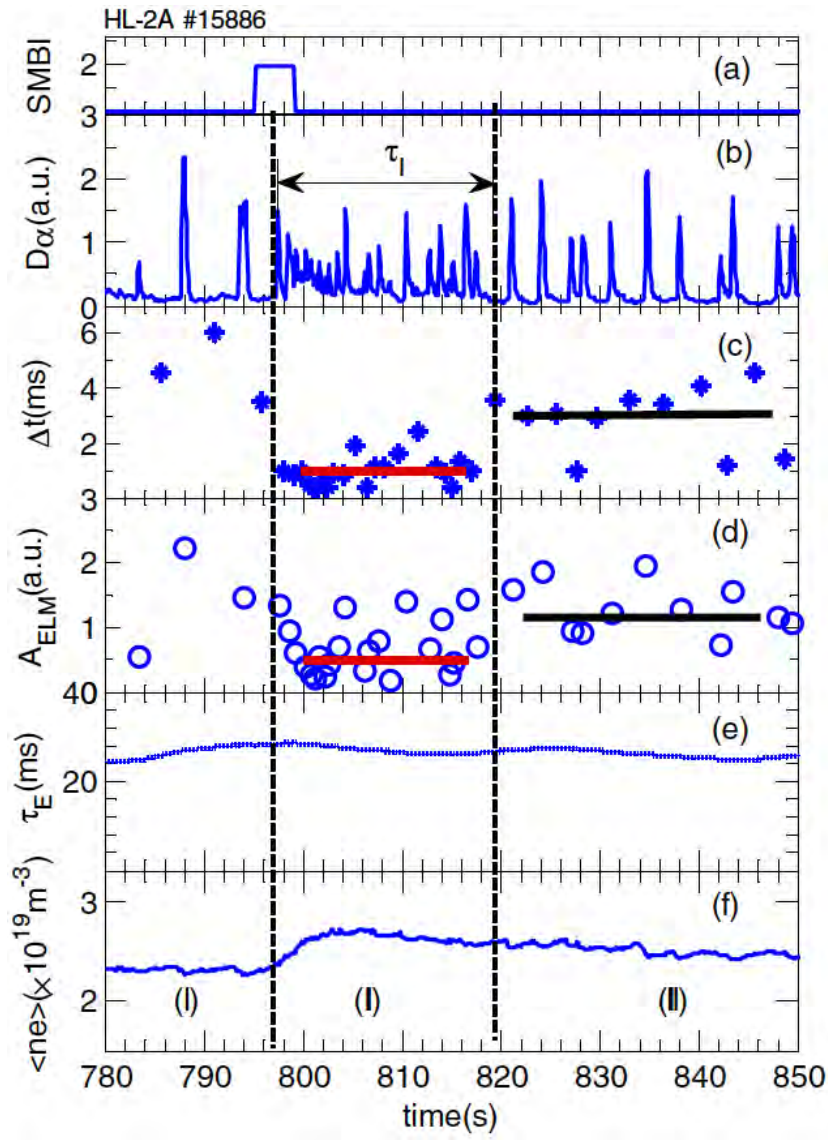


Figure 33

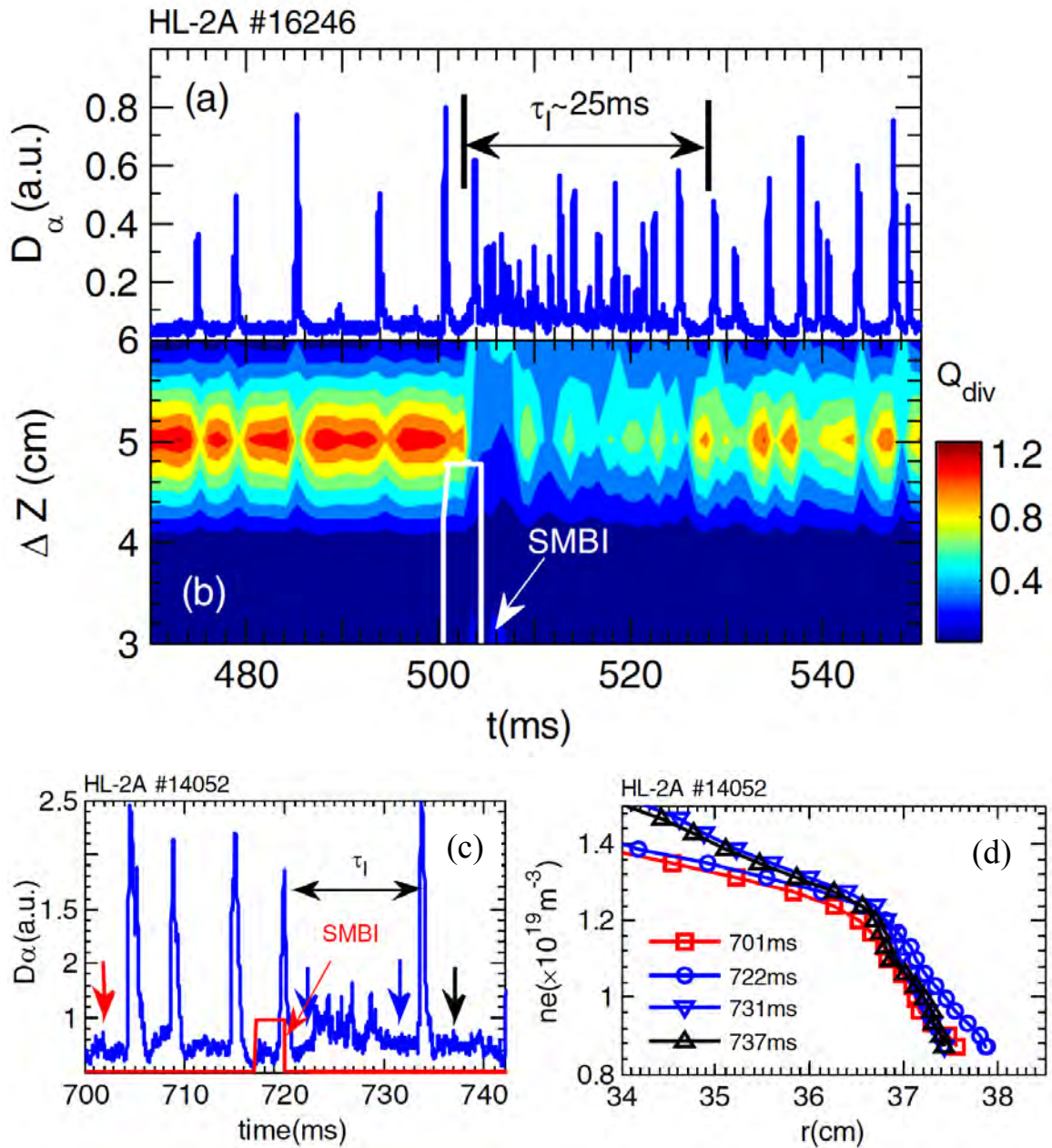


Figure 34

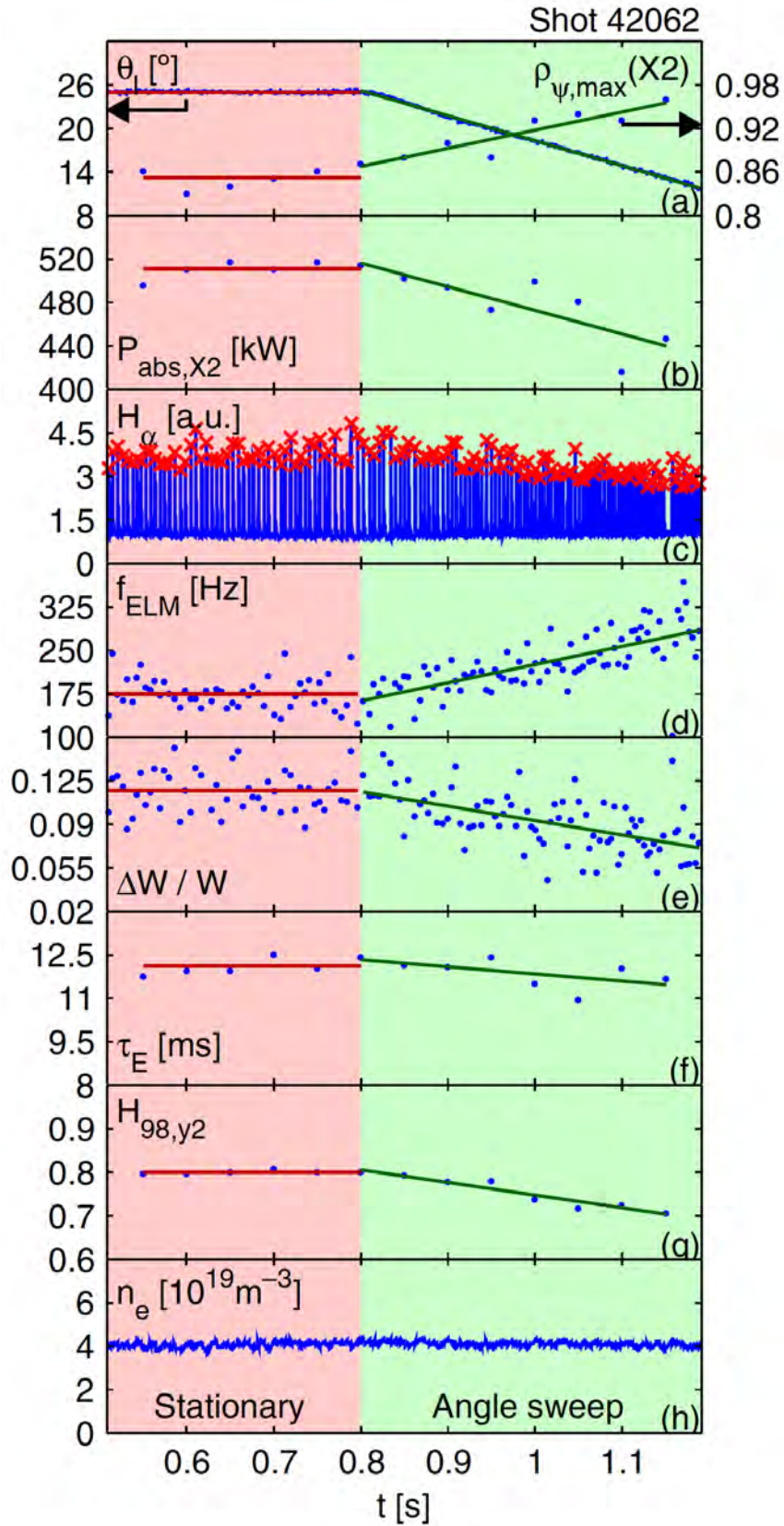


Figure 35

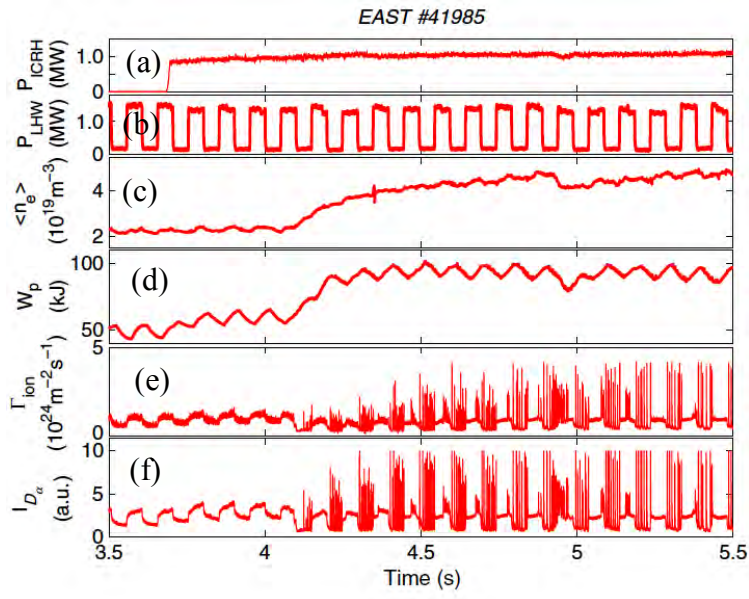


Figure 36

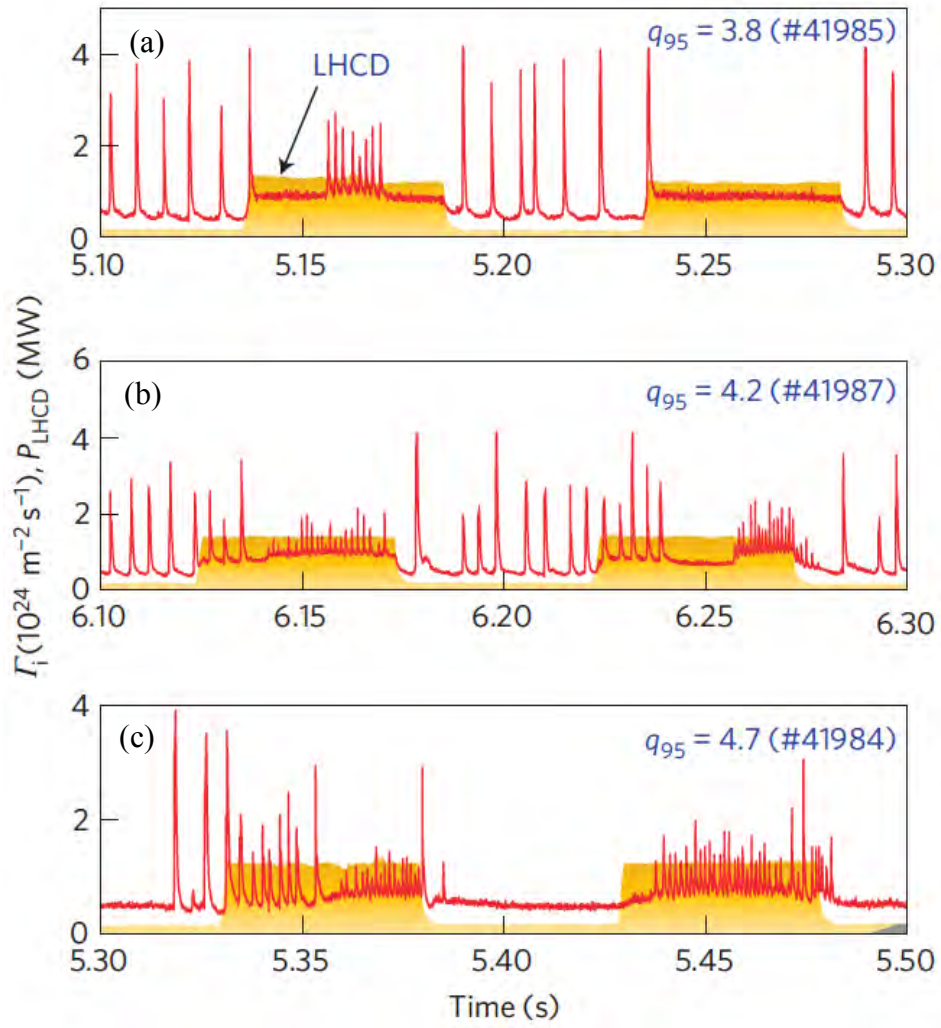


Figure 37

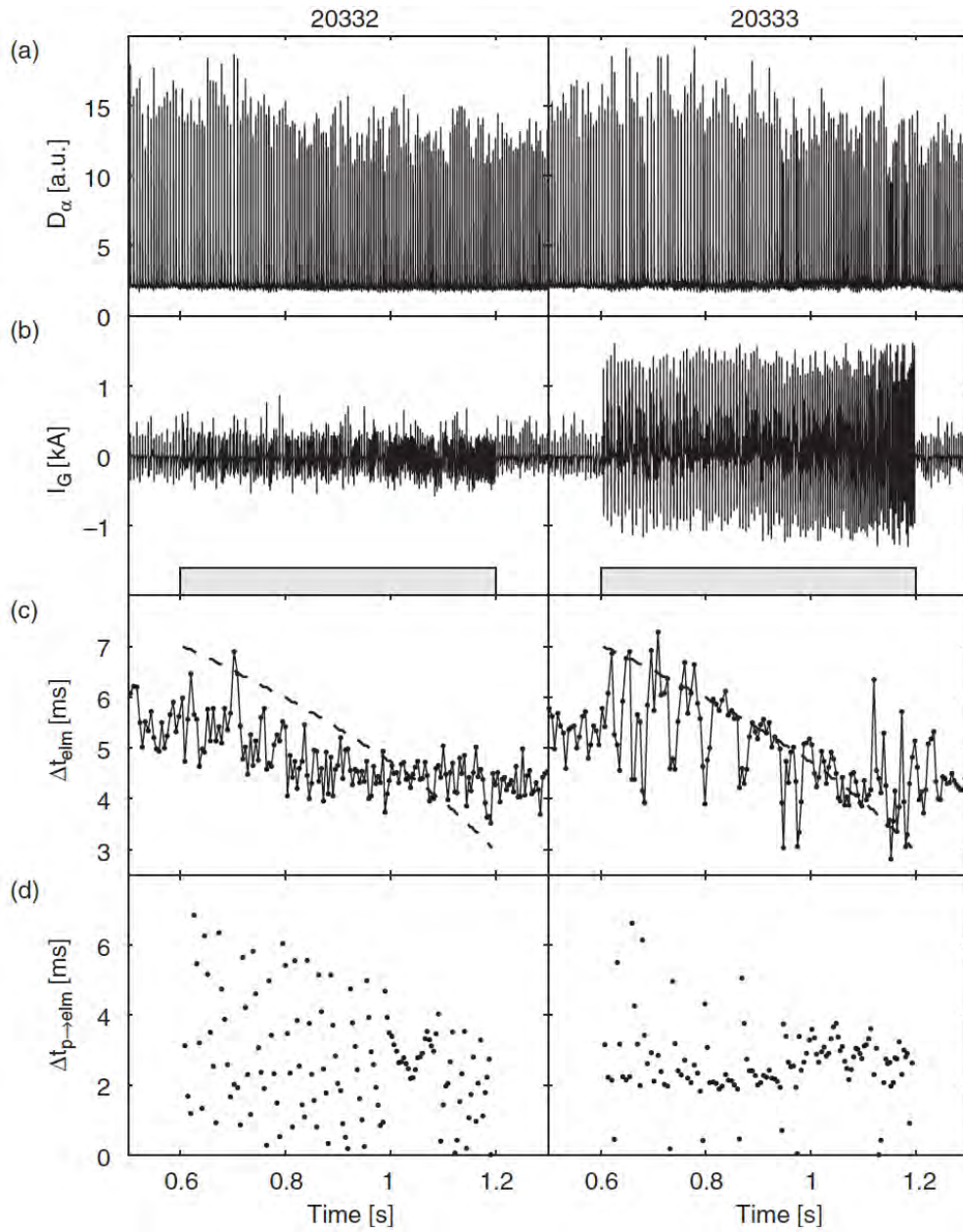


Figure 38

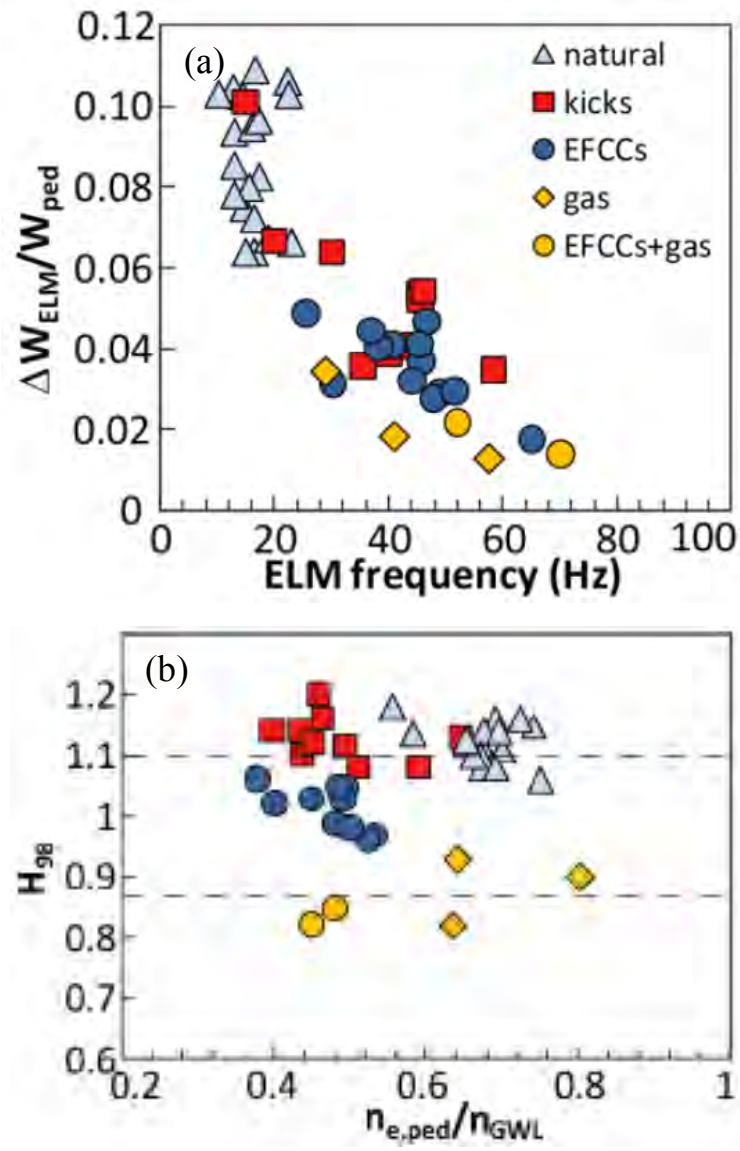


Figure 39

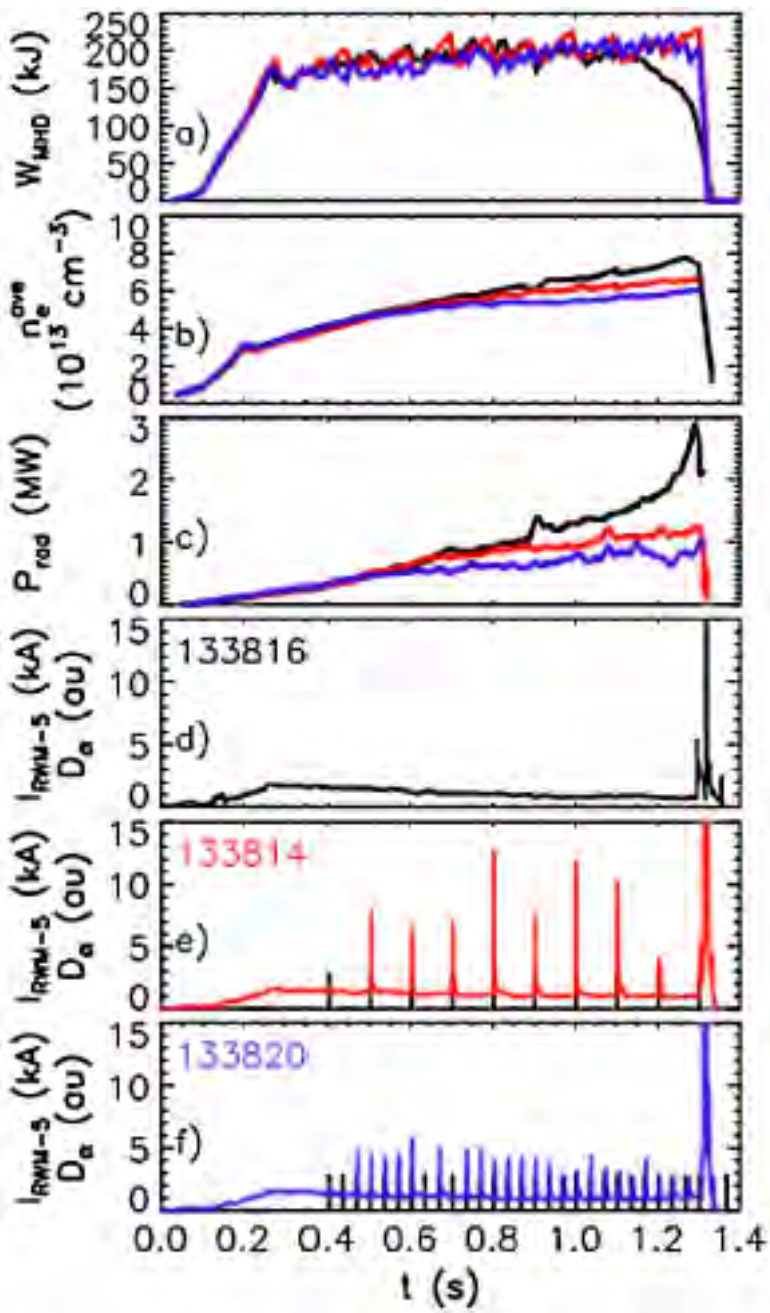


Figure 40

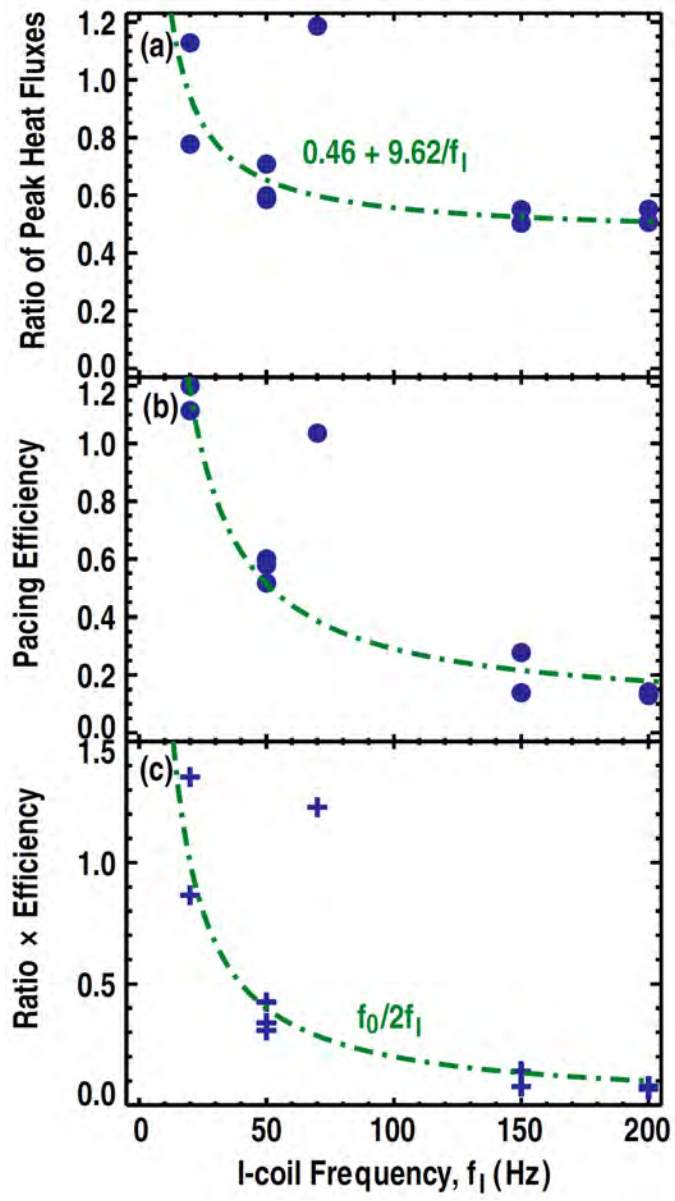


Figure 41

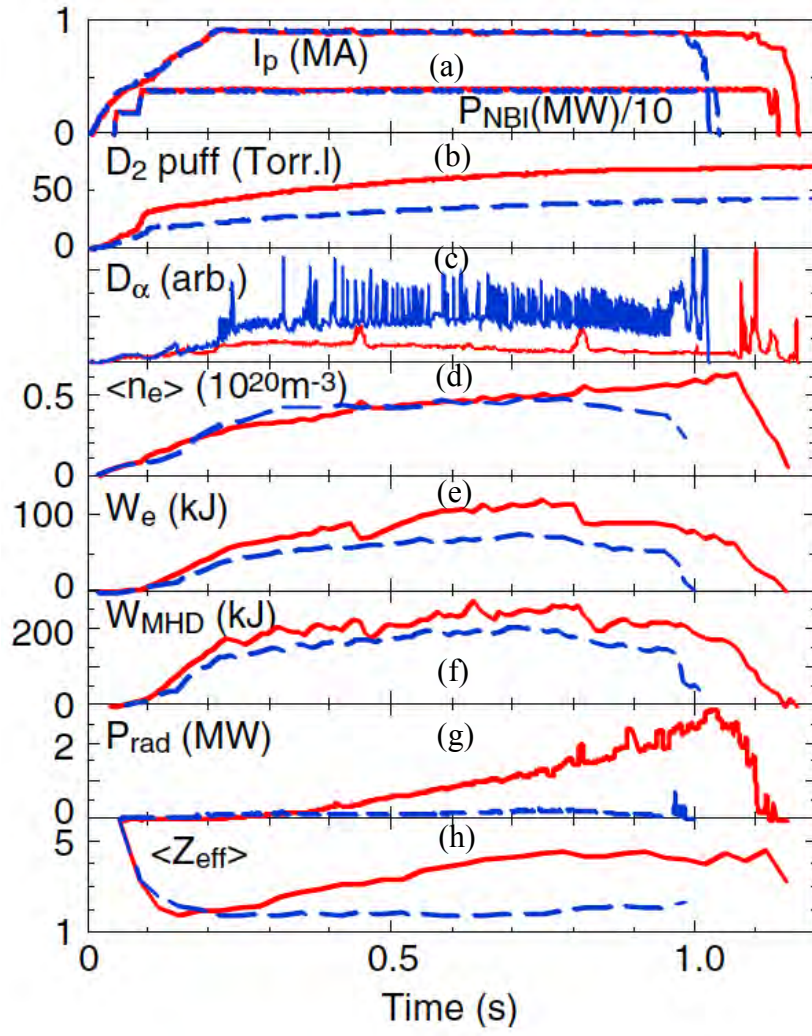


Figure 42

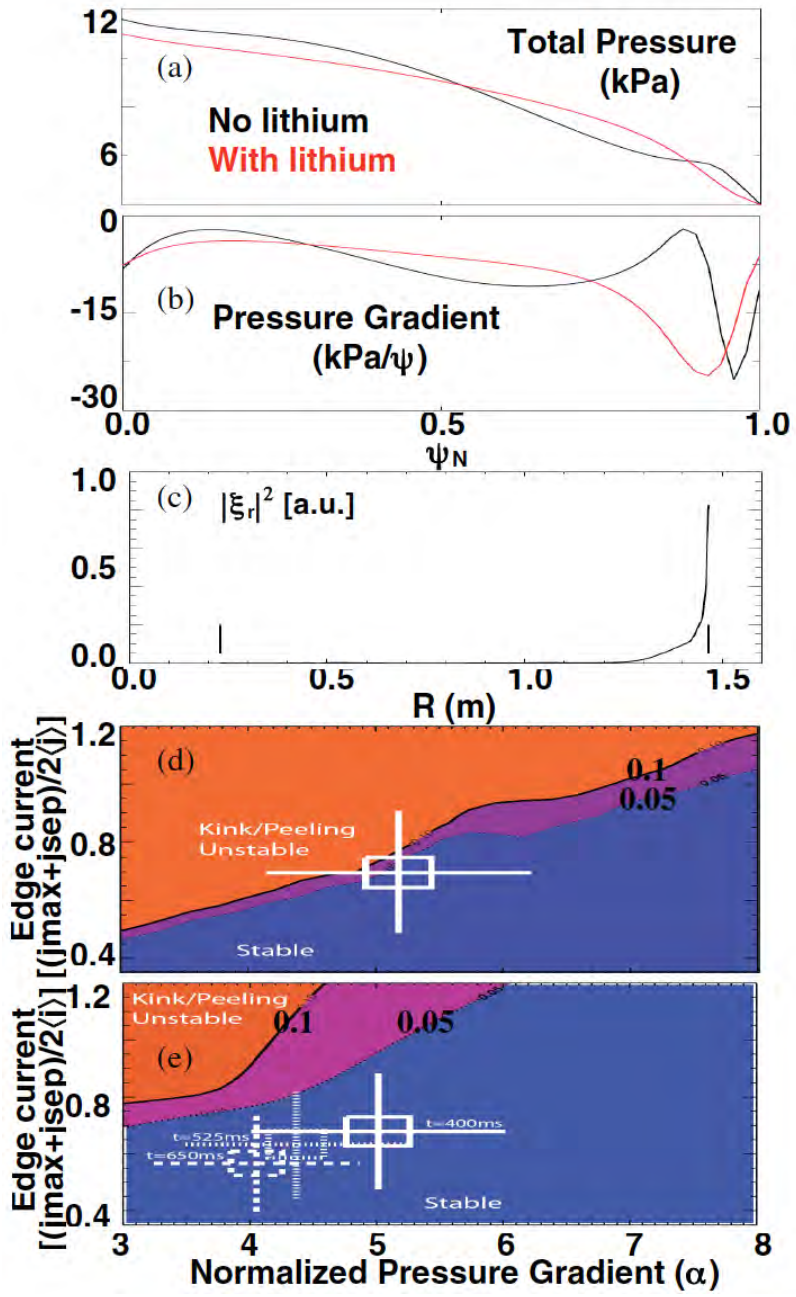
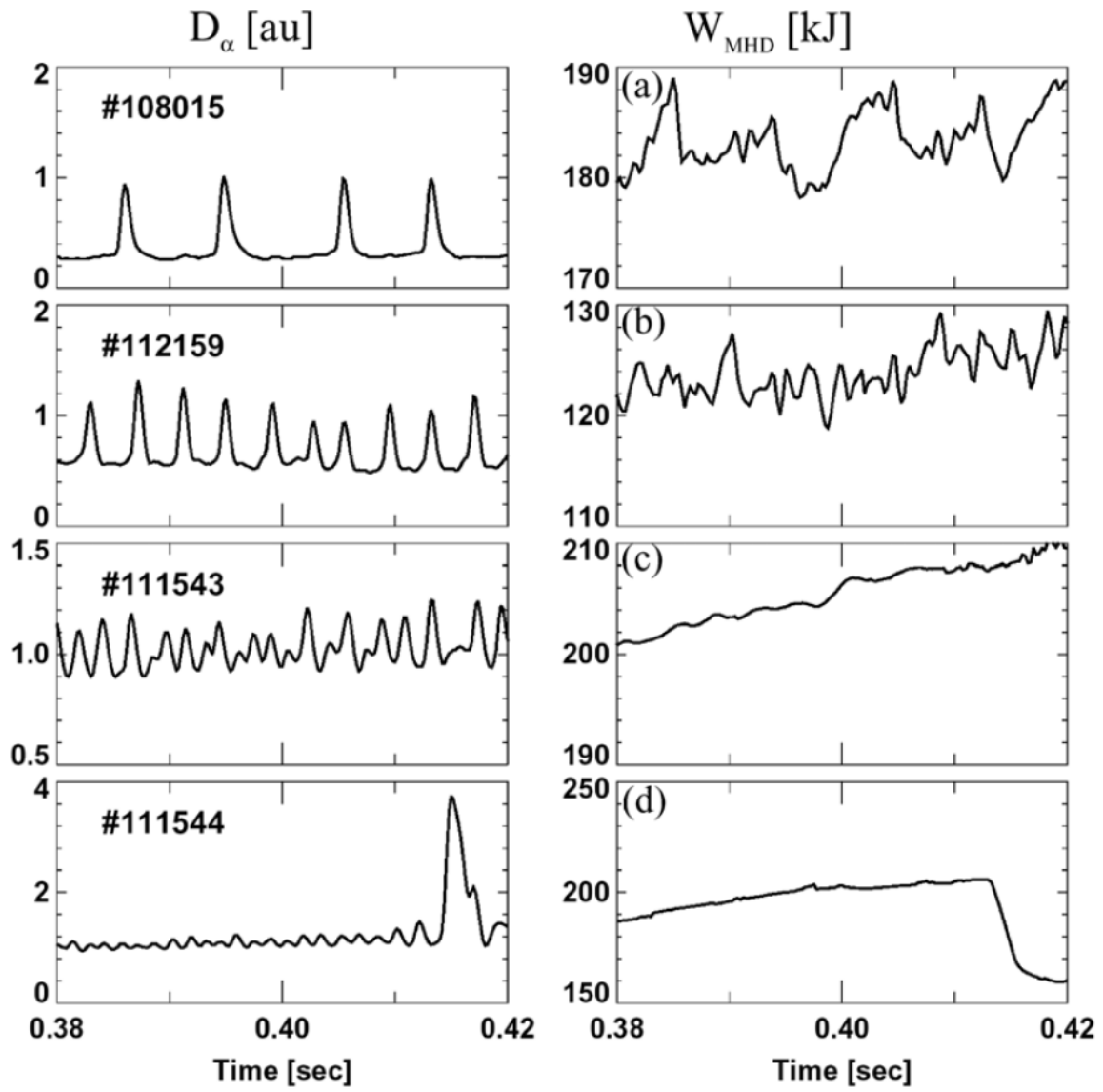


Figure 43



## References

- 1 *ITER organization website*, <http://www.iter.org>  
2 Wagner F., *et al.*, 1982 *Phys. Rev. Lett.* **49** 1408  
3 Kinsey J. E., *et al.*, 2011 *Nucl. Fusion* **51** 083001  
4 Zohm H., 1996 *Plasma Phys. Control. Fusion* **38** 105  
5 Leonard A. W., "ELMs in Tokamaks", 2014 *Phys. Plasmas* submitted  
6 Connor J. W., *et al.*, 1998 *Phys. Plasmas* **5** 2687  
7 Connor J. W., Hastie R. J., and Taylor J. B., 1978 *Phys. Rev. Lett.* **40** 396  
8 Manickam J., 1992 *Phys. Fluids B* **4** 1901  
9 Hill D. N., *et al.*, 1992 *J. Nucl. Mater.* **196-198** 204  
10 Zohm H., *et al.*, 1994 *Plasma Phys. Control. Fusion* **36** A129  
11 Leonard A. W., A. Herrmann, and Itami K., 1999 *J. Nucl. Mater.* **266-269** 109  
12 Loarte A., *et al.*, 2003 *J. Nucl. Mater.* **313-316** 962  
13 Federici G., *et al.*, 2003 *J. Nucl. Mater.* **313-316** 11  
14 Loarte A., *et al.*, in Fusion Energy 2008 (Proc. 22nd Int. Conf. Geneva, 2008)  
(Vienna: IAEA) CD-ROM file [IT/P6] and <http://www-naweb.iaea.org/naweb/physics/FEC/FEC2008/html/index.htm>  
15 Greenfield C. M., *et al.*, 2001 *Phys. Rev. Lett.* **86** 4544  
16 Evans T. E., *et al.*, 2004 *Phys. Rev. Lett.* **92** 235003  
17 Evans T. E., *et al.*, 2006 *Nature Physics* **2** 419  
18 Maingi R., *et al.*, 2009 *Phys. Rev. Lett.* **103** 075001  
19 Whyte D. G., *et al.*, 2010 *Nucl. Fusion* **50** 105005  
20 Suttrop W., *et al.*, 2011 *Phys. Rev. Lett.* **106**  
21 Greenwald M., *et al.*, 1999 *Phys. Plasmas* **6** 1943  
22 Oyama N., *et al.*, 2006 *Plasma Phys. Control. Fusion* **48** A171  
23 Lang P. T., *et al.*, 2013 *Nucl. Fusion* **53** 043004  
24 Evans T. E., 2013 *J. Nucl. Mater.* **438** S11  
25 Loarte A., *et al.*, 2014 *Nucl. Fusion* **54** 033007  
26 Snyder P. B., *et al.*, 2002 *Phys. Plasmas* **9** 2037  
27 Wilson H. R., *et al.*, 2006 *Plasma Phys. Control. Fusion* **48** A71  
28 Wilson H. R., *et al.*, 2002 *Phys. Plasmas* **9** 1277  
29 Cowley S. C. and Artun M., 1997 *Physics Reports* **283** 185  
30 Cowley S. C., *et al.*, 2003 *Plasma Physics Controlled Fusion* **45** A31  
31 Wilson H. R. and Cowley S. C., 2004 *Phys. Rev. Lett.* **92** 175006  
32 Zhu P. and Hegna C. C., 2008 *Phys. Plasmas* **15** 092306  
33 Snyder P. B., *et al.*, 2009 *Nucl. Fusion* **49** 085035  
34 Snyder P. B., *et al.*, 2009 *Phys. Plasmas* **16** 056118  
35 Snyder P. B., *et al.*, 2011 *Nucl. Fusion* **51** 103016  
36 Osborne T. H., *et al.*, 2008 *J. Phys.: Conf. Series* **123** 012014  
37 Eich T., *et al.*, 2011 *Phys. Rev. Lett.* **107** 215001  
38 Makowski M. A., *et al.*, 2012 *Phys. Plasmas* **19** 056122  
39 Goldston R. J., 2012 *Nucl. Fusion* **52** 013009  
40 Eich T., *et al.*, 2013 *Nucl. Fusion* **53** 093031  
41 Eich T., *et al.*, 2011 *J. Nucl. Mater.* **415** S856  
42 Jakubowski M. W., *et al.*, 2009 *Nucl. Fusion* **49** 095013

43 Ahn J. W., *et al.*, 2013 *J. Nucl. Mater.* **438** S317  
44 Loarte A., *et al.*, 2002 *Plasma Phys. Control. Fusion* **44** 1815  
45 Lang P. T., *et al.*, 2003 *Nucl. Fusion* **43** 1110  
46 Lang P. T., *et al.*, 1997 *Phys. Rev. Lett.* **79** 1487  
47 Baylor L. R., *et al.*, 2000 *Phys. Plasmas* **7** 1878  
48 Maingi R., *et al.*, 1997 *Phys. Plasmas* **4** 1752  
49 Baylor L. R., *et al.*, 2013 *Bull. Am. Phys. Soc.* **58** 239  
50 Milora S. L., *et al.*, 1995 *Nucl. Fusion* **35** 697  
51 Huysmans G., S. Pamela, E. van der Plas, and P. Ramet, 2009 *Plasma Phys. Control. Fusion* **51** 124012  
52 Baylor L. R., *et al.*, 2013 *Phys. Rev. Lett.* **110**  
53 Lang P. T., *et al.*, 2013 *Nucl. Fusion* **53** 073010  
54 Baylor L. R., *et al.*, 2012 Proc. 24th Int. Conf. on Fusion Energy (San Diego, 2012) [EX/6-02] <http://www-naweb.iaea.org/naweb/physics/FEC/FEC2012/index.htm>  
55 Lang P. T., *et al.*, 2014 *Nucl. Fusion* **54** at press  
56 Mansfield D. K., *et al.*, 2013 *Nucl. Fusion* **53** 113023  
57 Futatani S., *et al.*, 2012 Proc. 24th Int. Conf. on Fusion Energy (San Diego, 2012) [ITR/P1-22] <http://www-naweb.iaea.org/naweb/physics/FEC/FEC2012/index.htm>  
58 Maruyama S., *et al.*, 2012 Proc. 24th Int. Conf. on Fusion Energy (San Diego, 2012) [ITR/P5-24] <http://www-naweb.iaea.org/naweb/physics/FEC/FEC2012/index.htm>  
59 Fenstermacher M. E., *et al.*, 2008 *Phys. Plasmas* **15** 056122  
60 Fenstermacher M. E., *et al.*, 2008 *Nucl. Fusion* **48** 122001  
61 Lanctot M. J., *et al.*, 2013 *Nucl. Fusion* **53** 083019  
62 Evans T. E. and the D.-D. T., 2012 *Plasma and Fusion Research* **7** 2402046  
63 Petrie T. W., *et al.*, 2011 *Nucl. Fusion* **51** 073003  
64 Liang Y., *et al.*, 2007 *Phys. Rev. Lett.* **98**  
65 Liang Y., *et al.*, 2010 *Phys. Rev. Lett.* **105**  
66 Liang Y., *et al.*, 2010 *Nucl. Fusion* **50** 025013  
67 Liang Y., *et al.*, 2013 *Nucl. Fusion* **53** 073036  
68 Barrera L., *et al.*, 2013 Proc. 40th Euro. Conference on Plasma Physics and Controlled Fusion, Espoo, Finland, 1-5 July 2013 P4.113  
69 Rathgeber S. K., *et al.*, 2013 Proc. 40th Euro. Conference on Plasma Physics and Controlled Fusion, Espoo, Finland, 1-5 July 2013 P4.108  
70 Suttrop W., *et al.*, 2011 *Plasma Phys. Control. Fusion* **53** 124014  
71 Fischer R., *et al.*, 2012 *Plasma Phys. Control. Fusion* **54** 115008  
72 Jeon Y., *et al.*, 2012 *Phys. Rev. Lett.* **109**  
73 Kwak J. G., *et al.*, 2013 *Nucl. Fusion* **53** 104005  
74 Kirk A., *et al.*, 2010 *Nucl. Fusion* **50** 034008  
75 Liu Y., *et al.*, 2011 *Nucl. Fusion* **51** 083002  
76 Chapman I. T., *et al.*, 2012 *Nucl. Fusion* **52** 123006  
77 Kirk A., *et al.*, 2013 *Nucl. Fusion* **53** 043007  
78 Kirk A., *et al.*, 2013 *Plasma Phys. Control. Fusion* **55** 124003  
79 Evans T. E., *et al.*, 2006 *Phys. Plasmas* **13** 056121  
80 Evans T. E., *et al.*, 2008 *Nucl. Fusion* **48** 024002

81 Groebner R. J. and Osborne T. H., 1998 *Phys. Plasmas* **5** 1800  
82 Snyder P. B., *et al.*, 2007 *Nucl. Fusion* **47** 961  
83 Snyder P. B., *et al.*, 2012 *Phys. Plasmas* **19** 056115  
84 Ferraro N. M., *et al.*, 2013 *Nucl. Fusion* **53** 073042  
85 Yun G., *et al.*, 2011 *Phys. Rev. Lett.* **107**  
86 Orlov D. M., 2013 *Bull. Am. Phys. Soc.* **58** 369  
87 Evans T. E., *et al.*, 2013 *Nucl. Fusion* **53** 093029  
88 Greenwald M., *et al.*, 1988 *Nucl. Fusion* **28** 2199  
89 Lang P. T., *et al.*, 2012 *Nucl. Fusion* **52** 023017  
90 Suttrop W., *et al.*, 2013 *Proc. 40th Euro. Conference on Plasma Physics and  
Controlled Fusion, Espoo, Finland, 1-5 July 2013* P4.117  
91 Evans T. E., *et al.*, 2005 *Nucl. Fusion* **45** 595  
92 Kirk A., *et al.*, 2012 *Phys. Rev. Lett.* **108**  
93 Bécoulet M., *et al.*, 2008 *Nucl. Fusion* **48** 024003  
94 Bécoulet M., *et al.*, 2009 *Nucl. Fusion* **49** 085011  
95 Nardon E., *et al.*, 2010 *Nucl. Fusion* **50** 034002  
96 Becoulet M., *et al.*, 2012 *Nucl. Fusion* **52** 054003  
97 Ferraro N. M., 2012 *Phys. Plasmas* **19** 056105  
98 Waelbroeck F. L., *et al.*, 2012 *Nucl. Fusion* **52** 074004  
99 Evans T. E., *et al.*, 2005 *J. Physics: Conf. Series* **7** 174  
100 Shafer M. W., *et al.*, 2012 *Nucl. Fusion* **52** 122001  
101 Wingen A., *et al.*, 2014 *Nucl. Fusion* **54** 064007  
102 Wade M. R., *et al.*, “Advances in the Physics Understanding of ELM Suppression  
Using Resonant Magnetic Perturbations in DIII-D”, 2014 *Nucl. Fusion* **54**  
submitted 3/2014.  
103 Shafer M. W., *et al.*, 2010 *The Review of scientific instruments* **81** 10E534  
104 McDermott R. M., *et al.*, 2009 *Phys. Plasmas* **16** 056103  
105 Ryter F., *et al.*, 1998 *Plasma Phys. Control. Fusion* **40** 725  
106 Hubbard A. E., *et al.*, 2011 *Phys. Plasmas* **18** 056115  
107 Hubbard A. E., *et al.*, 2012 *Nucl. Fusion* **52** 114009  
108 Hughes J. W., *et al.*, 2013 *Nucl. Fusion* **53** 043016  
109 White A. E., *et al.*, 2011 *Nucl. Fusion* **51** 113005  
110 Burrell K. H., *et al.*, 2001 *Phys. Plasmas* **8** 2153  
111 Burrell K. H., *et al.*, 2009 *Nucl. Fusion* **49** 085024  
112 Garofalo A. M., *et al.*, 2011 *Nucl. Fusion* **51** 083018  
113 Burrell K. H., *et al.*, 2012 *Phys. Plasmas* **19** 056117  
114 Burrell K. H., *et al.*, 2013 *Nucl. Fusion* **53** 073038  
115 Maingi R., *et al.*, 2009 *J. Nucl. Mater.* **390-391** 440  
116 Maingi R., *et al.*, 2010 *Phys. Rev. Lett.* **105** 135004  
117 Gerhardt S. P., *et al.*, 2014 *Nucl. Fusion* **54** 083021  
118 Takase Y., *et al.*, 1997 *Phys. Plasmas* **4** 1647  
119 Mossessian D. A., *et al.*, 2003 *Phys. Plasmas* **10** 1720  
120 F. Ryter, *et al.*, 2011 *Proc. 38th Euro. Conf. on Plasma Physics and Controlled  
Fusion, June 27-July 1, 2011, Strasbourg, France* P5.112  
121 Hubbard A. E., *et al.*, Proc. 24th Int. Conf. on Fusion Energy (San Diego, 2012)  
[EX/1-3] <http://www-naweb.iaea.org/napc/physics/FEC/FEC2012/index.htm>

122 Walk J. R., *et al.*, 2012 *Nucl. Fusion* **52** 063011  
 123 Groebner R. J., *et al.*, 2013 *Nucl. Fusion* **53** 093024  
 124 Martin Y. R., T. Takizuka, and ITPA CDBM H-mode Threshold Database  
 Working Group, 2008 *J. Phys.: Conf. Series* **123** 012033  
 125 Suttrop W., *et al.*, 2003 *Plasma Phys. Control. Fusion* **45** 1399  
 126 Suttrop W., *et al.*, 2004 *Plasma Phys. Control. Fusion* **46** A151  
 127 Suttrop W., *et al.*, 2005 *Nucl. Fusion* **45** 721  
 128 Sakamoto Y., *et al.*, 2004 *Plasma Phys. Control. Fusion* **46** A299  
 129 Oyama N., *et al.*, 2005 *Nucl. Fusion* **45** 871  
 130 Burrell K., *et al.*, 2009 *Phys. Rev. Lett.* **102**  
 131 Burrell K. H., *et al.*, 2005 *Phys. Plasmas* **12** 056121  
 132 Garofalo A., *et al.*, 2008 *Phys. Rev. Lett.* **101**  
 133 Solomon W. M., *et al.*, 2013 *Bull. Am. Phys. Soc.* **58** 108  
 134 Grierson B. A., *et al.*, “Response of Impurity Particle Confinement Time to  
 External Actuators in QH-mode Plasmas on DIII-D”, 2014 *Nucl. Fusion* **54**  
 submitted 12/2013.  
 135 Menard J. E., *et al.*, 2012 *Nucl. Fusion* **52** 083015  
 136 Yao L. G., *et al.*, 2001 *Nucl. Fusion* **41** 817  
 137 Xiao W. W., *et al.*, 2012 *Nucl. Fusion* **52** 114027  
 138 Horton L. D., *et al.*, 2004 *Plasma Phys. Control. Fusion* **46** B511  
 139 Rossel J. X., *et al.*, 2012 *Nucl. Fusion* **52** 032004  
 140 Liang Y., *et al.*, 2013 *Phys. Rev. Lett.* **110**  
 141 Li J., *et al.*, 2013 *Nature Phys.* **9** 817  
 142 Degeling A. W., *et al.*, 2003 *Plasma Phys. Control. Fusion* **45** 1637  
 143 Lang P. T., *et al.*, 2004 *Plasma Phys. Control. Fusion* **46** L31  
 144 de la Luna E., *et al.*, in Fusion Energy 2010 (Proc. 23rd Int. Conf. Daejeon, 2010)  
 (Vienna: IAEA) CD-ROM file [EXC/8-4] and [http://www-  
 naweb.iaea.org/napc/physics/FEC/FEC2010/index.htm](http://www-naweb.iaea.org/napc/physics/FEC/FEC2010/index.htm)  
 145 Gerhardt S. P., *et al.*, 2010 *Nucl. Fusion* **50** 064015  
 146 Dominguez A., 2012 *Ph. D. Thesis, Physics Dept., MIT*  
 147 Shoji T., *et al.*, 1992 *J. Nucl. Mater.* **196-198** 3098  
 148 Fielding S. J., 2001 *Europhys. Conf. Abstr.* **25** 1825  
 149 Canik J. M., *et al.*, in Fusion Energy 2008 (Proc. 22nd Int. Conf. Geneva, 2008)  
 (Vienna: IAEA) CD-ROM file [PD/P1] and [http://www-  
 naweb.iaea.org/napc/physics/FEC/FEC2008/html/index.htm](http://www-naweb.iaea.org/napc/physics/FEC/FEC2008/html/index.htm)  
 150 Strait E. J., 2009 *Nucl. Fusion* **49** 104008  
 151 Canik J. M., *et al.*, 2010 *Nucl. Fusion* **50** 034012  
 152 Canik J. M., *et al.*, 2010 *Phys. Rev. Lett.* **104** 045001  
 153 Canik J. M., *et al.*, 2010 *Nucl. Fusion* **50** 064016  
 154 Solomon W. M., *et al.*, 2012 *Nucl. Fusion* **52** 033007  
 155 Kugel H. W., *et al.*, 2008 *Phys. Plasmas* **15** 056118  
 156 Mansfield D. K., *et al.*, 2009 *J. Nucl. Mater.* **390-391** 764  
 157 Bell M. G., *et al.*, 2009 *Plasma Phys. Control. Fusion* **51** 124054  
 158 Kugel H. W., *et al.*, 2009 *J. Nucl. Mater.* **390-391** 1000  
 159 Kugel H. W., *et al.*, 2009 *Fusion Eng. Design* **84** 1125  
 160 Canik J. M., *et al.*, 2011 *Phys. Plasmas* **18** 056118

161 Maingi R., *et al.*, 2011 *Phys. Rev. Lett.* **107** 145004  
162 Kugel H. W., *et al.*, 2011 *J. Nucl. Mater.* **415** S400  
163 Boyle D. P., *et al.*, 2011 *Plasma Phys. Control. Fusion* **53** 105011  
164 Maingi R., *et al.*, Proc. 24th Int. Conf. on Fusion Energy (San Diego, 2012)  
[EX/11-2] <http://www-naweb.iaea.org/napc/physics/FEC/FEC2012/index.htm>  
165 Canik J. M., *et al.*, 2013 *Nucl. Fusion* **53** 113016  
166 Kaye S. M., *et al.*, 2013 *Nucl. Fusion* **53** 063005  
167 Boyle D., *et al.*, 2013 *J. Nucl. Mater.* **438** S979  
168 Duan X. R., *et al.*, 2013 *Nucl. Fusion* **53** 104009  
169 Xiao W. W., *et al.*, 2014 *Nucl. Fusion* **54** 023003  
170 Rhee T., *et al.*, 2012 *Phys. Plasmas* **19** 022505  
171 Mailloux J., *et al.*, 2002 *Phys. Plasmas* **9** 2156  
172 Hughes J. W., *et al.*, 2010 *Nucl. Fusion* **50** 064001  
173 Marmor E., *et al.*, 2009 *Nucl. Fusion* **49** 104014  
174 Ferron J. R., *et al.*, 2000 *Phys. Plasmas* **7** 1976  
175 Canik J. M., *et al.*, 2012 *Nucl. Fusion* **52** 054004  
176 Guo H. Y., *et al.*, 2014 *Nucl. Fusion* **54** 013002  
177 Wang H. Q., *et al.*, 2012 *Nucl. Fusion* **52** 123011  
178 Mattas R., *et al.*, 2000 *Fusion Eng. Design* **49** 127  
179 Brooks J. N., 2002 *Fus. Eng. Des.* **60** 515  
180 Ono M., *et al.*, 2013 *Nucl. Fusion* **53** 113030  
181 Maingi R., *et al.*, 2005 *Nucl. Fusion* **45** 1066  
182 Stober J., M. Maraschek, and Conway G. D., 2001 *Nucl. Fusion* **41** 1123  
183 Kamada Y., *et al.*, 2000 *Plasma Phys. Control. Fusion* **42** A247  
184 Kirk A., *et al.*, 2011 *Plasma Phys. Control. Fusion* **53** 095008  
185 Maingi R., *et al.*, 2011 *Nucl. Fusion* **51** 063036  
186 Baylor L. R., *et al.*, 2013 *Bull. Am. Phys. Soc.* **58** 239

---

# Princeton Plasma Physics Laboratory Office of Reports and Publications

Managed by  
Princeton University

under contract with the  
U.S. Department of Energy  
(DE-AC02-09CH11466)

---

P.O. Box 451, Princeton, NJ 08543  
Phone: 609-243-2245  
Fax: 609-243-2751

E-mail: [publications@pppl.gov](mailto:publications@pppl.gov)

Website: <http://www.pppl.gov>